Eindhoven University of Technology

MASTER

The influence of non-local spin transport on all-optical switching in synthetic ferrimagnetic bilayers

Peters, Maarten R.A.

Award date:
2021

EINDHOVEN UNIVERSITY OF TECHNOLOGY

Department of Applied Physics
Physics of Nanostructures

The influence of non-local
spin transport on all-optical switching
in synthetic ferrimagnetic bilayers

Master Thesis

M.R.A. Peters

Supervisors:
prof.dr. B. Koopmans
dr.ir. R. Lavrijsen
ir. Y.L.W. van Hees

Eindhoven, February 2021

Abstract

Since the pioneering experiments in 1996, the response of magnetic materials to femtosecond laser excitation has been widely researched. Among others, ultrafast magnetization dynamics, laser induced non-local spin transport and all-optical switching of the magnetization have been reported. Recent research has shown that by combining non-local spin transport with all-optical switching, magnetic domains can deterministically be written. Deterministic writing is achieved by exciting a $[Co/Ni]_4/Co/Cu/Pt/Co/Gd$ multilayer with a linearly polarized laser pulse with a well chosen energy. Depending on the relative orientation of the magnetization of the two layers (parallel or antiparallel, respectively) all-optical switching of the Co/Gd bilayer is hindered or assisted. The deterministic writing is attributed to the transport of angular momentum between the [Co/Ni] multilayer and the Co/Gd bilayer via mobile, spin-polarized electrons. The microscopic origin of this laser induced non-local spin transport as well as all-optical switching is still under debate.

The influence of non-local spin transport on all-optical switching in synthetic ferrimagnetic bilayers is investigated. The research is performed by means of experiment as well as numerical modelling. In the employed model, the microscopic origin of the laser induced magnetization dynamics as well as non-local spin transport is assumed to be the $(s - d)$ exchange interaction between the localized (d) spins and mobile (s) spins. The switching dynamics of synthetic ferrimagnetic Co/Gd bilayers as well as $[Co/Ni]_4/Co/Cu/Pt/Co/Gd$ multilayers are modelled. Laser induced switching on a ps timescale as a result of the $s - d$ exchange interaction is reproduced. However, all-optical switching is only observed for laser energies where the phonon temperature is raised above the Curie temperature. As this leads to unrealistic conditions in experiment, it is concluded that the $s - d$ exchange interaction alone is unable to explain the experimentally observed all-optical switching in synthetic ferrimagnetic bilayers.

From static switching experiments on synthetic ferrimagnetic bilayers (Co/Gd) as well as multilayer samples for spin current assisted all-optical switching ($[Co/Ni]4/Co/Cu/Pt/Co/Gd$) the (planar) threshold laser fluence is determined as a function of the thickness of the Co layer that is part the Co/Gd bilayer. Although the measured Co thickness range is small, for both samples the threshold fluence is found to increase with Co thickness. For the Co/Gd bilayer, all-optical switching appears to become increasingly difficult with Co layer thickness. For the $[Co/Ni]_4/Co/Cu/Pt/Co/Gd$ multilayer, the laser fluence range in which magnetic domains are written deterministically is found to increase with the thickness of the Co layer that is part of the Co/Gd bilayer. These experimental observations are reproduced by the $s - d$ model.

Time-resolved magneto-optic Kerr effect experiments are employed in order to measure the ultrafast magnetization dynamics in $[Co/Ni]_4/Co/Cu/Pt/Co/Gd$ multilayers after femtosecond laser excitation. The experimental data indicates that the ultrafast dynamics in the $[Co/Ni]_4$ multilayer are barely influenced by non-local spin transport. The dynamics in the Co/Gd bilayer however are strongly influenced by the spin current originating from the reference layer. The Co/Gd switching dynamics are measured for switching from an antiparallel to parallel magnetization configuration and vice versa. As is expected from the effect of non-local spin transport, the Co/Gd magnetization is found to reverse at a faster rate when the sample is switched from an antiparallel to a parallel state than when it is switched in the opposite direction. Again, this experimental observation is reproduced by the $s - d$ model.

The work presented in this thesis indicates that the experimentally observed phenomena that are attributed to laser induced non-local spin transport can be explained by itinerant spin-polarized electrons that are accumulated through the $s - d$ exchange interaction. A good understanding of the microscopic origin of the laser induced non-local spin transport is required in order to apply and optimize deterministic all-optical writing in future memory devices.

List of Abbreviations

3TM   Three-temperature model
AF   Antiferromagnetically
AP   Antiparallel
AOS   All-optical switching
DW   Domain wall
FM   Ferromagnetic metal
GMR   Giant magneto resistance
HDD   Hard disk drives
HM   Heavy metal
HWP   Half-wave plate
LCP   Left circularly polarized
M3TM   Microscopic three-temperature model
MCD   Magnetic circular dichroism
MOKE   Magneto-optic Kerr effect
MRAM   Magnetic random acces memory
MTJ   Magnetic tunnel junction
NM   Normal metal
OOP   Out-of-plane
PEM   Photo-elastic modulator
PMA   Perpendicular magnetic anisotropy
P   Parallel
QWP   Quarter-wave plate
RAM   Random access memory
RCP   Right circularly polarized
RE   Rare-earth metal
RTM   Racetrack memory
SDSE   Spin-dependent Seebeck effect
SSD   Solid-state drive
STT   Spin-transfer torque
TM   Transition metal
TMM   Transfer matrix method
TMR   Tunnel magnetoresistance
TR   Time-resolved

Contents

1   Introduction

Since the invention of computers, digital data has become an increasingly important part of our lives. Research in the field of spintronics is focussed on the development of a new generation of memory devices by combining an electron's charge and spin properties. Historically, magnetic hard disk drives are used to store digital data on a long-term basis. A HDD consists of a rigid disk covered with magnetic domains. The data is stored in the direction of the magnetic domain (e.g. '1' for magnetization up, '0' for down). By spinning the disk past a read or write head, digital data is retrieved (read) or stored (written), respectively. A HDD provides a robust way to store data in a non-volatile way, i.e. the information remains without any applied voltage. However, the read and write speed of a HDD is relatively slow [1] and limited by the need for mechanical motion. Furthermore, in terms of storage capacity, the improvement of HDDs has stagnated in the past decade [2, 3].

Recently, transistor based NAND solid-state drives (SSDs) have surpassed HDDs in terms of (planar) storage capacity [4]. In a SSD, data is stored (in a non-volatile way) as electric charge in the transistors floating gate. The storage capacity is typically increased and costs are typically reduced by downsizing the transistors. However, with a transistor size as small as 5-10 nm, processing has become complicated and costly [3, 4]. Besides, the transistors run into some physical issues, when they are scaled down to these small sizes [4, 5]. With the transition to 3D-NAND architectures, some of these problems are overcome. With the 3D architecture, simultaneously, progress is made in terms of (volumetric) storage capacity. However, the so-called 'power wall' (decreasing energy efficiency due to increasing heat dissipation) ultimately limits the optimization of SSDs by downscaling the transistor size.

As the amount of generated data worldwide is increasing, the development of a new, fast and energy efficient alternative for data storage is needed. Spintronics can be employed for the development of a new generation of magnetic memory devices. In this chapter, two of these newly proposed devices are introduced, namely the magnetic random access memory (MRAM) [6] and the racetrack memory (RTM) [1, 7]. Both technologies have the potential to serve as universal memory, i.e. a memory that not only serves for long-term data storage, but simultaneously replaces the volatile static random access memory (SRAM) or dynamic random access memory (DRAM) devices as primary memory. This research focusses on the possibility to combine non-local spin transport with all-optical switching (AOS) as write mechanism in these devices. AOS based memory devices show high potential for use with future photonic integrated circuits (PICs) [8, 9]. In terms of writing speed and energy efficiency an AOS based device has the potential to outperform devices with an electrical writing mechanisms, since no signal conversion from photonic to electric or vice versa is required.

1.1   Magnetic random access memory

Similar to HDDs, in MRAM digital data is stored in the magnetization direction of a magnetic domain. The operation principle of the device however, is fundamentally different. In contrast to HDDs, MRAM does not contain any moving parts, but an architecture similar to SDDs (figure 1.1a). HDDs typically use applied fields, whereas for MRAM, data is written and read electrically.

MRAM devices generally store data in a magnetic tunnel junction (MTJ). The MTJ bit consists of two magnetic layers, one free layer and one fixed layer. The layers are separated by an insulating oxide barrier layer. The tunnel magnetoresistance (TMR) effect [10] is used to read the data stored in a bit. Due to the TMR effect, the resistance of the multilayer structure depends on the relative orientation of the magnetic layers. When the free layer's magnetization is oriented parallel (P) to the fixed layer (figure 1.1b), the multilayer has a relatively low resistance. For an antiparallel (AP) configuration a high resistance is observed (figure 1.1c). This difference in resistance can be used to differentiate between a logic '0' and '1'.

The MTJ device can be written with spin-transfer torques (STTs) [11, 12] or spin-orbit torques (SOTs)

(a) MRAM   (b) low resistivity   (c) high resistivity
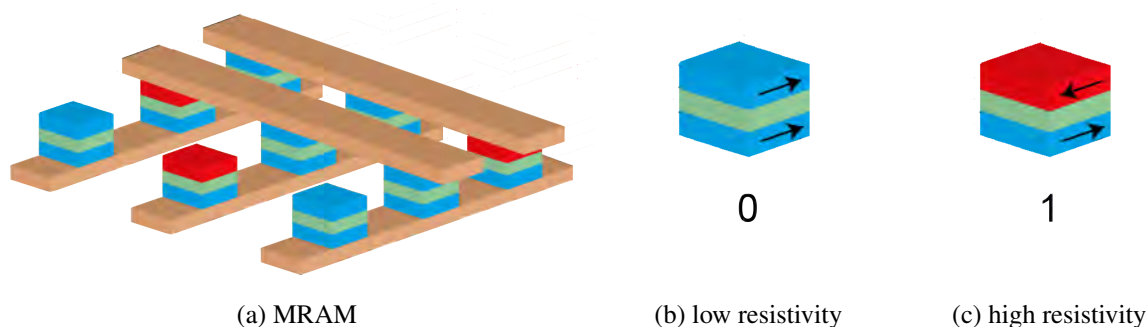
Figure 1.1: (a) Schematic representation of an MRAM device. (b) The parallel magnetization configuration results in a low resistive state, which is used to represent a logic '0' in MRAM. (c) The antiparallel configuration results in a high resistivity, representing a logic '1' in MRAM.

[13, 14]. In this manner, a write time in the order of a few nanoseconds down to 400 ps [15] can be achieved [1, 6]. With its fast read and write speeds, the non-volatile MRAM has the potential to serve as a universal memory. The STT-MRAM, however, has the disadvantage that read and write current use the same path (figure 1.2a) [13]. For SOT-MRAM devices (figure 1.2b) the write current generally flows underneath the MTJ. This three-terminal architecture however could results in an increased bit size and thus in a reduced storage capacity [13].
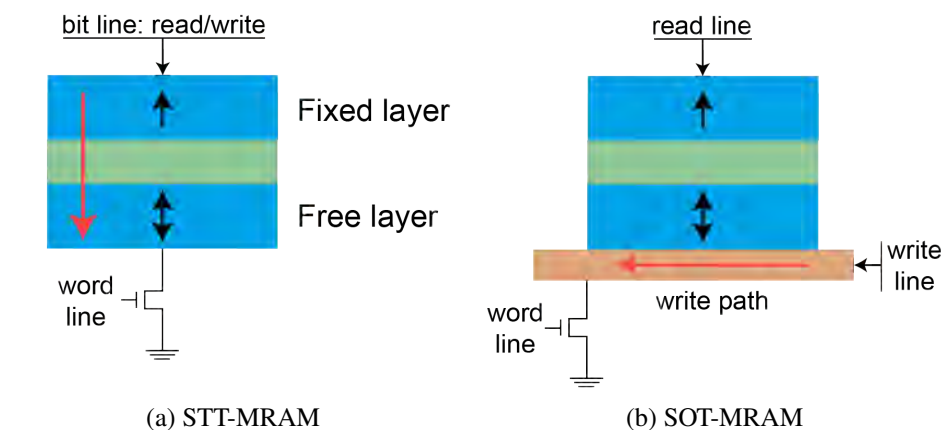
(a) STT-MRAM   (b) SOT-MRAM

Figure 1.2: Schematic representation of an (a) STT-MRAM and (b) SOT-MRAM MTJ. The red arrow represents the path of the write current.

1.2 Racetrack memory

Similar to MRAM, the magnetic racetrack memory (RTM) has the potential to serve as universal memory. In the initially proposed RTM [7], data is stored in the domain walls (DWs) between magnetic domains. In order to operate the RTM, STTs as well as SOTs can be used to move the DWs through the device by means of current pulses (figure 1.3) [1, 2]. By moving them past the read and write heads, the data is read or written. In this manner, a single read or write head can be used to read or write multiple bits (similar to HDD). Consequently, in the RTM a higher (planar) storage capacity can be achieved than for MRAM. By moving to a 3D structure (figure 1.3b), the (volumetric) storage capacity can potentially be even further improved. MTJs can again be used to read the data through TMR and write the data with STTs or SOTs [1, 2]. Both STT and SOT provide a read and write time in the order of nanoseconds. Compared to MRAM, for the RTM, an extra shift latency is introduced, depending on the DW velocity [1].

(a) horizontal RTM   (b) vertical RTM
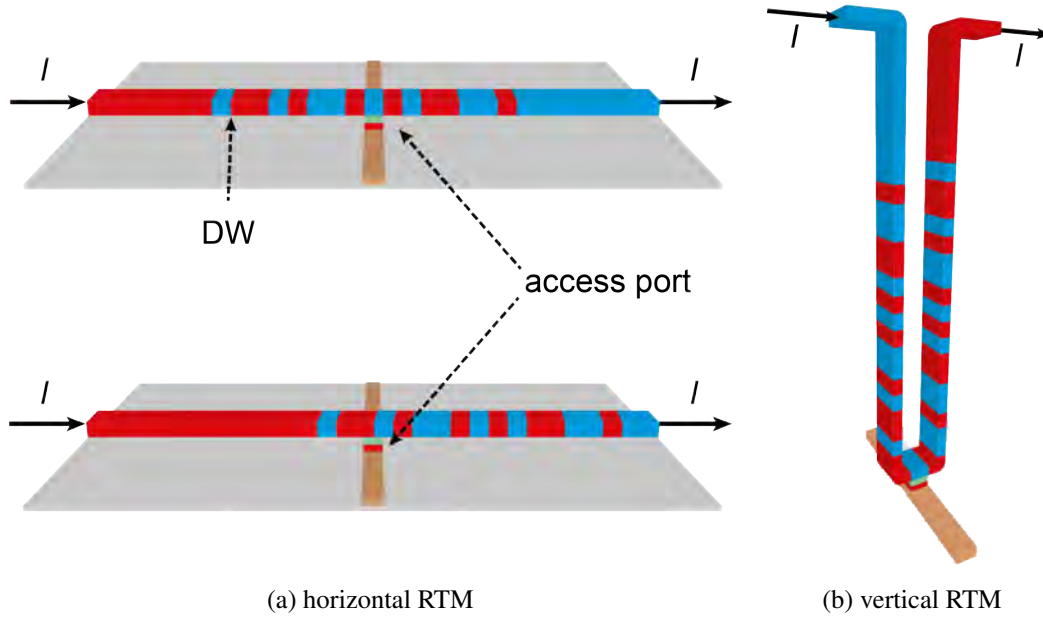
Figure 1.3: (a) Horizontal RTM. By applying current pulses (top) the data is moved through the device (bottom). (b) Vertical RTM. Adapted from [1].

1.3   All-optical switching

One of the main requirements for any universal memory (MRAM or RTM), is the possibility to write data on a short timescale. While (as previously mentioned) the magnetization can electrically be reversed on a ns timescale, it is possible to switch the magnetization on an even shorter timescale with a laser pulse. A fs laser pulse is one of the fastest available stimuli for the excitation of a material. Since Beaurepaire *et al.* [16] showed the ultrafast (sub ps) quenching of the magnetization of nickel (Ni) after excitation with a laser pulse, the response of magnetic materials to laser light has been widely researched.

1.3.1   All-optical toggle switching

It was discovered that the magnetization of certain ferrimagnetic alloys (such as GdFeCo) can be switched by exciting the alloy with a single circularly polarized laser pulse [17]. The switching was initially found to be helicity-dependent [17, 18]. However, this helicity-dependence was later attributed to magnetic circular dichroism (MCD) [19], i.e. the difference in absorption for left and right circularly polarized light in a magnetic field. Further research has shown all-optical switching (AOS) of ferrimagnetic alloys [20, 21] and synthetic ferrimagnets [19] with a single linearly polarized laser pulse. The magnetization reversal in this process has been demonstrated to be thermally driven [21].

Every linearly polarized laser pulse switches the magnetization, regardless of the initial state. In other words, by applying just one pulse, a magnetic domain is switched (figure 1.4). A second pulse toggles the magnetization back to its original direction, a third pulse again switches the domain, etc. Through AOS, the magnetization can be reversed on a timescale in the order of 10 ps [9], which is significantly faster than the observed 400 ps SOT switching.

Because of its fast switching times and high energy efficiency, it has been suggested to integrate AOS with spintronic memory devices (figure 1.5) [8, 9, 22]. Synthetic ferrimagnetic cobalt/gadolinium (Co/Gd) bilayers on a heavy metal (HM) layer, such as platinum (Pt), are a promising candidate for the RTM [19]. The Co/Gd bilayer allows for AOS. The Pt enables the generation of SOTs as well as high DW velocities as a result of the Dzyaloshinskii-Moriya interaction (DMI) [23].
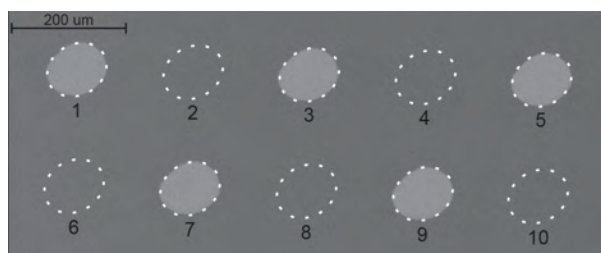
Figure 1.4: Kerr microscope image of a Co/Gd bilayer after exposure to an increasing number of laser pulses. The contrast shows the (relative) orientation of the magnetization. Every odd pulse switches the magnetization of the exposed domain. Every even pulse switches the magnetization back, restoring the domain in its initial state. From [19].

(a) AOS-MRAM   (b) AOS-RTM
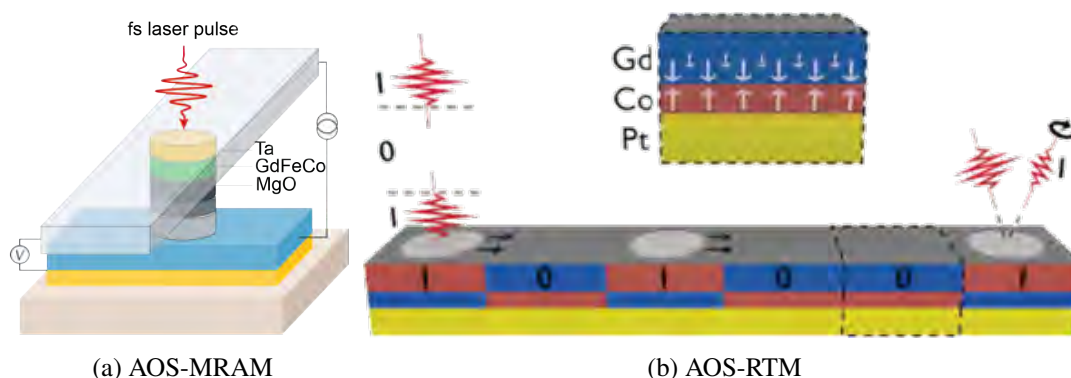
Figure 1.5: (a) Schematic representation of all-optically switchable MTJ suitable for integration in MRAM. Adapted from [22]. (b) Schematic representation of a Pt/Co/Gd RTM. Bits are written by AOS (left) and then moved along the racetrack with current pulses. The data can potentially be read optically through the magneto-optic Kerr effect (right). From [19].

The integration of AOS in memory devices is particularly interesting for integrated photonics [24]. By integrating AOS in MRAM (figure 1.5a) or RTM (figure 1.5b) with photonics, data can directly, all-optically be written, skipping the optical to electrical signal conversion. The data can be optically read by (for example) the magneto-optic Kerr effect (MOKE, figure 1.5b).

1.3.2   Spin current assisted AOS

In conventional AOS, each laser pulse reverses the magnetization, regardless of the initial state (figure 1.4). Consequently, in order to write data through AOS, the initial state of the bit first needs to be read. This limits the writing speed of a device. Research [25, 26] has shown that laser excitation of a ferromagnetic metal (FM) in a metallic multilayer not only leads to ultrafast dynamics for the local magnetization, but also transports spins from the FM layer into the multilayer. It has recently been suggested to combine laser induced non-local spin transport with AOS [27, 28, 29] in order to write data deterministically. In this deterministic writing scheme, the desired final state is written regardless of the initial state of the bit.

For this so-called 'spin current assisted AOS' [28], a multilayer sample consisting of a free layer, conductive spacer layer and a reference layer is used (figure 1.6). The free layer consists of a transition metal/rare-earth metal (TM/RE) synthetic ferrimagnetic bilayer, such as Co/Gd. A normal metal (NM), such as copper (Cu), is used as spacer layer. The reference layer is a ferromagnetic metal layer, e.g. a Co/Ni multilayer. Both the free and reference layer exhibit perpendicular magnetic anisotropy (PMA). The free layer can be switched by laser excitation. Furthermore, the laser excites a spin current that flows from the reference layer through the NM spacer to the free layer. Depending on the relative orien-
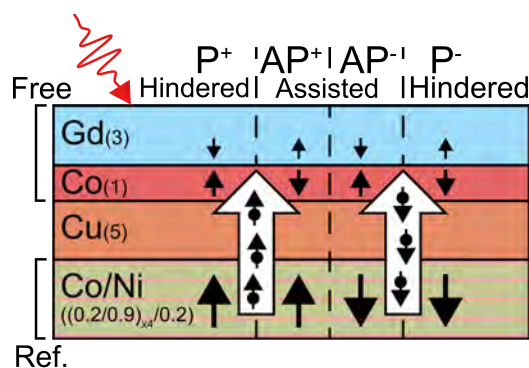
Figure 1.6: Schematic representation of the magnetic multilayer sample for spin current assisted AOS. The magnetization direction of the different magnetic layers is indicated with black arrows. All four possible configurations of the sample are shown, i.e. P+, AP+, P- and AP-, where the plus and minus sign indicate whether the reference layer's magnetization is directed in the + or -z-direction. The spins in the center of the white arrows indicate the (main) polarization of the spin current from the Co/Ni to the Co/Gd. From [28].

tation of the magnetization of the TM layer (that is part of the free layer) and the FM reference layer, the spin current either hinders or assists AOS. For a parallel (P) alignment, switching is hindered, whereas in an antiparallel (AP) configuration the non-local spin transport assists AOS. As a result, a difference in energy required to switch the multilayer stack from parallel to antiparallel configuration, P→AP, and from antiparallel to parallel, AP→P, is observed. This energy difference can be employed to write data deterministically [28].

1.4   Thesis outline

In order to apply and optimize spin current assisted AOS in spintronic devices, a good understanding of the nature and behavior of the laser induced phenomena is required. However, the microscopic origin of ultrafast magnetization dynamics and laser induced non-local spin transport is still under debate. In this thesis the non-local spin transport and its influence on AOS in synthetic ferrimagnetic TM/RE bilayers as well as FM/NM/TM/RE magnetic multilayers is investigated. The goal is to determine whether spin current assisted AOS can be explained from the $s - d$ exchange interaction, what the influence of (the thickness of) the Co and Gd layers on this spin current assisted AOS is and how the spin transport between the reference layer and free layer change the ultrafast laser-induced dynamics (where the TM/RE free layer's switching dynamics are of particular interest).

Before the research findings are presented, in chapter 2 the theoretical background and some of the existing models on spin transport and AOS are explained. The discussed models are the (microscopic) three temperature model or (M)3TM and the $s - d$ model. The experimental methodology is explained in chapter 3. Both static measurements and time-resolved MOKE experiments are employed. The research findings (chapter 4) indicate that experimentally observations that are attributed to (non-local) spin transport can potentially be explained from the $s - d$ model. Furthermore, the findings indicate that the FM reference layer's ultrafast dynamics are barely influenced by spin currents generated in the TM/RE free layer. However, a clear influence of the reference layer on the free layer's switching dynamics is observed.

2   Theoretical background

In this chapter, the theoretical background regarding all-optical switching and optically induced spin transport is introduced. First, femtomagnetism and laser induced phenomena, such as laser induced spin currents and all-optical switching, are described phenomenologically. Then, two of the established theories regarding the underlying microscopic mechanism are discussed, i.e. the microscopic three-temperature model (M3TM) [30] and the $s-d$ model [31, 32]. The M3TM assumes Elliot-Yafet electron-phonon scattering to be the driving microscopic mechanism for ultrafast demagnetization. In the $s-d$ model, not Elliot-Yafet electron-phonon scattering, but the coupling between the localized spins and mobile spins ($3d$ and $4s$ in transition metals, respectively), i.e. the $s-d$ exchange interaction, is assumed to be the driving mechanism.

2.1   Femtomagnetism

In 1996 Beaurepaire *et al.* [16] reported the ultrafast demagnetization of ferromagnetic metals after laser excitation. This started extensive research into the response of magnetic materials to fs laser pulses.

2.1.1   Ultrafast magnetization dynamics

In the original experiment (figure 2.1a) a nickel thin film was demagnetized on a sub-picosecond timescale. The ultrafast demagnetization dynamics were explained by a phenomenological model, the so-called three-temperature model (3TM) [16]. The 3TM describes the laser induced dynamics of the magnet without going into the microscopic origin of these dynamics.

<div align="center">(a)   (b)</div>
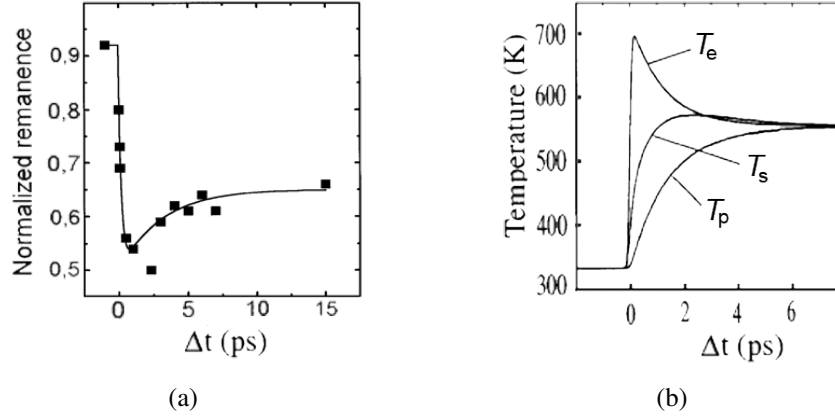
Figure 2.1: (a) Time-resolved measurement of the ultrafast quenching of the Ni magnetization after excitation with a 60 fs laser pulse at $\Delta t = 0$. (b) The calculated evolution of $T_{e,p,s}$ from the 3TM. (a) and (b) from [16].

In the 3TM, the magnetic material is divided in three thermalized subsystems, i.e. an electron, phonon and spin system. Three temperatures, T_e, T_p and T_s, respectively, are assigned to the electron, phonon and spin subsystems. Energy is exchanged between these three subsystems. This energy exchange is described in terms of three coupled differential equations for T_e, T_p and T_s,

$$
\begin{aligned}
C_{\mathrm{e}}\frac{\mathrm{d}T_{\mathrm{e}}}{\mathrm{d}t} &= -G_{\mathrm{ep}}(T_{\mathrm{e}}-T_{\mathrm{p}})-G_{\mathrm{es}}(T_{\mathrm{e}}-T_{\mathrm{s}})+P(t),\\
C_{\mathrm{p}}\frac{\mathrm{d}T_{\mathrm{p}}}{\mathrm{d}t} &= G_{\mathrm{ep}}(T_{\mathrm{e}}-T_{\mathrm{p}})-G_{\mathrm{ps}}(T_{\mathrm{p}}-T_{\mathrm{s}}),\\
C_{\mathrm{s}}\frac{\mathrm{d}T_{\mathrm{s}}}{\mathrm{d}t} &= G_{\mathrm{es}}(T_{\mathrm{e}}-T_{\mathrm{s}})+G_{\mathrm{ps}}(T_{\mathrm{p}}-T_{\mathrm{s}}),
\end{aligned}
\tag{2.1}
$$

with $C_{\mathrm{e,p,s}}$ the subsystem contributions to the specific heat, $G_{\mathrm{ep,es,ps}}$ the coupling constants between the subsystems and $P(t)$ the laser pulse, which acts as a heat source. The electron system is assumed to be solely thermal and does not carry any angular momentum. The magnetization m depends on the spin temperature T_{s} and can be determined through a Weiss mean-field approach [10, 33].

The laser energy is initially absorbed by the thermal electrons. The energy is then distributed over the other subsystems (figure 2.1b). Two different timescales can be defined [33, 34], the electron-phonon equilibration timescale τ_{e}, which is directly dependent on G_{ep}, and the time-scale of the magnetization loss τ_{m}, which contains both electron-spin and phonon-spin contributions.

While the ultrafast demagnetization of a FM can be phenomenologically described with the 3TM, the 3TM does not provide any insight in the microscopic origin of the fs laser induced dynamics. The microscopic origin of ultrafast magnetization dynamics is still under debate. Among others, local spin dynamics due to laser heating [30, 32, 33, 35, 36] and spin-dependent transport of hot electrons [37, 38] have been proposed as the microscopic processes that drive these laser induced phenomena.

2.1.2 Laser induced spin transport

(a)   (b) conductive spacer   (c) insulating spacer
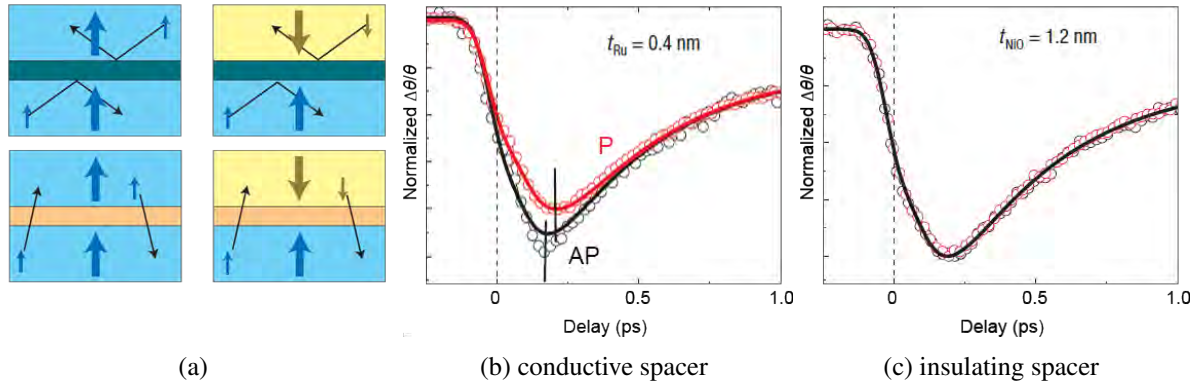
Figure 2.2: (a) Schematic representation of a magnetic multilayer sample consisting of two identical FM layers. There are two possible configurations, P (left) and AP (right). Depending on the spacer layer, i.e. insulating (top) or conductive (bottom), spin transport between the two layers is prevented or allowed, respectively. (b) & (c) Time-resolved magneto-optic Kerr measurement of the demagnetization of one of the two FM layers for a conductive and an insulating spacer, respectively. (a), (b) and (c) adapted from [25].

In addition to ultrafast demagnetization, the excitation of a FM with a fs laser pulse can be used to transport spin-polarized electrons out of the FM layer. This so-called spin current transports angular momentum, which can be used to excite a second magnetic layer [25, 26]. The demagnetization rate of a FM thin film is influenced by a second FM layer when the two layers are separated by a thin conductive spacer (figure 2.2) [25]. Demagnetization is either hindered or assisted, depending on the relative orientation of the two FM layers (parallel or antiparallel, respectively, figure 2.2b). When the magnetization of the two layers is aligned AP, the polarization of the spin current generated in one layer is opposite to the orientation of the majority spins in the other layer. Due to spin-flip scattering between

the local bands in the FM layer and the electrons transported by the spin current, angular momentum is transferred between the majority spins and the itinerant electrons. The spin current thus increases the demagnetization rate of the FM layer, resulting in more and faster demagnetization (figure 2.2b). The effect disappears when instead of a conductive spacer, an insulating layer is used (figure 2.2c).

The microscopic origin of the laser induced spin currents is, similar to the microscopic origin of ultrafast magnetization dynamics, still under debate. The theory of superdiffusive spin transport [37, 38] assumes spin-dependent transport of excited electrons as the driving mechanism for ultrafast demagnetization. Other existing models, such as the $s - d$ model, assume a spin current generation rate proportional to the demagnetization rate, i.e. proportional to the time derivative of the magnetization $\frac{dm}{dt}$ [26, 31, 32]. Furthermore, as a result of a thermal gradient induced by the laser pulse, the spin-dependent Seebeck effect (SDSE) [26, 39] is expected to contribute to the spin current.

2.1.3   All-optical switching

Single pulse helicity independent all-optical switching was first shown in ferrimagnetic alloys and later also shown for synthetic ferrimagnetic bilayers. Where a ferromagnet consists of a single magnetization lattice, a ferrimagnet has two anti-ferromagnetically coupled sublattices (figure 2.3a) and is described by two spin systems. By excitation with a linearly polarized fs laser pulse, the orientation of both sublattices can be switched.

Radu *et al.* [20] showed that the difference in laser induced demagnetization between the two sublattices in the ferrimagnet plays an important role in AOS of a ferrimagnetic alloy (GdFeCo). As a result of the faster demagnetization rate for the TM sublattice, the TM magnetization is almost completely quenched, while the RE sublattice is still magnetised. Due to angular momentum transfer from the RE to the TM sublattice, the TM sublattice magnetization is switched, i.e. crosses zero (figure 2.3b). Meanwhile, the RE sublattice is still oriented in its initial direction. A transient ferromagnetic-like state is observed. Once the TM magnetization has recovered sufficiently, due to the anti-ferromagnetic exchange coupling between the sublattices, the RE magnetization is switched as well.

(a) ferrimagnetic sublattices   (b) AOS
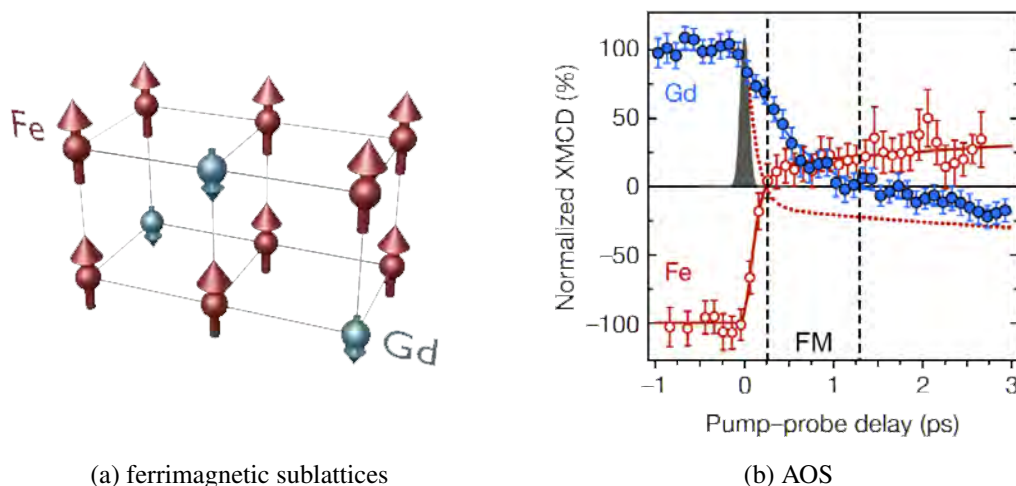
Figure 2.3: (a) Schematic representation of the sublattices in a ferrimagnetic alloy. The RE (Gd) and TM (Fe) magnetizations are aligned antiparallel. (b) Time-resolved x-ray magnetic circular dichroism (XMCD) measurement of the Fe and Gd magnetization for AOS in a GdFeCo ferrimagnetic alloy. A transient ferromagnetic-like (FM) state is observed. (a) and (b) adapted from [20].

Direct angular momentum transfer from between the local $3d$ and $4f$ bands of the TM and RE, respectively, could explain the observed AOS dynamics [40, 41, 42]. Other research, however, has focussed on the role of the conduction (sp) band in AOS [43, 44]. Choi *et al.* [44] performed measurements on a fer-

rimagnetic alloy/NM bilayer. They measured the spin accumulation in the normal metal (figure 2.4). The long-lived (up-to at least 10 ps), negative contribution to the signal is (mainly) attributed to a combination of SDSE and the demagnetization of the RE sublattice. Since AOS is observed in $Gd_{25}Fe_{65.6}Co_{9.4}$ and not in $Tb_{20}Fe_{62}Co_{18}$, the increase in RE contribution for the $Gd_{25}Fe_{65.6}Co_{9.4}$ (blue triangles) compared to the $Tb_{20}Fe_{62}Co_{18}$ (black squares) measurement suggests a significant role of the conduction band in AOS [44]. In other experiments [41, 42], however, no indication of a significant conduction band contribution to the switching process has been found.
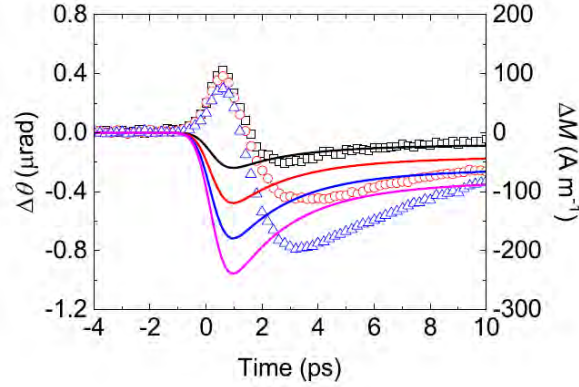
Figure 2.4: Time-resolved MOKE measurement of the spin accumulation on the NM (Cu) surface for $Tb_{20}Fe_{62}Co_{18}$/Cu (black squares), $Gd_{22}Fe_{68.5}Co_{9.5}$/Cu (red circles) and $Gd_{25}Fe_{65.6}Co_{9.4}$/Cu (blue triangles) bilayers. The solid lines represent spin diffusion calculations for spin generation from the SDSE. The (qualitative) difference between the experimental and simulated data indicates a large contribution of the RE demagnetization to the spin accumulation in the all-optically switchable $Gd_{22}Fe_{68.5}Co_{9.5}$. From [44].

2.1.4 Spin current assisted all-optical switching

It has recently been suggested to combine AOS with laser induced non-local spin transport [27, 28, 29]. For this so-called 'spin current assisted AOS' a multilayer sample consisting of a synthetic ferrimagnetic (Co/Gd) free layer, NM (Cu) spacer layer and a FM ([Co/Ni]) reference layer (figure 1.6) is used [28].
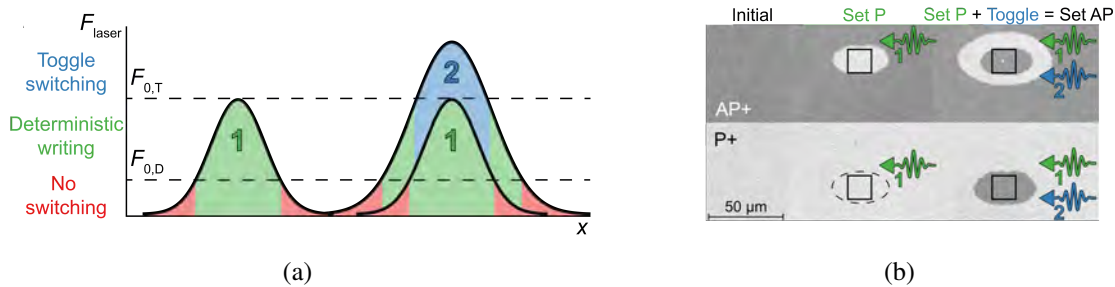
Figure 2.5: (a) Sketch of the spacial distribution of the fluence F_{laser} of Gaussian shaped laser pulses in the deterministic writing scheme. (b) Kerr microscope image of the initial and final states for the deterministic writing scheme. Regardless of the initial state, a single pulse with a laser fluence in the deterministic writing regime (left) ensures the system ends up in P configuration (left black squares). With a second pulse (right) in the toggle regime, the P state written by the first pulse is toggled to an AP state (right black squares). (a) and (b) are adapted from [28]

Similar to the FM/NM/FM multilayer experiment (figure 2.2), spin-polarized electrons transport angular momentum between the reference and free layer. Depending on the relative orientation of the magnetization of the TM layer (that is part of the free layer) and the magnetization of the FM reference layer, the

spin current either hinders or assists AOS. For a parallel (P) alignment, switching is hindered, whereas in an antiparallel configuration the non-local spin transport assists AOS. Three different laser fluence regimes can be distinguished (figure 2.5a). In the first, low fluence regime the laser pulse does not induce any switch in the multilayer. In this regime only demagnetization occurs. The second regime is the deterministic writing regime, where the laser fluence is sufficiently large for AP→P switching to occur. In this regime, however, the laser has a fluence that is below the P→AP switching threshold. The final regime is the toggle regime, where P→AP and AP→P switching occur.

The existence of the second regime can be employed to write data deterministically [28]. For a laser pulse in this regime, regardless of the multilayer's initial state, the final state of the system is known. Applying a single pulse in this regime writes a P state or logical zero. With two pulses, the first pulse in the deterministic and second pulse in the toggle regime, an AP state or logical one is written (figure 2.5).

In the following sections, two different theories regarding the microscopic origin of the ultrafast laser induced phenomena are introduced. First the M3TM is treated. The M3TM assumes Elliot-Yafet electron-phonon scattering to be the driving microscopic mechanism for ultrafast demagnetization. All-optical switching is attributed to direct angular momentum transfer from between the local bands. In the second model, the $s - d$ model, the coupling between the localized (d) spins and mobile (s) spins is assumed to be the driving mechanism for ultrafast laser induced dynamics. The creation of itinerant s electrons through this $s - d$ interaction could potentially drive AOS.

2.2   Microscopic three-temperature model

In this section, a microscopic extension of the 3TM based on local spin dynamics, the so-called microscopic three-temperature model (M3TM), is discussed. In the M3TM, laser induced demagnetization is attributed to Elliot-Yafet spin-flip scattering. The spin system relaxes due to (local) angular momentum transfer from the spin to the phonon subsystem (figure 2.6b) by an electron-phonon-spin scattering event. Similar to the 3TM, the electron system is assumed to be solely thermal and does not carry any angular momentum. Since the spin subsystem is described by a stationary spin lattice, the generation of laser induced spin currents can not be described within the M3TM.

2.2.1   M3TM for a single macro spin

The electron subsystem is modelled as a free electron gas with constant density of states (DOS). The phonon subsystem is described by a Debye model. It is generally assumed that the electron and phonon subsystem both are in internal equilibrium, i.e. there is a well defined electron and phonon temperature, T_e and T_p, respectively. By also assuming that the electron-phonon scattering rate for scattering events without a spin-flip is not influenced by the presence of the spin system, these subsystems within the M3TM are described by the standard two temperature model [45],

$$
\begin{aligned}
\gamma_e T_e \frac{dT_e}{dt} &= g_{ep}(T_p - T_e) + P(t), \\
C_p \frac{dT_p}{dt} &= g_{ep}(T_e - T_p) + C_p \frac{T_{amb} - T_p}{\tau_D},
\end{aligned}
\tag{2.2}
$$

where g_{ep} is the electron-phonon coupling factor and the electron specific heat is given by $C_e = \gamma_e T_e$, with proportionality factor γ_e. In comparison to equations 2.1 an extra term is added. This term describes the energy dissipation from the sample to the substrate. The ambient (or substrate) temperature is denoted with T_{amb} and τ_D is the timescale at which energy is dissipated.

(a) energy   (b) angular momentum
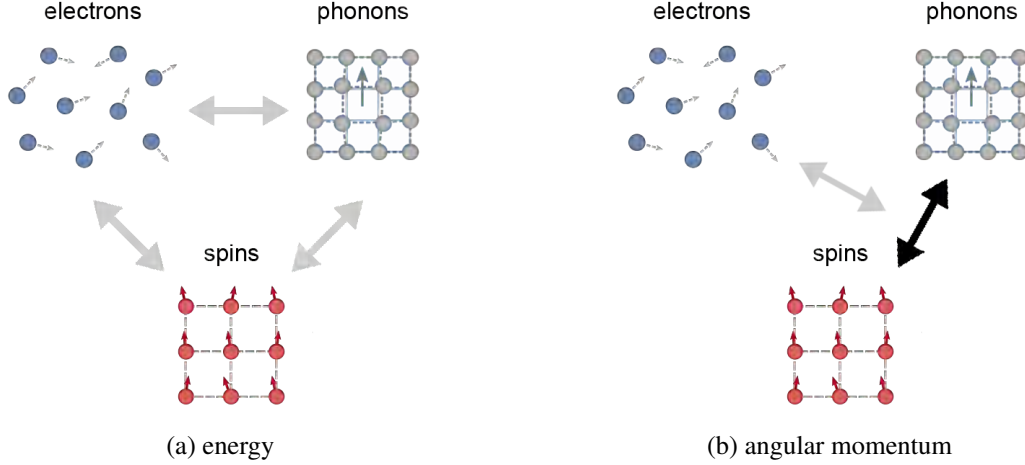
Figure 2.6: (a) Schematic representation of the energy transfer between the subsystems in the (M)3TM. (b) Schematic representation of the angular momentum transfer in the M3TM. Angular momentum is transferred between the phonon and spin subsystems due to e-p-s Elliot-Yafet spin-flip scattering.

A Weiss mean-field approach is used for the spin subsystem. The normalized magnetization is defined as

$$m = - \sum_{m_s=-S}^{S} m_s \frac{f_{m_s}}{S},$$ (2.3)

with spin quantum number S and where the occupation number for the energy levels of the spin system f_{m_s} is determined by Boltzmann statistics. The exchange splitting Δ_{ex} is given by

$$\Delta_{\mathrm{ex}} = \frac{3k_{\mathrm{B}}T_{\mathrm{C}}}{S+1}m,$$ (2.4)

where k_{B} is the Boltzmann constant and T_{C} the Curie temperature. The electron-phonon-spin interaction is introduced as a simple model Hamiltonian describing the Elliot-Yaffet spin-flip scattering with scattering probability a_{sf}. The resulting dynamics are determined using Fermi's golden rule. For $S = \frac{1}{2}$ this results in

$$\frac{\mathrm{d}m}{\mathrm{d}t} = R\frac{T_{\mathrm{p}}}{T_{\mathrm{C}}}m\left(1 - m\coth\left(m\frac{T_{\mathrm{C}}}{T_{\mathrm{e}}}\right)\right)$$ (2.5)

as the relation between m, T_{e} and T_{p}, where the prefactor R determines the demagnetization rate and is given by

$$R = \frac{8a_{\mathrm{sf}}g_{\mathrm{ep}}k_{\mathrm{B}}T_{\mathrm{C}}^2 V_{\mathrm{at}}}{(\mu_{\mathrm{at}}/\mu_{\mathrm{B}})E_{\mathrm{D}}^2},$$ (2.6)

with V_{at} the atomic volume, μ_{at} the atomic magnetic moment, μ_{B} the Bohr magneton and E_{D} the Debye energy.

2.2.2 M3TM for all-optical switching

So far, only one spin subsystem has been considered. In order to describe AOS in ferrimagnetic alloys, a second spin subsystem needs to be considered [40, 46]. The electron and phonon system are still

governed by equations 2.2. Both the spin subsystems (each representing one of the two sublattices, figure 2.3a) are described by a Weiss mean field approach. The exchange splitting $\Delta_{\mathrm{ex},i}$ for each of the spin systems ($i = 1, 2$) is given by

$$\begin{aligned}
\Delta_{\mathrm{ex},1} &= x\gamma_{1,1}m_1 + (1-x)\gamma_{1,2}m_2 \\
\Delta_{\mathrm{ex},2} &= (1-x)\gamma_{2,2}m_2 + x\gamma_{1,2}m_1,
\end{aligned} \tag{2.7}$$

with x the proportion of the sublattice 1 element(s) in the material, $\gamma_{i,j}$ the Weiss molecular field constants and m_i the (normalized) magnetization of spin subsystem i. Note that in agreement with equation 2.4,

$$\gamma_{i,i} = \frac{3k_{\mathrm{B}}T_{C,i}}{S_i + 1}. \tag{2.8}$$

The sign of $\gamma_{1,2}$ determines whether the sublattices are ferromagnetically or antiferromagnetically coupled, where a positive value results in ferromagnetic and a negative value in antiferromagnetic coupling.

(a)   (b)
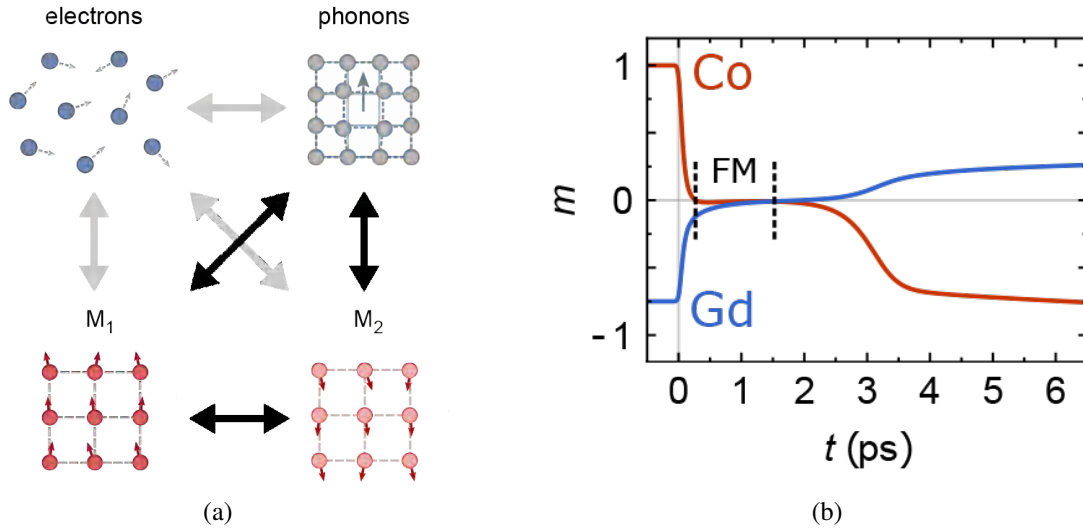
Figure 2.7: (a) Schematic representation of the energy and angular momentum exchange between the subsystems in the M3TM with two spin subsystems. The grey arrows indicate energy transfer, while the black arrows indicate both energy and angular momentum transfer. (b) AOS in a ferrimagnetic alloy in the M3TM with two spin subsystems. The transient ferromagnetic-like state is indicated with FM. From [46].

Energy is transferred between the electron, phonon and both the spin subsystems (figure 2.7a). Similar to the single-lattice M3TM, angular momentum is transferred from the spin subsystems to the phonon subsystems by Elliot-Yafet spin-flip scattering. Direct angular momentum transfer between the two sublattices is included by (direct) exchange scattering [40]. Exchange scattering consists of an electron-electron scattering event, where a spin in both subsystems is flipped during the event. The M3TM with two spin subsystems reproduces the experimental observation (figure 2.3b) of a transient ferromagnetic-like state during AOS in ferrimagnetic alloys (figure 2.7b).

In a similar manner, synthetic antiferromagnetic (Co/Gd) bilayers can be described with the M3TM [46]. For this purpose, the material is described in terms of atomic monolayers. The thermal electron and phonon system are considered to be homogeneous throughout the entire multilayer structure, but individual spin systems are assigned to each atomic monolayer. Again, a Weiss mean-field approach is used. Each atom is assumed to be only influenced by its nearest neighbours. Assuming the monolayers to

lie in the (111) plane of an fcc lattice, each atom has twelve nearest neighbours. Six of these neighbours are positioned in the same monolayer and three in each of the neighbouring monolayers. The exchange splitting in each monolayer i is now given by

$$\Delta_i = \frac{\gamma_{i,i-1}}{4} m_{i-1} + \frac{\gamma_{i,i}}{2} m_i + \frac{\gamma_{i,i+1}}{4} m_{i+1}. \tag{2.9}$$

Again, the same AOS dynamics (similar to figure 2.7b) are obtained from the (multilayer) M3TM [46]. The TM sublattice is switched first, giving rise to an intermediate ferromagnetic-like state. After the TM sublattice has recovered sufficiently, the RE is switched as well as a result of the AF coupling between the two sublattices. Furthermore, the threshold fluence for switching a synthetic antiferromagnetic bilayer increases with the TM layer thickness (figure 2.8a). The observed layer dependence is in agreement with the experimentally observed increase in threshold fluence for Pt/TM/Gd samples (figure 2.8b) [46]. All-optical switching is observed for a large range of TM layer thicknesses.

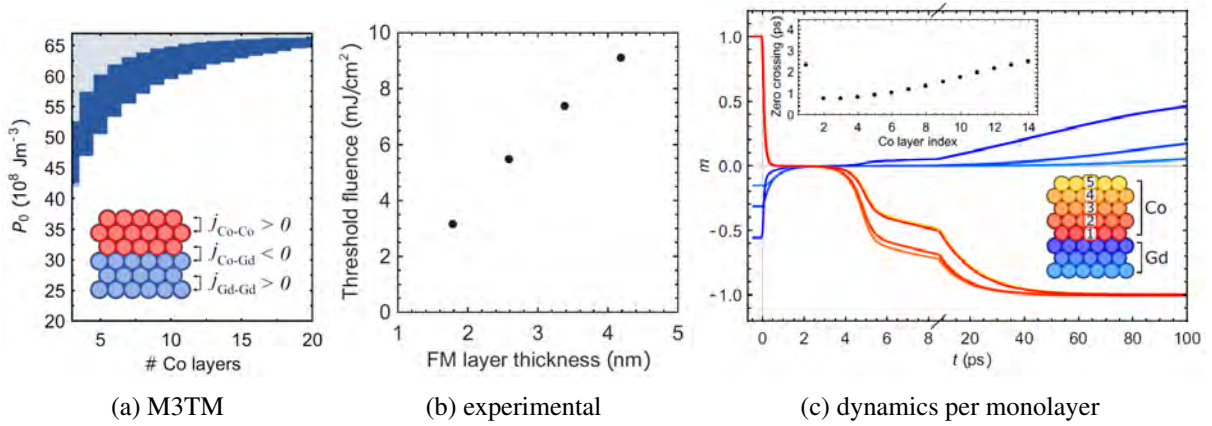|		
(a) M3TM	(b) experimental	(c) dynamics per monolayer

Figure 2.8: (a) Phase diagram for AOS as a function of laser energy P_0 and the number of Co monolayers in a Co/Gd bilayer in the M3TM. The white indicates the range where the laser energy is too low to switch the bilayer. The (dark) blue indicates switching. For the grey area, the phonon temperature exceeds the bilayer's Curie Temperature and the final state of the sample is expected to be a multidomain state. (b) Measurement of the AOS threshold fluence as a function of TM layer thickness, where the TM layer is composed of Co(0.2)/[Ni(0.6)/Co(0.2)]$_N$ multilayers ($N = 2, 3, 4, 5$). (c) AOS magnetization dynamics for the atomic monolayers in the M3TM for a Co/Gd bilayer with 5 Co and 3 Gd monolayers. The inset shows the time at which each Co monolayer's magnetization is reversed for a 14 Co layer system. (a), (b) and (c) from [46].

From the individual atomic monolayer's dynamics (figure 2.8c) the switching mechanism is extracted. The inset shows that the second TM monolayer from the TM/Gd interface switches first. The TM monolayer at the Co/Gd interface is strongly influenced by the AF exchange coupling with the Gd monolayer at the interface. Therefore, it switches at a later time. After the second monolayer has switched, as a result of exchange scattering between the neighbouring TM monolayers, each monolayer is consecutively switched. The M3TM thus assumes local angular momentum transfer between the spin subsystems to drive AOS in synthetic ferrimagnetic bilayers.

2.3 $s - d$ model

In this section a second model to describe laser induced effects in magnetic materials is introduced. The model is very similar to the M3TM. Again a magnetic material is described in terms of three subsystems. However, instead of a solely thermal conduction electron subsystem, the mobile electron system can carry angular momentum. The angular momentum carried by the mobile electron system is described in

terms of the spin accumulation μ_s, i.e. the difference in chemical potential for spin-up and spin-down, $\mu_s = \mu_\uparrow - \mu_\downarrow$. Furthermore, the driving microscopic mechanism for ultrafast magnetization dynamics is not Elliot-Yafet spin-flip scattering, but the $s - d$ exchange interaction.

2.3.1 $s - d$ model for a single macro spin

In the $s - d$ model, a material is described in terms of a phonon and two electron subsystems (figure 2.9), i.e. a mobile electron/spin and a localised electron/spin system ($4s$ and $3d$ in transition metals, respectively). Both electron systems can carry angular momentum. The mobile and local spin subsystems are coupled through the (on site) $s - d$ exchange interaction [31, 32, 47, 48]. Due to this $s - d$ interaction, angular momentum is transferred from the local to the mobile subsystem by spin-flip scattering of the mobile on the localized spins. For each scattering event, the total angular momentum is conserved.
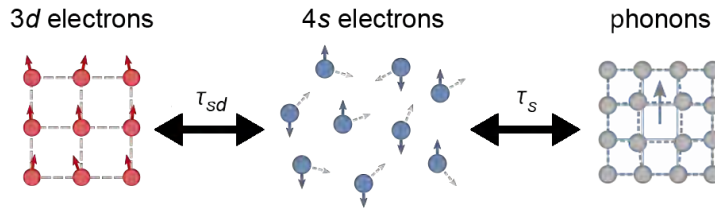

Figure 2.9: Schematic representation of the angular momentum and energy transfer between the three subsystems in the $s - d$ model. Adapted from [48].

Similar to the M3TM, the mobile s system is described as a free electron gas with uniform temperature T_e and the phonon subsystem by a Debye model with uniform temperature T_p. Temperatures T_e and T_p are given by the two temperature model (equation 2.2). The localised spin system is again described with a Weiss mean-field approach (equations 2.3 and 2.4). The spin dynamics due to the $s - d$ exchange coupling are determined using Fermi's golden rule. For $S = \frac{1}{2}$ this results in two equations for the magnetization of the localised spins m_d and spin accumulation μ_s [48],

$$
\begin{aligned}
\frac{\mathrm{d}m_d}{\mathrm{d}t} &= \frac{1}{\tau_{sd}}\left(m_d - \frac{\mu_s}{2k_\mathrm{B}T_\mathrm{C}}\right)\left(1 - m_d \coth\left(\frac{2m_d k_\mathrm{B}T_\mathrm{C} - \mu_s}{2k_\mathrm{B}T_\mathrm{e}}\right)\right), \\
\frac{\mathrm{d}\mu_s}{\mathrm{d}t} &= \rho_{sd}\frac{\mathrm{d}m_d}{\mathrm{d}t} - \frac{\mu_s}{\tau_s},
\end{aligned}
\tag{2.10}
$$

with timescale τ_sd closely related to the demagnetization rate. The parameter ρ_{sd} determines the feedback of the demagnetization on μ_s and is dependent on the density of states at the Fermi level and the $s - d$ exchange splitting [32, 48]. Angular momentum dissipates out of the (mobile) spin system at spin-orbit relaxation timescale τ_s [32, 48], e.g. through Elliot-Yafet spin-flip scattering. Note that the determination of parameters ρ_sd and τ_sd for a real system is not straightforward. Due to $s - d$ hybridization, the $3d$ and $4s$ electrons in a transition metal are not as divided in two distinct systems as assumed in the derivation of the equations above [48]. Furthermore, for $\tau_s \to 0$, any net spin accumulation vanishes instantly ($\mu_s = 0$) and the mobile electrons can be considered to be spinless. In this limit, equations 2.10 become mathematically equivalent to equation 2.5 in the M3TM. Finally, the total magnetization for $S = \frac{1}{2}$ is given by [48]

$$
m_\mathrm{tot} = m_d - \frac{\mu_s}{\rho_{sd}},
\tag{2.11}
$$

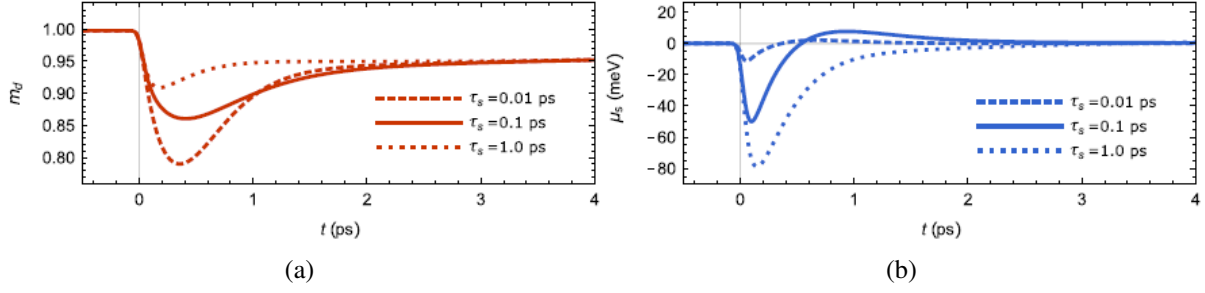which is conserved by the $s - d$ interaction.

Figure 2.10: (a) m_d and (b) μ_s as function of time as described by the $s - d$ model with a laser pulse arriving at $t = 0$ ps for different values of τ_s. Adapted from [48].

The experimentally observed ultrafast magnetization dynamics of a FM are reproduced by the $s - d$ model (figure 2.10a). Since spin accumulation generation is proportional to $\frac{\mathrm{d}m}{\mathrm{d}t}$, both a negative and positive μ_s is observed during demagnetization and remagnetization, respectively (solid line figure 2.10b). Furthermore, from figure 2.10 can be concluded that the spin accumulation μ_s counteracts the demagnetization of the local spin system. The longer the angular momentum dissipation time, the larger the spin accumulation and the less m_d demagnetizes.

2.3.2   Multilayer $s - d$ model

Since the $s - d$ model (in contrast to the M3TM) allows for the description of spin currents through the mobile (s) electrons, the $s - d$ model is used throughout this thesis to investigate non-local spin transport in TM/RE bilayers and FM/NM/TM/RE multilayers. The $s - d$ model is described in a multilayer implementation, similar to the multilayer M3TM that is introduced in section 2.2.2. The electron temperature T_e and phonon temperature T_p are considered to be homogeneous throughout the entire multilayer structure and are given by the two temperature model (equation 2.2). At time t_0 a laser pulse (Gaussian in time), with standard deviation σ and the absorbed laser fluence P_0 excites the systems,

$$P(t) = \frac{P_0}{\sigma\sqrt{\pi}} \exp\left(\frac{t - t_0}{\sigma}\right). \tag{2.12}$$

Each monolayer i is assigned a local magnetization $m_{d,i}$ as well as a spin accumulation $\mu_{s,i}$. The exchange splitting Δ_i in each monolayer is given by equation 2.9. Again, Fermi's golden rule is used to derive the dynamics,

$$
\begin{aligned}
m_{d,i} &= -\sum_{m_s=-S_i}^{S_i} m_s \frac{f_{m_s,i}}{S_i}, \\
\frac{\mathrm{d}f_{m_s,i}}{\mathrm{d}t} &= -(W_{m_s-1,m_s,i} + W_{m_s+1,m_s,i})f_{m_s,i} \\
&\quad + W_{m_s,m_s-1,i}f_{m_s-1,i} + W_{m_s,m_s+1,i}f_{m_s+1,i}, \\
\frac{\mathrm{d}\mu_{s,i}}{\mathrm{d}t} &= 2S_i\rho_{\mathrm{sd},i}\frac{\mathrm{d}m_{d,i}}{\mathrm{d}t} - \frac{\mu_{s,i}}{\tau_{s,i}} - \frac{\mu_{s,i} - \mu_{s,i\pm1}}{\tau_{\mathrm{eq},i}},
\end{aligned}
\tag{2.13}
$$

with $f_{m_s,i}$ the occupation numbers for each energy level m_s of a spin. The transition rates $W_{m_s\pm1,m_s,i}$ for transitions from energy level m_s to $m_s \pm 1$ are given by

$$W_{m_s\pm1,m_s,i} = \frac{1}{\tau_{\mathrm{sd},i}} \frac{\Delta_i - \mu_{s,i}}{2k_\mathrm{B}T_{C,i}} \frac{S_{m_s,i}^{\pm}}{2\sinh\frac{\Delta_i-\mu_{s,i}}{2k_\mathrm{B}T_\mathrm{e}}} \exp\left(\frac{\mp(\Delta_i - \mu_{s,i})}{2k_\mathrm{B}T_\mathrm{e}}\right), \tag{2.14}$$

and thus depend on a monolayer's demagnetization timescale $\tau_{\text{sd,i}}$, exchange coupling Δ_i, spin accumulation $\mu_{s,i}$ and Curie temperature $T_{\text{C},i}$ as well as on the electron temperature T_{e} [31, 32, 47, 48]. Furthermore, the spin ladder operator $S^{\pm}_{m_s,i}$ is defined as $S^{\pm}_{m_s,i} = S_i(S_i + 1) - m_s(m_s \pm 1)$.

The last term in the differential equation for $\mu_{s,i}$ (equation 2.13) describes equilibration of the mobile spin system of the monolayers at a timescale $\tau_{\text{eq},i}$, e.g. through diffusion of the mobile spins through the multilayer structure. The timescale τ_{eq} is assumed to be constant throughout the multilayer structure. Note that this definition of the equilibration term (last term in equation 2.13) assumes the density of states (DOS) of the s system to be homogeneous throughout the structure. In line with the assumption that the mobile electron temperature T_{e} is homogeneous throughout the entire structure, the mobile spin system is assumed to equilibrate (almost) instantly and the value $\tau_{\text{eq}} = 0.01$ fs is used.

Apart from angular momentum transfer through the mobile s spins, it is reasonable to expect a direct angular momentum transfer between the localised d spins, similar to the exchange scattering in the M3TM. An extra term $W^d_{m_s \pm 1, m_s, i}$ is added to the transition rate between energy levels $W_{m_s \pm 1, m_s, i}$ (equation 2.14). This term describes the direct angular momentum transfer between two monolayers' spin systems. Again, the assumption is made that each lattice site is only influenced by its nearest neighbours. For each monolayer i only contributions from monolayers $j = i \pm 1$ remain. Assuming the transfer rate is much slower than the equilibration of the s spin system, this direct angular momentum transfer is independent of μ_s. An exact derivation of $W^d_{m_s \pm 1, m_s, i}$ is beyond the scope of this research. Therefore, it is assumed that the mathematical form of $W^d_{m_s \pm 1, m_s, i}$ is equivalent to the exchange scattering term as derived in the M3TM [40]. The definition used by Beens *et al.* [46] is adopted, with the scattering rate constant $n_{i,j}$ linear proportional to the square of the exchange coupling constant ($j^2_{i,j}$). The proportionality is governed by the dimensionless parameter λ. By setting the parameter λ to zero, this direct angular momentum transfer can be excluded from the model. In reference [46] $\lambda = 5$ is used for the multilayer M3TM, where direct exchange scattering is the only channel for the angular momentum transport between monolayers.
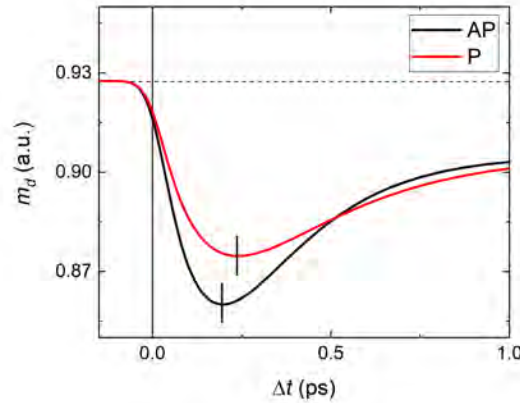
Figure 2.11: Laser induced magnetization dynamics for one of the two FM layers in a FM/NM/FM multilayer stack as described by the multilayer $s - d$ model ($\lambda = 0$). The material parameters that are used in reference [48] are adopted.

As previously mentioned, the multilayer $s - d$ model allows for the description of spin transport in multilayer structures. The experiment with two identical FM layers, separated by a conductive NM layer as depicted in figure 2.2 can thus be described with the multilayer $s - d$ model. The two identical FM layers are both modelled with a thickness of 5 monolayers. The NM spacer layer is modeled implicitly, by assuming that there is no exchange coupling between the two layers. The experimentally observed increased demagnetization rate for AP alignment, with respect to P alignment of the FM layers' magnetization (figure 2.11) is reproduced by the $s - d$ model.

The $s - d$ model is used throughout this thesis to investigate non-local spin transport in TM/RE bilayers and FM/NM/TM/RE multilayers. The AOS dynamics in synthetic ferrimagnetic bilayers in the multilayer $s - d$ model are compared to the dynamics in the multilayer M3TM. Furthermore, experimentally determined AOS threshold fluences as a function of layer thickness and time-resolved MOKE measurements of the switching dynamics are compared to the model's outcome. In the following chapter, however, first the experimental methodology is explained.

3 Experimental methodology

In this chapter, the experimental methods that are used throughout this thesis are explained. First, the magneto-optic Kerr effect (MOKE) is explained. Kerr microscopy is used to image all-optically switched magnetic domains in static switching measurements. From the size of the switched domains, the AOS threshold fluence is determined. Both demagnetization and switching dynamics are measured through time-resolved MOKE measurements. In the final section of this chapter, sample composition and fabrication is briefly explained.

3.1 Magneto-optic Kerr effect

The main experimental methods in this thesis are based on the magneto-optic Kerr effect [34, 49, 50]. The effect results from the difference in refractive index for left (LCP) and right circularly polarized (RCP) light as a result of a materials magnetization (linearly polarized light is a superposition of LCP and RCP light). Due to the difference in refractive index, upon reflection of a magnetic material a phase difference and difference between the LCP and RCP light is introduced. As a result, the linearly polarized light is rotated and an ellipticity is induced, as is schematically shown in figure 3.1.
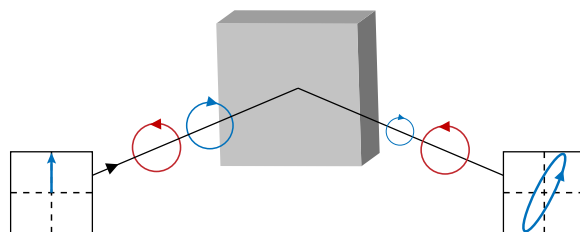
Figure 3.1: Schematic representation of the principle of MOKE. Due to the difference in refractive index for right and left circularly polarized light, the polarization for linearly polarized light is rotated upon reflection from magnetic sample. From [50].

(a) polar   (b) longitudinal   (c) transversal
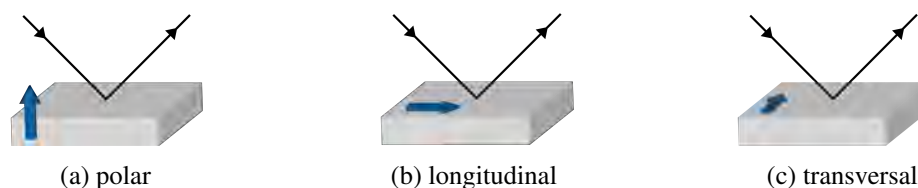
Figure 3.2: Schematic representation of the magnetization direction relative to the incident light in (a) polar, (b) longitudinal and (c) transversal MOKE. From [50].

3.1.1 Basic polar MOKE setup

The MOKE signal highly depends on the relative orientation of the incoming light and magnetization. Three different types of MOKE configurations can be distinguished, i.e. polar, longitudinal and transversal MOKE (figure 3.2). In polar MOKE the magnetization is directed normal to the surface (along the $z-$direction). Since out-of-plane (OOP) magnetized thin film samples are used throughout this thesis, polar MOKE is discussed in the remainder of this section. The largest MOKE contrast is obtained when the incident light travels along the $z-$direction, in other words normal to the surface. In this configuration, the magneto-optic response in an isotropic medium ($\epsilon_{xx} = \epsilon_{yy} = \epsilon_{zz}$) can be described in terms of the dielectric tensor,

$$\epsilon = \begin{pmatrix} \epsilon_{xx} & \epsilon_{xy} & 0 \\ -\epsilon_{xy} & \epsilon_{xx} & 0 \\ 0 & 0 & \epsilon_{xx} \end{pmatrix}, \tag{3.1}$$

with eigenmodes corresponding to RCP and LCP, respectively,

$$\begin{pmatrix} E_x \\ E_y \end{pmatrix}_{\pm} = \frac{1}{\sqrt{2}} \begin{pmatrix} 1 \\ \pm i \end{pmatrix}, \tag{3.2}$$

with E_x the $x-$ and E_y the $y-$component of the electric field and eigenvalues $\epsilon_{\pm} = \epsilon_{xx} \pm i\epsilon_{xy}$. Since ϵ_{xy} depends on the magnetization, reflected linearly polarized light will experience a magnetization dependent complex rotation Φ. For an semi-infinite medium, Φ is given by

$$\Phi = \theta + i\varepsilon = \frac{\epsilon_{xy}}{\sqrt{\epsilon_{xx}(\epsilon_{xy} - 1)}}, \tag{3.3}$$

with Kerr rotation θ and Kerr ellipticity ε [34, 50].
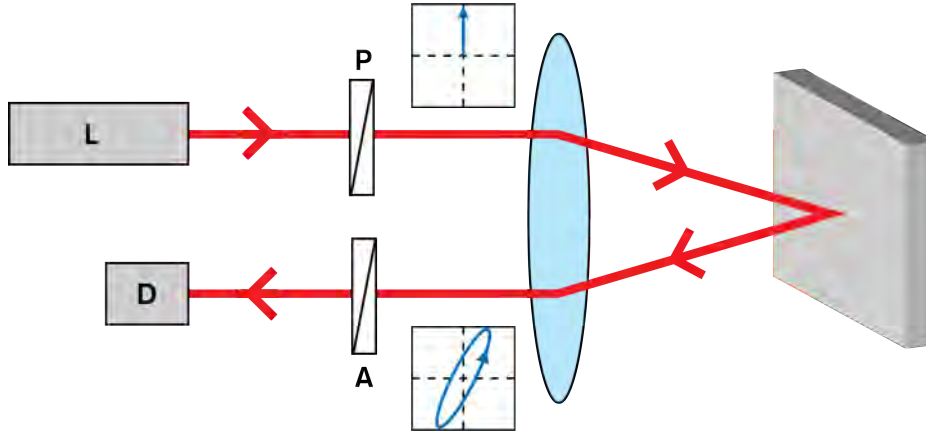
Figure 3.3: Schematic representation of a basic MOKE setup with laser L, photodetector D and almost crossed configuration of polarizer P and analyzer A.

In the most simple experimental MOKE setup (figure 3.3), laser light is linearly polarized by a polarizer P, before it is focused onto the sample with a lens. Consequently, the linearly polarized light will be rotated over complex angle Φ before passing through a second polarizer, which is called analyzer A, at an angle γ with respect to P. The resulting intensity I of the light at the detector can be calculated through the Jones formalism. Its γ dependence is given by [50]

$$I \propto \cos^2 \gamma + (\theta^2 + \varepsilon^2) \sin^2 \gamma + \theta \sin 2\gamma \approx \cos^2 \gamma + \theta \sin 2\gamma, \tag{3.4}$$

where the term proportional to $(\theta^2 + \varepsilon^2)$ is expected to be negligible due to the generally small values of θ and ε. For a cross configuration ($\gamma = \frac{\pi}{2}$), both the non-magnetic background ($\propto \cos \gamma$) and magnetic signal ($\propto \sin 2\gamma$) are zero. However, expansion around equilibrium angle $\gamma_0 = \frac{\pi}{2}$ gives

$$I \propto 2\theta\Delta\gamma + \Delta\gamma^2, \tag{3.5}$$

with $\Delta\gamma = (\gamma - \gamma_0)$. The magnetic signal scales with $\Delta\gamma$, the non-magnetic with $\Delta\gamma^2$. In other words, around γ_0, the magnetic signal is more sensitive to small changes in γ than the non-magnetic background. Consequently, the MOKE signal can be optimized by setting A almost perpendicular to P.

3.1.2 Kerr microscopy

A Kerr microscope is used to image all-optically switched domains. A Kerr microscope is similar to a regular microscope, but contains (among others) polarizers in order to measure magnetic contrast through Kerr rotation or ellipticity. This is achieved by implementing a basic MOKE setup in a microscope. A conventional basic MOKE setup uses the reflection of a single laser beam and is only sensitive to the magnetization at the spot where the beam is reflected. The advantage of Kerr microscopy is that the magnetic contrast can be spatially resolved, resulting in a 2D image of the (relative) magnetization in the sample. In this way, magnetic domains can be imaged. A CCD camera is mounted on top of the Kerr microscope, to record the image.

3.1.3 Modulation with photo-elastic modulator

As mentioned in the section 3.1.1, the expected Kerr rotation θ is very small. In order to increase the signal-to-noise ratio of the MOKE signal, polarization modulation is employed. For this modulation, a photo-elastic modulator (PEM) is used. A PEM consists of a periodically compressed birefringent crystal. As a result, a periodical phase difference is induced between LCP and RCP light. The PEM is placed in the laser path between the polarizer P and the lens (figure 3.4). With P set at an angle $\frac{\pi}{4}$ with respect to the main axis of the PEM, the resulting modulated light can be expressed as

$$\begin{pmatrix} E_x \\ E_y \end{pmatrix} = \frac{1}{\sqrt{2}} \begin{pmatrix} 1 \\ e^{iA\cos\Omega t} \end{pmatrix} \tag{3.6}$$

with A the amplitude of retardation between the electric field components, and $f = \frac{\Omega}{2\pi}$ the modulation frequency (50 kHz). Note that when $A = \frac{\pi}{2}$, the light oscillates between LCP and RCP with frequency f.
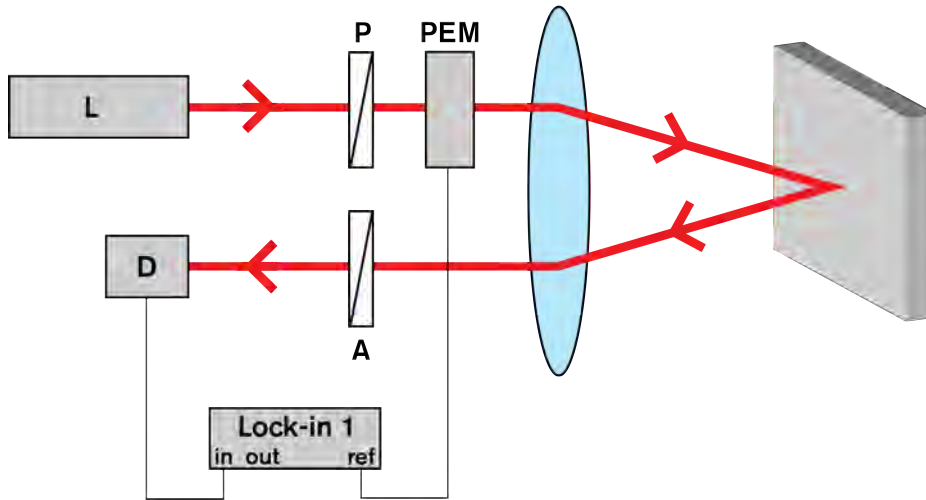
Figure 3.4: MOKE setup with polarization modulation. The PEM allows for measuring the Kerr rotation or ellipticity with a lock-in amplifier in the first or second harmonic, respectively.

The Jones formalism gives

$$I \propto \frac{1}{2} + \theta \cos|A\cos\Omega t| + \varepsilon \sin|A\cos\Omega t|, \tag{3.7}$$

with analyzer A oriented along the main axis of the PEM ($\gamma = \frac{\pi}{4}$). Expansion of equation 3.7 into spherical harmonics gives [50]

$$I_{1f} \propto \varepsilon J_1(A) \cos \Omega t \tag{3.8}$$

and

$$I_{2f} \propto \theta J_2(A) \cos 2\Omega t \tag{3.9}$$

for the first and second harmonics, respectively, with the first and second spherical Bessel functions of the first kind are denoted as $J_1(x)$ and $J_2(x)$, respectively. Consequently, a lock-in amplifier can be used to measure the Kerr ellipticity or Kerr rotation by locking into the first or second harmonic signal, respectively.

3.1.4   Time-resolved MOKE

In order to measure demagnetization and switching dynamics a pump-probe setup is used (figure 3.5). A beam splitter is placed in a pulsed laser's path, transmitting 90% of the light. The reflected part of the pulse (10%) is used to probe the magnetization. Similar to the basic MOKE setup, the polarizers P and A and the PEM are placed in the path of the probe. The transmitted pulse is used to excite (pump) the magnetic samples. By varying the path length of the probe (or pump), the time delay Δt between the pump and probe pulse is altered and a time-resolved MOKE (TR-MOKE) signal is obtained.
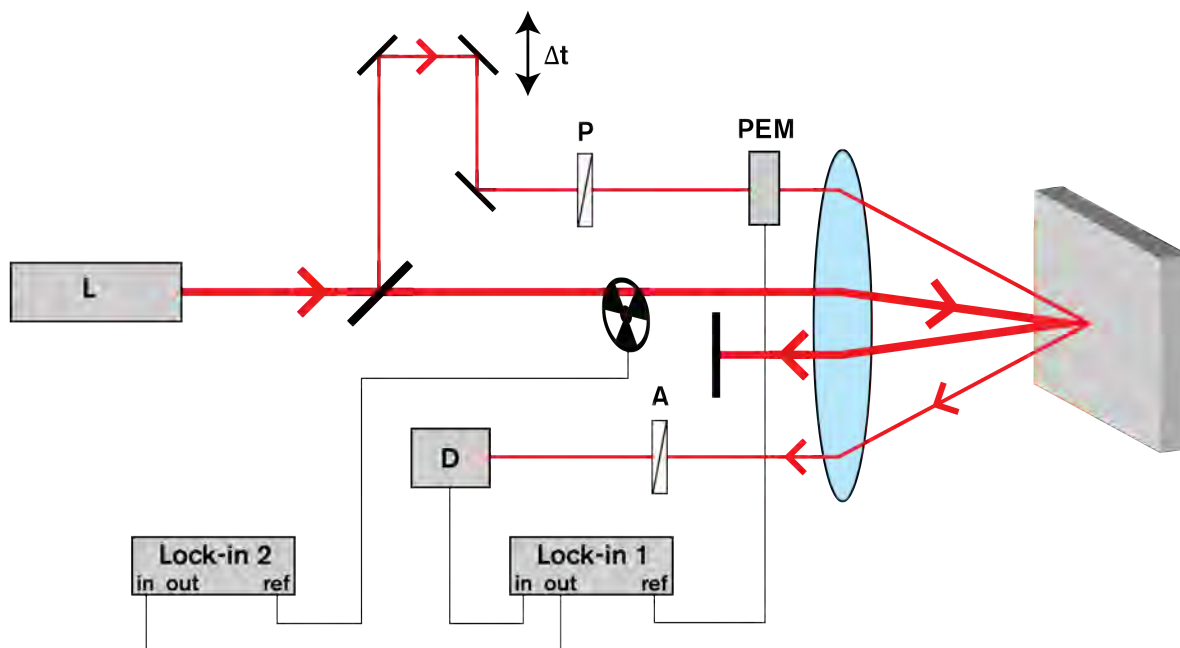
Figure 3.5: TR-MOKE setup. A beam splitter separates pump and probe. The length of the path of the probe can be adjusted to measure the magnetization as a function of the time delay Δt between pump and probe. The signal-to-noise ratio is reduced with a second lock-in amplifier that is locked to the frequency of the chopper in the path of the pump .

When the total pump-induced demagnetization is small, the change in the Kerr rotation and ellipticity is small as well and barely any signal is measured with the lock-in amplifier. To increase the signal size and improve the signal-to-noise ratio in the TR-MOKE setup, a chopper is placed in the path of the pump. The chopper modulates the pump intensity ($f_{\text{chop}} \approx 70$ Hz). By feeding the output of lock-in 1 to a second lock-in amplifier with reference frequency f_{chop}, it is possible to lock into the pump-induced change in the MOKE signal.

Throughout this thesis, demagnetization measurements are performed with a pulsed Ti:Sapphire laser with a pulse duration of approximately 100 fs, wavelength of 780 nm and a repetition rate of 80 MHz. For all demagnetization measurements the chopper was used. For the measurement of the all-optical switching dynamics a laser (Spirt-NOPA) with wavelength of 700 nm, repetition rate of 500 kHz and again a pulse duration of approximately 100 fs is used. Both with and without chopper in the pump path, a measurable pump-induced signal is found. The repetition rate of the Spirit-NOPA can be reduced with a pulse picker. The pulse picker and a mechanical shutter are also used in static switching experiments to select individual pulses. Note that for both lasers' wavelength, the MOKE signal is expected to mostly probe the Co contribution to the Co/Gd bilayer's magnetization [44, 51].

(a) raw data   (b) separated magnetic and non-magnetic signal
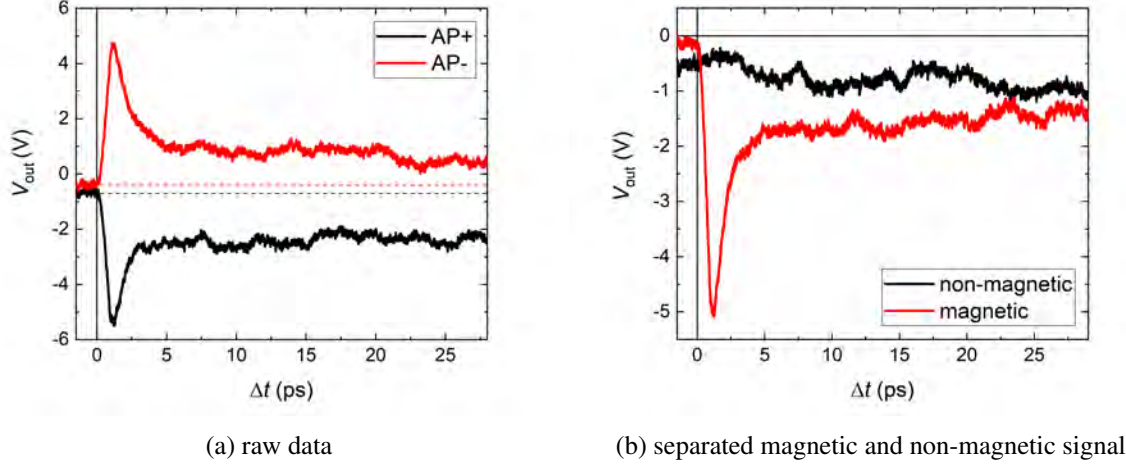
Figure 3.6: (a) 'Raw' data obtained by averaging over five measurements of the TR-MOKE signal on a [Co/Ni]$_4$/Co/Cu/Pt/Co sample in AP+ and AP- configuration. (b) By separating the symmetric and antisymmetric part of the measured signal, the non-magnetic signal is separated from the magnetic signal.

3.1.5   Subtracting non-magnetic contributions

Non-magnetic contributions to the time-resolved signal can occur, for example as a result of a small imperfection in the alignment of the delay line. Fortunately, these non-magnetic signals can easily be isolated. The magnetic signal is asymmetric with respect to the magnetization, i.e. a positive magnetization results in exactly the opposite TR-MOKE signal with respect to a negative magnetization. However, the non-magnetic background does not change when the magnetization is switched. By measuring for both positive and negative magnetization, the magnetic signal can be isolated. In figure 3.6a the output signal V_{out} of lock-in 2 for a demagnetization measurement on a FM/NM/TM/RE magnetic multilayer sample is plotted for both AP+ and AP- configuration. The non-magnetic and magnetic signals are determined as

$$V_{\text{out,non-magnetic}} = \frac{V_{\text{out},+} + V_{\text{out},-}}{2} \qquad (3.10)$$

and

$$V_{\text{out,magnetic}} = \frac{V_{\text{out},+} - V_{\text{out},-}}{2}, \qquad (3.11)$$

respectively. The resulting non-magnetic and magnetic signals are shown in figure 3.6b.

3.1.6 Depth-resolved (TR-)MOKE

In a conventional TR-MOKE measurement on a magnetic multilayer sample, the measured signal contains the combined responses of the different layers. An individual layer's response unfortunately, can not easily be distinguished. However, by adding one optical component, it is possible to isolate the individual layer's contributions [52].
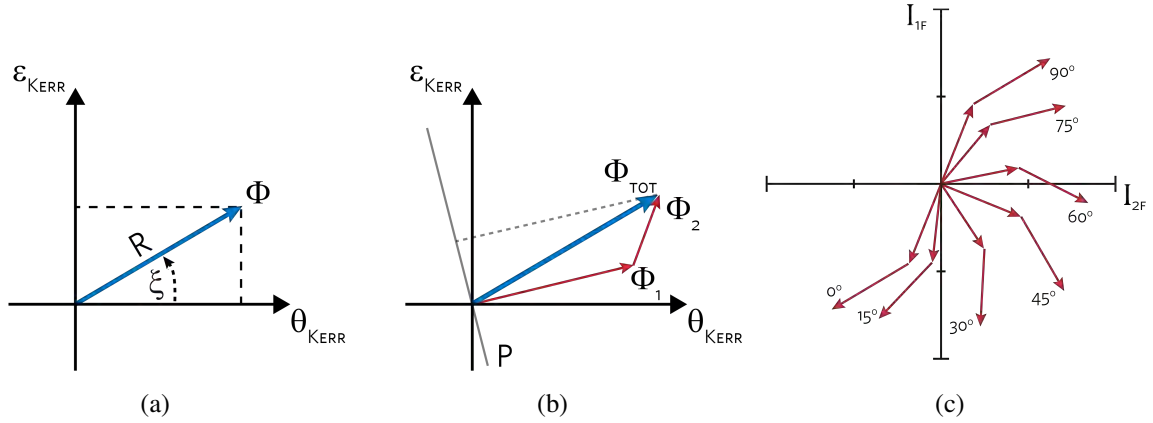
Figure 3.7: (a) Kerr rotation Φ in the Kerr plane. (b) The total Kerr rotation Φ_{tot} in the Kerr plane for a magnetic bilayer sample consists of the sum of the Kerr rotations for the individual layers. In a conventional MOKE measurement, the projection of Φ_{tot} on the $\theta-$axis (or $\varepsilon-$axis) is measured. By measuring along the projection axis P (orthogonal to Φ_1) the Φ_2 contribution is isolated. (c) Schematic representation of the change of I_{1f} and I_{2f} with QWP angle α. Adapted from [50].
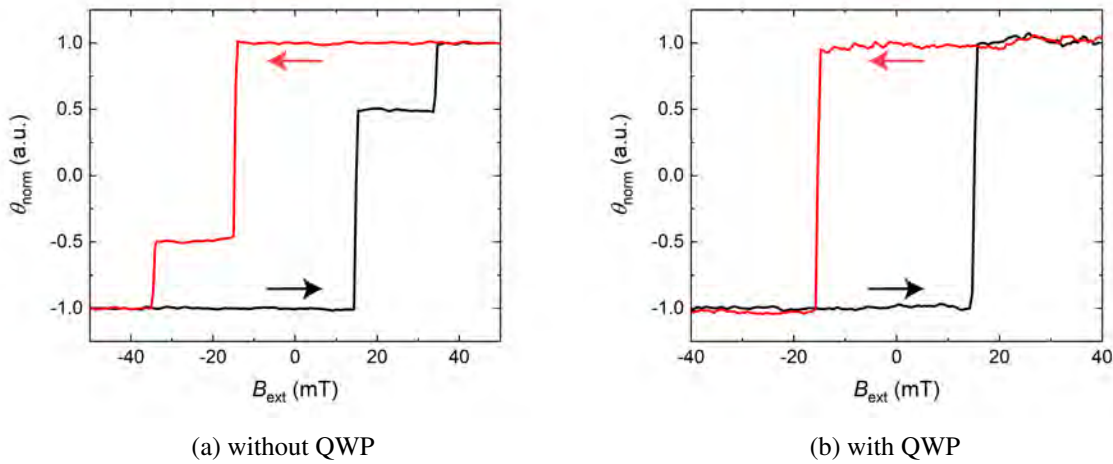
Figure 3.8:   (a) Normalized polar MOKE measurement of the hysteresis loop for a [Co/Ni]$_4$/Co/Cu/Pt/Co/Gd thin film sample without the use of a QWP. The arrows indicate the direction of the field sweep. The sample clearly exhibits PMA for both magnetic layers. The low coercivity step corresponds to a switch of the Co/Ni magnetization, whereas the Co/Gd bilayer exhibits a higher coercivity. (b) By adding a QWP to the probe path and setting the correct angle α, the contribution by the Co/Gd bilayer is eliminated from the measured MOKE signal. Only the Co/Ni contribution remains.

In order to understand this approach, the magnetic response is described in the Kerr plane spanned by θ and ε (figure 3.7a) [52, 53]. The complex Kerr rotation Φ can be assigned an amplitude R and angle ξ. For a magnetic multilayer sample, the total Kerr rotation Φ_{tot} is equal to the sum of the Kerr rotations

Φ_i of the individual layers, as shown in figure 3.7b. A quarter-wave plate (QWP) is implemented at an angle α with respect the PEM's main axis. Conventionally, the Kerr rotation θ can be measured in the second harmonic I_{2f}, whereas Kerr ellipticity ε is found in first harmonic I_{1f}. However, by rotating the angle α the sensitivity of the first and second harmonic to θ or ε can be changed (figure 3.7c). This change can again be calculated with the Jones formalism, giving [52]

$$\begin{pmatrix} I_{1f} \\ I_{2f} \end{pmatrix} \propto \begin{pmatrix} -\sin^2 2\alpha & -\cos 2\alpha \\ -cos2\alpha & sin^2 2\alpha \end{pmatrix} \begin{pmatrix} \varepsilon \\ \theta \end{pmatrix}. \tag{3.12}$$

It is possible to chose α such, that Φ_{tot} is projected on an axis P where only the Kerr rotation by one of the magnetic layers contributes to the signal, i.e. Φ_2 in figure 3.7b. This is experimentally verified by performing a static MOKE measurement on a magnetic multilayer sample. In figure 3.8 the normalized Kerr signal θ_{norm} is shown for both a measurement without and with QWP, respectively. Note that the amplitude of the Φ_2 signal that is projected on axis P (figure 3.7b) depends on the angle between the Kerr rotations Φ_1 and Φ_2. An angle of $\frac{\pi}{2}$ results in the optimal signal. When the angle between Φ_1 and Φ_2 is small, the on P projected Φ_2 signal is small as well (figure 3.7b).

3.1.7 Minimizing coherent contributions due to pump-probe overlap

Time-resolved pump-probe measurements can contain coherent artifacts at zero delay (i.e. when pump and probe overlap) [54, 55, 56, 57, 58]. A significant contribution to these coherent artifacts originates from interference between pump and probe [54, 55, 58]. Furthermore, the pump is expected to induced a (temporary) change in the dielectric tensor [56], e.g. due to the so-called 'specular inverse Faraday effect' (SIFE) and 'specular optical Kerr effect' (SOKE) [57, 59]. One would expect the pump-probe interference to disappear when the pump and probe beam are polarized perpendicular to each other. However, although the magnitude of the coherent spikes is reduced, third order effects still cause coherent contributions to the signal in the case of perpendicular polarization [55, 58].
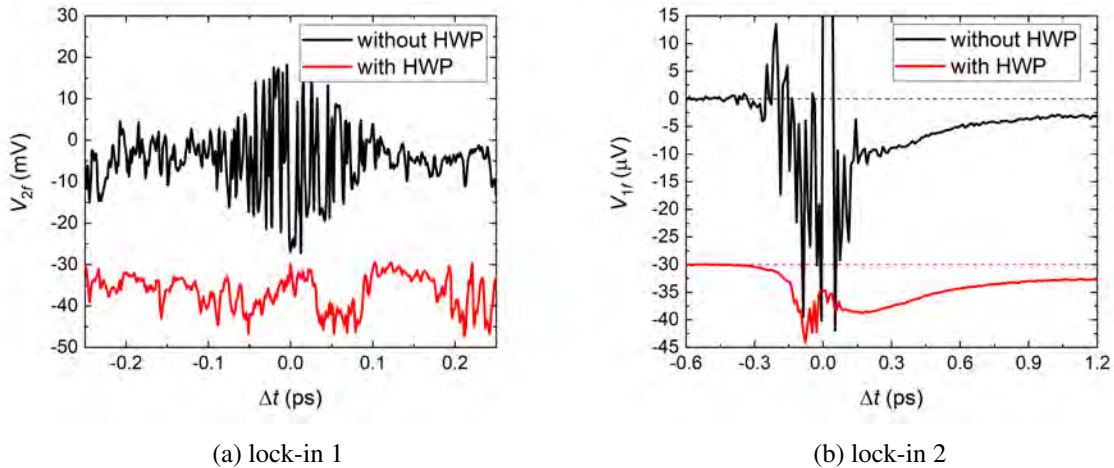
(a) lock-in 1   (b) lock-in 2

Figure 3.9: (a) Single measurement of the second harmonic voltage in lock-in 1 and (b) first harmonic voltage in lock-in 2 after averaging over twenty measurements. Measurements are performed on a $[Co/Ni]_4/Co/Cu/Pt/Co/Gd$ thin film sample. By inserting a HWP in the pump path, the interference at zero delay is effectively removed from the signal in lock-in 1. The pump-induced signal in lock-in 2 is no longer dominated by this interference. Note that measurement with HWP was translated vertically in order to clearly distinguish it from the measurement without HWP.

It has experimentally been shown [58] that the coherent interference contribution in a pump-probe measurement on InP can be reduced by placing a polarizer in front of the detector, perpendicular to the

pump's polarization. Since analyzer A is already in place in front of the detector, a half-wave plate (HWP) is placed in the path of the pump in order to rotate it's polarization such that the interference signal that passes the analyzer A is minimum. As shown in figure 3.9a, by adjusting the pump's polarization, the coherent 'beat' in lock-in 1 is removed from the signal or at least reduced to a level smaller than the noise level. In lock-in 2 the signal is no longer dominated by this coherent 'beat' (figure 3.9b) and only the demagnetization trace and a coherent peak remain. The presence of this coherent peak is not expected to influence the magnetization dynamics [57]. As the pump-probe interference is minimized, the coherent peak is mainly attributed to the specular inverse Faraday effect and specular optical Kerr effect.

3.2 Sample fabrication

In this section sample fabrication and optimization are discussed. All experiments throughout this thesis are performed on thin film multilayer samples fabricated by DC magnetron sputtering [60] at room temperature (with a base pressure of $10^{-7} - 10^{-8}$ mbar). A seeding layer consisting of 4 nm Ta and 4 nm Pt, respectively, is sputtered onto every substrate to ensure proper growth and the desired perpendicular magnetic anisotropy (PMA). All samples are capped by a 4 nm Ta capping layer.

The main magnetic thin film samples that are used throughout this thesis are the magnetic multilayers for spin current assisted, i.e. [Co(0.2)/Ni(0.9)]$_4$/Co(0.2)/Cu(5)/Pt(0.5)/Co(t_{Co})/Gd(3) (see figure 1.6 for a schematic overview of the magnetic multilayer). The numbers between parentheses indicate the layer thicknesses in nm. The thickness of the Co layer that is part of the Co/Gd bilayer t_{Co} is varied. Due to the strong ferromagnetic coupling in the [Co/Ni]$_4$/Co multilayer, the [Co/Ni]$_4$/Co multilayer is treated as a single ferromagnetic CoNi layer with a thickness $t_{CoNi} = 4.6$ nm in the remainder of this thesis. Similar to the 4 nm thick Pt layer that is part of the seeding layer, the intermediate 0.5 nm thick Pt layer is added to ensure PMA in the Co/Gd bilayer.

In order to compare the P and AP configuration of the CoNi/Cu/Pt/Co/Gd multilayer, a significant difference in the coercive field of the CoNi reference layer and the Co/Gd bilayer (figure 3.8a) is essential. Such a plateau in the hysteresis loop allows the sample to be set in an AP state by means of an applied field. When the coercivities of the two magnetic layers lie too closely together, the sample can not be initialized in AP configuration.

The static switching measurements and the time-resolved demagnetization measurements that are discussed in sections 4.2, 4.3.1 and 4.3.2 of the next chapter, are performed on silicon (or degenerately doped Si:B) substrates with a 100 nm thick oxidized capping layer, i.e. Si/SiO$_2$(100) (or Si:B/SiO$_2$(100)). In order to measure the switching dynamics in the TR-MOKE setup (discussed in section 4.3.3), the sample needs to be pumped continuously (repetition rate 100 - 500 kHz). In order to prevent sample damage due to heat accumulation in the multilayer, the AOS dynamics are measured on degenerately doped Si:B substrates, which exhibit a higher thermal conductivity due to the absence of the 100 nm thick SiO$_2$ (for more information see appendix A).

4   Results and discussion

The research findings are reported in this chapter. The applicability of the multilayer $s - d$ model (section 2.3.2) to AOS in synthetic ferrimagnetic bilayers and the subsequent switching dynamics are investigated. Spin current assisted AOS is modelled in the multilayer $s - d$ model. Next, the experimental results are discussed. The static switching behavior in synthetic ferrimagnetic bilayers and FM/NM/Co/Gd multilayer samples is compared to the $s - d$ model's predictions. Furthermore, some measurements on a Co/Gd/NM/FM multilayer are performed in order to investigate the effect of reversing the deposition order of the free and reference layer. The final section, contains time-resolved MOKE measurements of the dynamics in FM/NM/Co/Gd multilayer samples. First, low fluence demagnetization measurements are discussed, both for the first 2 ps and on a longer time scale (up to 50-500 ps). Then, TR-MOKE measurements of spin current assisted AOS are discussed.

4.1   AOS in the multilayer $s - d$ model

In this section, the multilayer $s - d$ model is employed to investigate the behavior of AOS in synthetic ferrimagnetic bilayers and magnetic multilayers as a result of conduction electrons. First, a Co/Gd bilayer is modelled. The Co/Gd switching dynamics and mechanism as predicted by the $s - d$ model are extracted. Furthermore, the behavior of the AOS threshold fluence as function of Co layer thickness is discussed. In the final part of this section, the $s - d$ simulations on a FM/NM/Co/Gd multilayer are introduced.
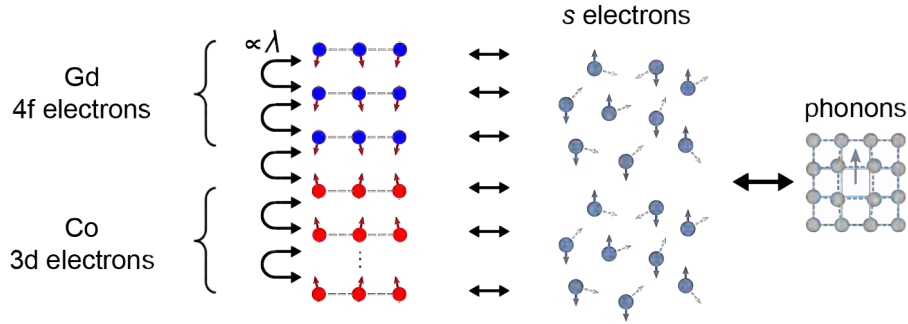
Figure 4.1: Schematic representation of the Co/Gd bilayer in the $s - d$ model. The arrows indicate the transfer of angular momentum. The direct angular momentum exchange between monolayers is proportional to dimensionless parameter λ and can be excluded from the model by setting $\lambda = 0$.

4.1.1   Macroscopic dynamics for Co/Gd bilayers

Throughout this thesis, synthetic ferrimagnetic Co/Gd bilayers are modelled for a varying number of Co monolayers n_{Co}. The number of Gd monolayers is set to three. In figure 4.1 a schematic representation of the Co/Gd bilayer is shown. Dimensionless parameter λ governs the direct angular momentum exchange between the local d systems of neighbouring monolayers (section 2.3.2). Initially, λ is set to zero. Consequently, only the $s - d$ interaction facilitates angular momentum transfer to and from the monolayers' local spin systems. The mobile s system transfers angular momentum between the monolayers. The used material properties are listed in appendix B. In this and the following subsections the $s - d$ model is employed in order to investigate whether angular momentum transport by itinerant electrons alone can explain AOS in synthetic ferrimagnetic bilayers.

The bilayer's magnetization dynamics with $n_{\mathrm{Co}} = 5$ are modelled (figure 4.2). As is shown in the figure, it is possible to switch the Co/Gd bilayer as a result of the angular momentum transported by the s system. For a positive m_{d}, the (localized) majority electrons are spin-polarized in the 'down'

direction. The demagnetization of the Co layer thus generates a negative spin accumulation. As a result, a large negative spin accumulation is observed within the first ps (figure 4.2a). On a slightly longer timescale, the generated μ_s mainly originates from the slower Gd demagnetization and is positive. This positive μ_s causes the Co magnetization to cross zero. Again, a transient ferromagnetic-like state is observed before the Gd magnetization is switched as well. The ferromagnetic-like state is observed for a relatively long time delay (compared to for example figures 2.7b and 2.8c). This is attributed to the fact that $\lambda = 0$ and thus no direct angular momentum is transferred between monolayers. Instead the spin accumulation drives the switch of the magnetization and μ_s is dominated by the Gd demagnetization for $\Delta t = 3 - 13$ ps approximately. Furthermore, a 'bump' in the Gd magnetization is found at a time delay Δt of approximately 18 ps. This bump is attributed to the spin accumulation generated by the remagnetization of the Co.
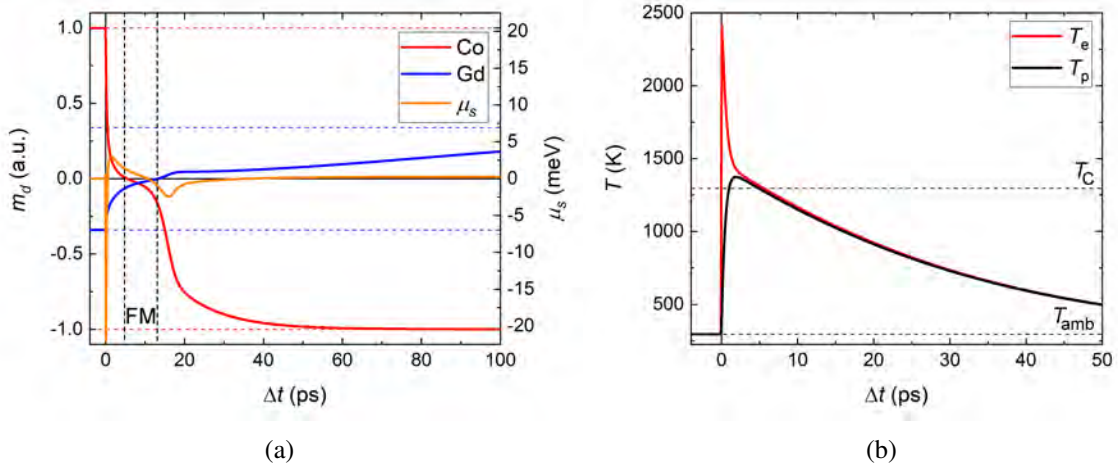

(a)   (b)

Figure 4.2: (a) m_d, μ_s, (b) T_e and T_p dynamics for a Co/Gd bilayer ($n_{Co} = 5$) in the multilayer $s - d$ model ($\lambda = 0$) after excitation with a laser pulse ($P_0 = 66 \cdot 10^8 \, \frac{J}{m^3}$). The vertical dashed lines in (a) indicate the transient ferromagnetic-like (FM) state. The horizontal dashed lines in (b) indicate the ambient temperature ($T_{amb} = 295$ K) and the Co/Gd bilayer's Curie temperature as determined from the Weiss model ($T_C = 1296$ K).

4.1.2   Co/Gd dynamics per monolayers

By looking at the switching dynamics of the individual Co monolayers, the switching mechanism is determined. The moment a monolayer's magnetization is switched, is defined as the moment the local magnetization m_d crosses zero, i.e. the sign of m_d changes from positive to negative or vice versa. The time delay Δt at which the magnetization m_d of the Co monolayers crosses zero is extracted from the $s - d$ simulations (figure 4.3). For the M3TM (see section 2.2.2, figure 2.8c), the switch of a Co/Gd bilayer initiates at the Co/Gd interface. As a result of direct exchange scattering between the Co monolayers, each neighbouring monolayer is then consecutively switched. In the multilayer $s - d$ model with $\lambda = 0$, this direct exchange scattering has been excluded from the model. Angular momentum is transferred between monolayers through the mobile s system.

Figure 4.3 shows that for $\lambda = 0$, the switch does not initiate at the Co/Gd interface. Instead, the Co layer that is the furthest away from the Co/Gd interface is the first layer that reverses its magnetization. These switching dynamics result from a combination of two factors. The first factor is the effective exchange coupling for each monolayer. The other is the assumption that the spin accumulation μ_s equilibrates almost instantly ($\tau_{eq} = 0.01$ fs). The outer Co monolayer ($i = 1$) has only one neighbouring layer and thus experiences the smallest exchange coupling (equation 2.9). On the other hand, the Co monolayer at the Co/Gd interface ($i = 5$) is strongly influenced by the antiferromagnetic exchange coupling with the

Gd. Since μ_s equilibrates almost instantly, its effect on the Co magnetization is approximately the same for every monolayer. Consequently, the outer Co monolayer switches first, whereas the Co monolayer at the Co/Gd interface is the last to switch.
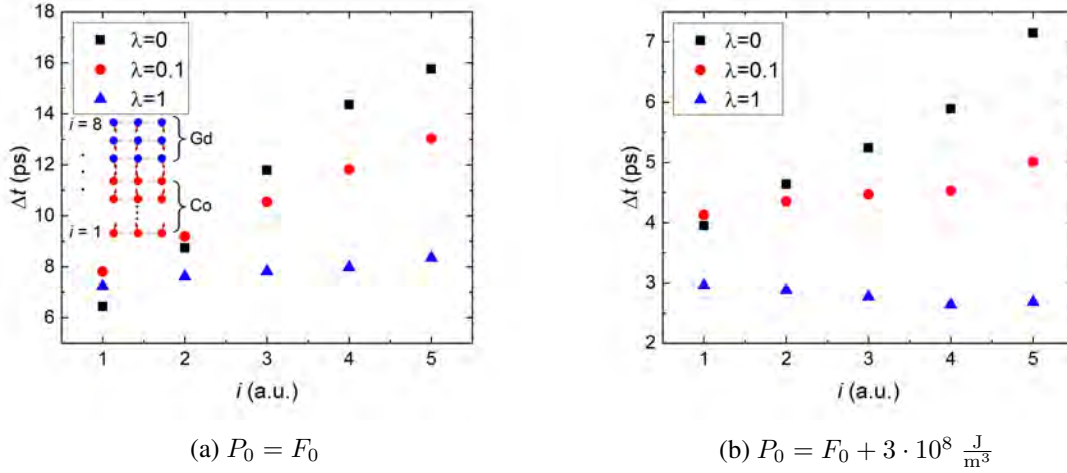

(a) $P_0 = F_0$ (b) $P_0 = F_0 + 3 \cdot 10^8 \; \frac{J}{m^3}$

Figure 4.3: Time delay Δt at which the (localized) magnetization of each monolayer i crosses zero as modeled for a Co/Gd bilayer ($n_{Co} = 5$) in the multilayer $s - d$ model for varying λ with a laser fluence (a) at and (b) above the threshold fluence. The inset in (a) shows a schematic representation of the Co/Gd structure.

Next, the direct angular momentum transfer between adjacent monolayers' local spin systems is included ($\lambda > 0$). When the simulated laser fluence P_0 is set equal to the AOS threshold fluence F_0 (figure 4.3a), the previously discussed switching mechanism is recovered for all simulated λ values. However by increasing the amount of angular momentum that is transferred through the direct exchange coupling between the localized d systems, the time in which all Co monolayers reverse their magnetization is reduced. This faster switching behavior can be easily understood from the fact that an increasingly efficient angular momentum transfer channel is added to the system.

When the pump fluence is increased to values above F_0 (figure 4.3b), the monolayer dynamics for $\lambda > 0$ start to deviate from the $\lambda = 0$ case. For the $\lambda = 0.1$ case, the direct angular momentum exchange is relatively small and the effect is small. However, for $\lambda = 1$, the switching mechanism is found to be different. The same switching mechanism as for the multilayer M3TM (figure 2.8c) is recovered, where the monolayers at the Co/Gd interface are the first to switch (figure 4.3b). This effect is attributed to fact that the direct angular momentum transfer rate increases with the electron temperature.

4.1.3 Threshold fluence of Co/Gd bilayers

Not only the switching mechanism, but also the threshold fluence F_0 is influenced by the direct angular momentum transfer between neighbouring d subsystems. The behavior of F_0 as a function of Co layer thickness is investigated for different values of lambda. The bilayer's Curie temperature T_C is determined from the Weiss model. First consider the $\lambda = 0$ case. The found values for F_0 are such that the phonon temperature T_p (temporarily) exceeds the bilayer's T_C (figure 4.2b and 4.4). At temperatures above T_C, a real FM sample loses its permanent magnetic properties. Upon cooling down to temperatures below T_C, the sample is expected to remagnetize into a multidomain state. In real samples at these high fluences, AOS is thus not expected to be found.

The model, however, can still be employed to qualitatively investigate the influence of itinerant electrons on F_0 as a function of the Co layer thickness. The threshold fluence is found to be increasing with the number of Co monolayers n_{Co} (figure 4.4). At small Co thickness (up to approximately 8 monolayers)

the found n_{Co} dependence is similar to that of the multilayer M3TM and experimental observations on FM/Gd bilayer samples (figure 2.8). For $n_{Co} > 8$, however, instead of a decreasing slope (M3TM), in the multilayer $s-d$ simulations an increasing slope is observed. In the $s-d$ model (for large layer thickness), all-optically switching thus becomes increasingly difficult. This can be explained from the effect of the spin accumulation on the demagnetization of the Co layer. As previously reported [48], a negative spin accumulation counteracts the demagnetization of the localized spin system. As a result of the increasing number of Co layers, the (relative) amount of itinerant spin-down spins that are generated in the Co layer increases. Although at the same time, the amount of mobile (spin-up) spins that are generated in the Gd layer increases as well (as a result of the increased laser fluence), the relative influence of the Gd layer decreases with Co layer thickness. Consequently, switching becomes increasingly difficult.
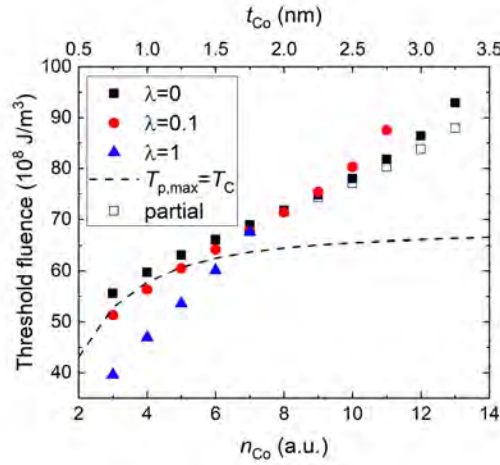

Figure 4.4: The threshold fluence for AOS of a Co/Gd bilayer for different values of λ as determined with the multilayer $s-d$ model as a function of the number of Co monolayers. The open black squares show the threshold for the numerically stable solution where only a part of the Co monolayers is switched ($\lambda = 0$). The dashed line indicates the fluence at which the maximum phonon temperature equals the bilayer's Curie temperature. For easy comparison with figure 2.8, the number of monolayers is converted into a Co layer thickness t_{Co} (top axis) assuming a 0.25 nm layer thickness [61].

Furthermore, for large layer thickness ($n_{Co} > 8$) an intermediate regime is observed (open black squares in figure 4.4), where a numerically stable solution with only a partially switched Co layer is found. In this regime, for example, only the first five monolayers ($i = 1 - 5$) switch, whereas the other Co monolayers return to their original state. These states are only observed in a fluence regime, where T_p reaches values far above T_C and physical relevance is questionable. Furthermore, for real samples such a state is expected to be unstable due to the large energy penalty as a result of the (ferromagnetic) exchange coupling.

By including direct angular momentum transfer between the localized spin systems ($\lambda = 0.1$), the threshold fluence at small Co thickness is decreased. Consequently, switching is observed for fluences where T_p remains smaller than T_C (figure 4.4). However, at larger layer thicknesses, the threshold fluence is found to be increasing at a faster rate than for $\lambda = 0$. At a Co thickness $n_{Co} > 11$, switching is no longer observed. For a larger value of λ ($\lambda = 1$ in figure 4.4) these effects are more prominent. For $n_{Co} < 7$ the phonon temperature stays below the Curie temperature, but for $n_{Co} > 7$ switching is no longer observed.

4.1.4 Spin current assisted AOS in the $s - d$ model

In this subsection and the remainder of this thesis a FM/NM/Co/Gd multilayer sample is modelled in the multilayer $s - d$ model (figure 4.5). The FM reference layer that is used in experiment is modelled as a fifteen monolayers thick Co layer. The NM spacer is implemented by setting the exchange coupling between the FM reference and free Co layer to zero. Again, the s system in the entire structure is assumed to equilibrate instantaneously. For these multilayer samples two threshold fluences are distinguished, one for P→AP and one for AP→P switching, i.e. $F_{\text{P}\rightarrow\text{AP}}$ and $F_{\text{AP}\rightarrow\text{P}}$, respectively. To goal is to investigate whether the experimentally observed difference between $F_{\text{P}\rightarrow\text{AP}}$ and $F_{\text{AP}\rightarrow\text{P}}$ can be explained from the $s - d$ model.
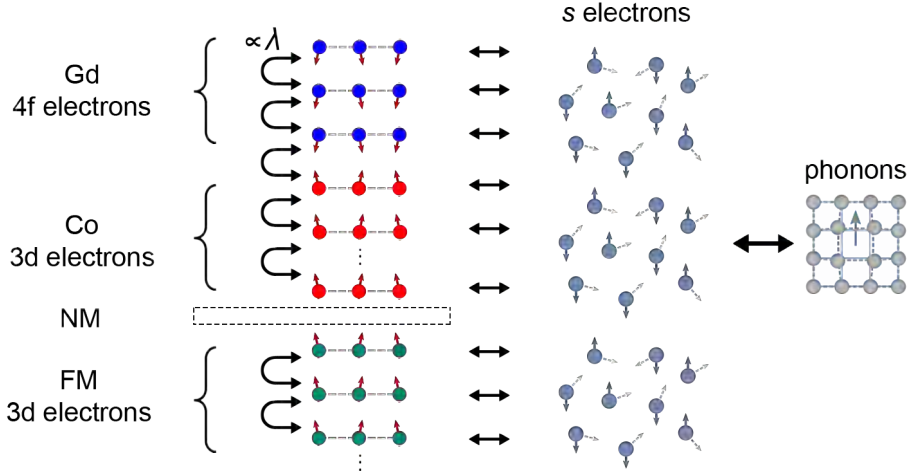
Figure 4.5: Schematic representation of the FM/Cu/Co/Gd multilayer in the $s - d$ model.

(a) initial state P

(b) initial state AP
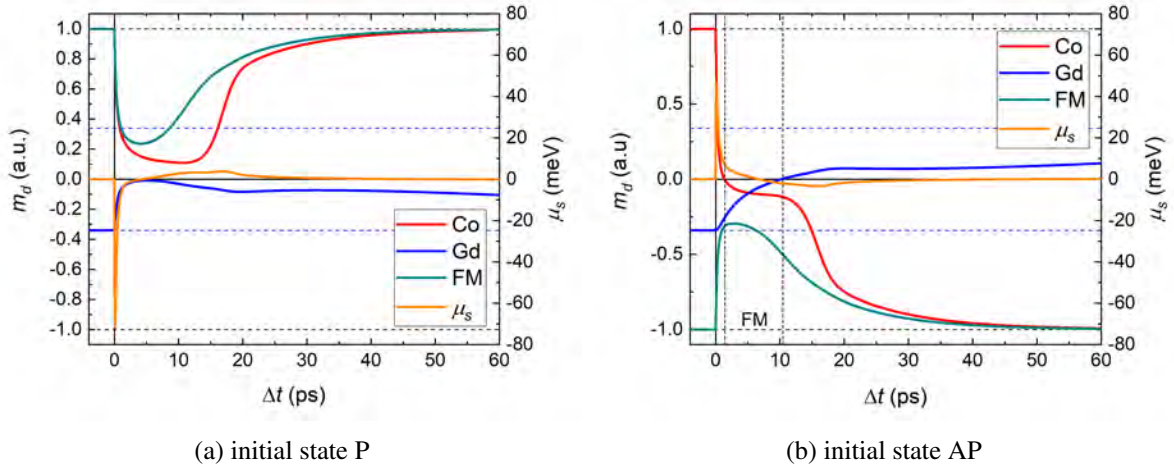
Figure 4.6: The laser induced dynamics for m_d and μ_s for a FM/CuCo/Gd multilayer ($n_{\text{Co}} = 5$) in the multilayer $s - d$ model ($\lambda = 0$) for laser fluence $P_0 = 66 \cdot 10^8 \ \frac{\text{J}}{\text{m}^3}$. Both a (a) P and (b) AP initial configuration are shown. The vertical dashed lines in (b) indicate the transient ferromagnetic-like (FM) state.

The magnetization dynamics are modelled at the same pump fluence as in figure 4.2. The result is plotted in figure 4.6. Since the reference layer is thicker than the Co layer, the spin accumulation in the modelled multilayer is dominated by the contribution from the demagnetization of the reference layer. When the multilayer is initially set in a P state (figure 4.6a), the negative spin accumulation generated in the reference layer results in a slower demagnetization rate in the Co layer. Consequently, the formation

of a transient ferromagnetic-like state in the Co/Gd bilayer and thus P→AP switching is hindered. For this pump fluence, the free layer returns to its initial state.

For an initial AP configuration (figure 4.6b) the spin accumulation generated in the reference layer is positive. Consequently, the demagnetization rate of the Co layer is enhanced (compared to a separate Co/Gd bilayer as well as a P configuration, figure 4.2a and figure 4.6a, respectively) and the formation of a transient ferromagnetic-like state and AOS is observed. Note that in AP configuration the spin accumulation generated in the Co layer has the opposite sign compared to the spin accumulation generated in the reference layer. Consequently, the maximum amount of spin accumulation in the multilayer is significantly smaller for an initial AP configuration than for an initial P configuration.

The Gd layer's behavior is the exact opposite of the behavior of the Co layer. In a P configuration, the demagnetization rate of the Gd is enhanced by the spin transport from the reference to the free layer. For the (initial) AP state, the demagnetization rate of the Gd layer is decreased. Again, the formation of a transient ferromagnetic-like state as a result of spin transport between the Gd and Co layer is thus hindered and assisted when the multilayer is initially in P and AP configuration, respectively.

In the remainder of this thesis, the multilayer $s - d$ model is compared to experimental results. In section 4.2.2 the behavior of the threshold fluence as function of Co layer thickness is discussed. The m_d dynamics of the Co layer for both AP→P and P→AP switching are compared to TR-MOKE measurements of the free layer's switching dynamics in section 4.3.3.

4.2 Static measurement of AOS

This section treats the static experiments on synthetic ferrimagnetic bilayers (Co/Gd) as well as magnetic multilayer samples (CoNi/Cu/Pt/Co/Gd, where as previously mentioned the [Co/Ni]$_4$/Co multilayer is referred to as if it were a single CoNi reference layer). In the static experiments, different spots on the samples are exposed to one or two separate pump pulses at varying pump fluence. The final state of the sample is recorded through a Kerr microscope. From the domain sizes of the all-optically switched domains, the threshold fluence is extracted as a function of Co layer thickness. These static switching experiments are also executed on a reversed stack (Co/Gd/Cu/Pt/CoNi), i.e. free layer/spacer/reference layer, in order to see whether the spin current arriving in the Gd layer instead of the Co layer results in a similar, deterministic switching behavior.

4.2.1 Static measurements on Co/Gd bilayers

The multilayer $s - d$ model is qualitatively compared to the experimentally determined threshold fluence for a Co/Gd bilayer. Measurements are performed on a Co(0 - 2)/Gd(3) wedged bilayer sample, where the thickness of the Co layer is wedged from 0 to 2 nm. At varying Co thickness, spots on the sample are exposed to a single pump pulse. The switched domains are imaged with a Kerr microscope. The size of a switched domain depends on the fluence of the laser pulse. The (planar) fluence F_{laser} is given by the pulse energy E_{laser} divided by the laser spot area. The AOS threshold fluence F_0, consequently, is defined as the threshold energy divided by the laser spot area. Assuming a slightly elliptical Gaussian laser pulse, with standard deviation along the short axis σ and (constant) ratio r between the long and short axis, the domain size of the switched domain is given by [19]

$$\text{domain size} = \pi r \sigma^2 \ln \left(\frac{E_{\text{laser}}}{\pi r \sigma^2 F_0} \right). \tag{4.1}$$

The switched domain size is determined for different laser energies (figure 4.7a). By fitting equation 4.1, the threshold fluence F_0 is extracted. In contrast to the predictions by the M3TM and the previously reported measurements on FM/Gd samples (figure 2.8), the slope in figure 4.7b is found to be increasing

(a)   (b)
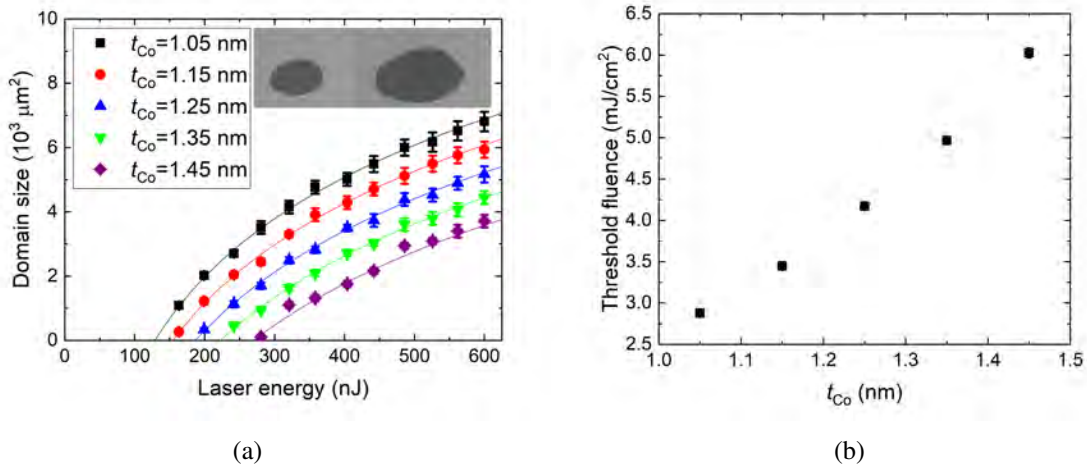
Figure 4.7: (a) Extracted domain size as function of laser energy for the wedged Co(0-2)/Gd(3) bilayer sample. The data is fitted with equation 4.1 in order to extract the threshold fluence. The inset shows two typical Kerr microscope images of switched domains. (b) Experimentally determined AOS threshold fluence for a Co(wedge)/Gd bilayer for different values of t_{Co}.

with layer thickness. As previously mentioned, an increasing amount of spin accumulation in the Co layer may give rise to an increasing slope. The increasing slope could be interpreted as an indication that itinerant electrons do play a (minor) role in AOS in Co/Gd bilayers. However, it should be noted that the measured thickness range spans approximately two monolayers, therefore no unambiguous conclusion can be drawn and further research is required. Furthermore, so far the effect of intermixing at the Co/Gd interface has not been taken into account. A recent theoretical study [62] indicates that intermixing reduces the threshold fluence. The experimentally observed behavior of the threshold fluence (figure 4.7b) can potentially be explained by assuming an equal amount of intermixing at the interface for each t_{Co}.

4.2.2 Spin current assisted all-optical switching

A wedged Co layer is used to measure the threshold fluence in CoNi/Cu/Pt/Co(t_{Co})/Gd samples as a function of the Co layer thickness t_{Co}. Static measurements are performed over the Co thickness range where clear PMA is observed. The sample is initially set in antiparallel configuration. By exposing the multilayer sample to two pump pulses that arrive one to two seconds apart, both the AP→P and P→AP switched domain sizes are determined (figure 4.8a). Again, from the size of the switched domains at different laser fluence, the threshold fluences are determined (figure 4.8b).

As expected, $F_{P \to AP}$ is found to be higher than $F_{AP \to P}$ (figure 4.8c). Furthermore, the fluence gap $\Delta F = F_{P \to AP} - F_{AP \to P}$ is found to be increasing with layer thickness. Although, it should again be noted that the measured thickness range is very small (approximately one Co monolayer). The main reason for this increasing gap size with Co thickness is the increasing switching threshold fluence F_0 for the Co/Gd bilayer (figure 4.7b). Since a higher fluence is required, the absorbed fluence in the reference layer is higher. Consequently, the reference layer is demagnetized more and a larger spin current is generated in the reference layer. More angular momentum is transferred from the reference to the free layer and the effect on the switching dynamics is larger, thus a larger fluence gap is observed.

The increasing F_0 is compensated for by normalizing the fluence gap. Normalization is done through division by the average threshold fluence $F_{avg} = \frac{1}{2}(F_{P \to AP} + F_{AP \to P})$. The normalized fluence gap ΔF_{norm} is shown in figure 4.8c as well (green, downward triangles). Although the change of ΔF_{norm} lies just within the measured uncertainty, ΔF_{norm} unexpectedly seems to be slightly increasing with

(a)

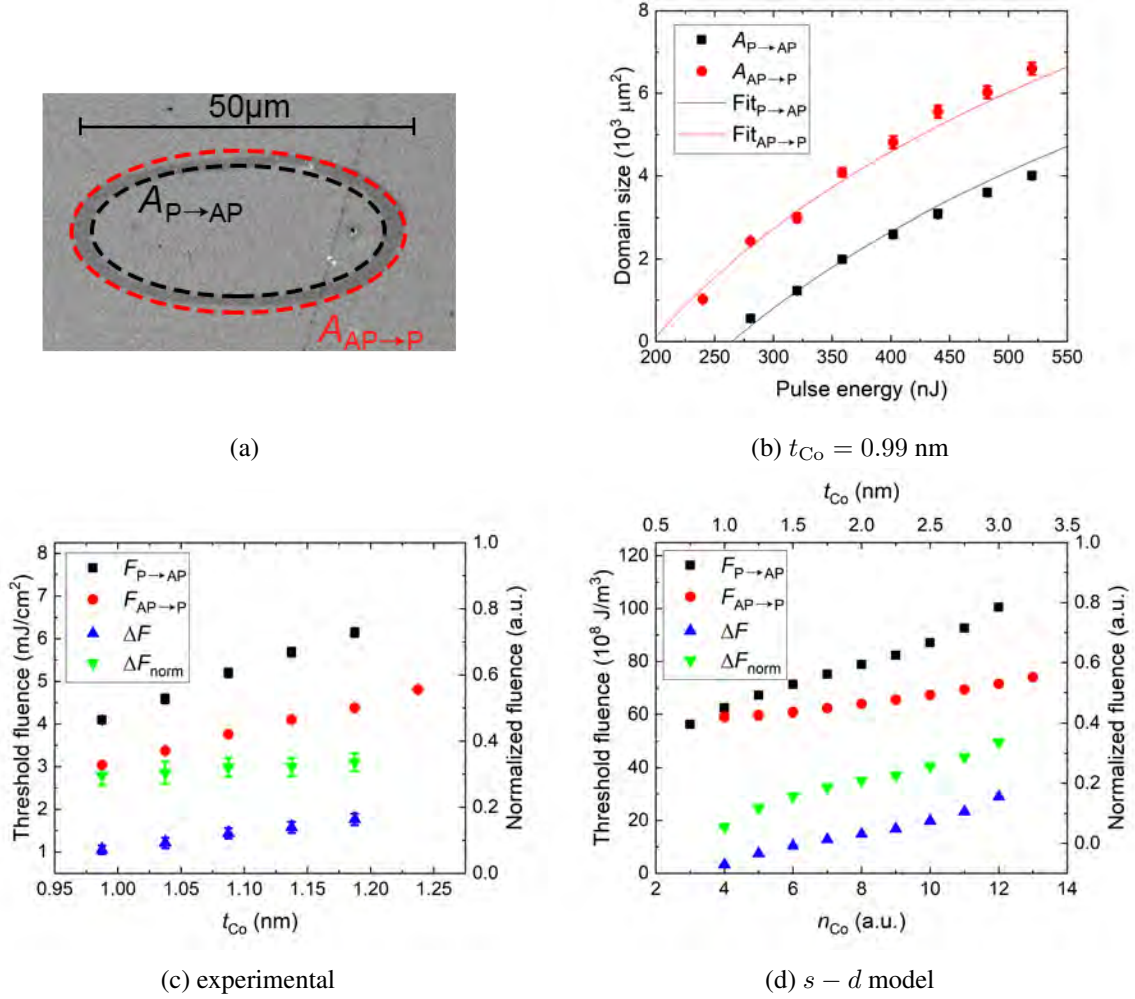

(b) $t_{Co} = 0.99$ nm

(c) experimental

(d) $s - d$ model

Figure 4.8: (a) Kerr microscopy image of a CoNi/Cu/Pt/Co/Gd sample after exposure to two pump pulses. The sample's initial state was AP. The P→AP and AP→P domain size ($A_{P→AP}$ and $A_{AP→P}$, respectively) are indicated. (b) Typical domain size as function of pump energy for the CoNi(4.6)/Cu(10)/Pt(0.5)/Co(0.5 - 1.5)/Gd(3) sample. The data is fitted with equation 4.1 in order to extract the threshold fluence. (c) Threshold fluences $F_{P→AP}$, $F_{AP→P}$, the fluence gap ΔF and normalized fluence gap ΔF_{norm} as experimentally determined as a function of t_{Co}. (d) $F_{P→AP}$, $F_{AP→P}$, ΔF and ΔF_{norm} for a FM/Cu/Co/Gd multilayer in the $s - d$ model with $\lambda = 0$. Note that the measured layer thickness in (c) spans a significantly smaller range than the t_{Co} range (top axis) in (d).

layer thickness. Intuitively, for an increasing Co layer thickness, the relative effect of the reference layer on the free layer is expected to decrease. Furthermore, from an absorption point of view, this result is equally unexpected. The (relative) absorption by the magnetic layers can be calculated with a transfer matrix method (TMM) [63, 64]. From these calculations, the amount of laser light absorbed in the free Co/Gd bilayer is expected to increase with Co layer thickness. Since more light has already been absorbed by the free layer before reaching the FM layer, the absorption in the reference layer is expected to decrease with t_{Co}. Consequently, the relative amount of angular momentum transferred from the reference to the free layer is expected to decrease with t_{Co}.

As mentioned in section 4.1.4, the multilayer structure is modelled in order to investigate whether the $s - d$ model can explain the experimentally observed fluence gap. Therefore, the threshold fluences $F_{P→AP}$ and $F_{AP→P}$ are extracted as function of n_{Co} (figure 4.8d). Similar to the experimental result, an increasing fluence gap with layer thickness is observed. The same normalization procedure is performed in order to exclude the effect of the increasing threshold fluence of the Co/Gd bilayer. For the $s - d$

simulations, the normalized gap ΔF_{norm} is clearly increasing with Co layer thickness. The order of magnitude of ΔF_{norm} is similar to the order of magnitude of ΔF_{norm} for the experimental results. It is concluded that the $s - d$ model is able to explain the experimentally observed ΔF.

4.2.3   Reversed multilayer stack

The final static switching experiments are performed on a sample with reversed reference layer and free layer positions relative to the incoming laser light (figure 4.9a). The Co layer that is part of the free layer, is deposited first. This ensures that the spin current traveling from the reference to the free layer arrives in the Gd instead of the Co. In principle, a similar difference in AOS threshold fluence for AP→P and P→AP switching as for the CoNi/Cu/Co/Gd samples is expected (see previously discussed Gd dynamics in the multilayer $s - d$ model, section 4.1.4). However, from previous measurements in the group, the proximity induced magnetization in the Gd is expected to correspond to approximately 0.45 nm of saturated Gd [19]. A large part of the 3 nm thick Gd layer is thus paramagnetic. Consequently, the effect of the paramagnetic Gd on the spin transport between the layers can be investigated with the reversed sample.

(a)   (b)
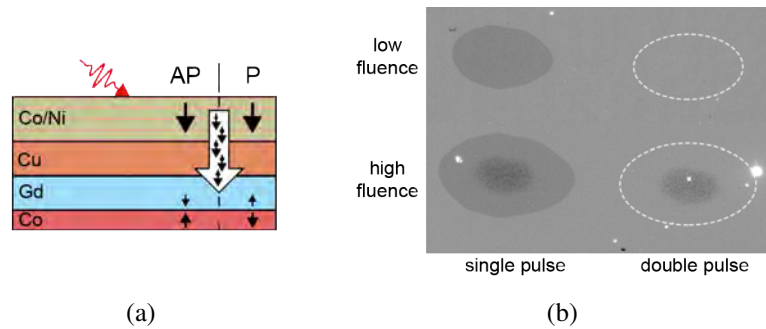
Figure 4.9: (a) Schematic representation of the reversed multilayer sample. (b) Kerr microscopy images for a Co(1)/Gd(3)/Ta(0.5)/Cu(3)/[Ni(0.6)/Co(0.2)]$_4$ magnetic multilayer sample after exposure to a single or double pulse for two different laser fluences, i.e. relatively low and high. Both pulses have a laser fluence above the switching threshold. A toggle switching mechanism is observed. For high laser fluence, a multidomain state is observed in the centre of the laser spot.

Again the initial state is set as AP. A static switching experiment is executed for both a single as well as two separate (time delay of 2 s) pump pulses. Instead of spin current assisted AOS, toggle switching is observed (figure 4.9b). At a fixed laser fluence, the P→AP domain size is equal to the AP→P domain size and the second pulse restores the sample's initial state. The angular momentum carried by the spin current is likely dissipated in the paramagnetic Gd before it reaches the magnetized part of the Gd and Co layers. Consequently, instead of spin current assisted AOS, conventional toggle AOS is observed.

4.3   Time-resolved measurement of magnetization dynamics

In the remainder of this chapter, the laser induced dynamics of FM/NM/Co/Gd multilayers are investigated through TR-MOKE. The goal is to determine how the multilayer's dynamics on a (sub) ps timescale are influenced by the laser induced spin transport between the reference and free layer. First, low fluence demagnetization dynamics are discussed. In the final subsection time- and depth-resolved MOKE measurements of the spin current assisted AOS dynamics are treated.

4.3.1   Short timescale magnetization dynamics

TR-MOKE measurements at low pump fluence are performed. The spin current between the free and reference layer is expected to be maximum during the ultrafast demagnetization of the CoNi reference layer. Consequently, at a short time delay, i.e. at a time delay $\Delta t \leq 2$ ps, the largest effect on the demagnetization dynamics is expected. A QWP (section 3.1.6) is inserted in the probe path in order to isolate the free layer's contribution to the Kerr signal. Based on the hysteresis loop (figures 4.10a), the angle of the QWP is set such that only the free layer contribution remains. This is confirmed by comparison with the hysteresis loop measured without a QWP, which contains contributions from both the reference and free layer (figure 4.11b).

The (anti)symmetrization (equation 3.11) that is used in order to get rid of the non-magnetic background, is performed with respect to the free layer's magnetization. The sign in the multilayer state, e.g. the '+' in P+ or AP+, indicates the reference layers magnetization direction instead of the free layers magnetization direction. Therefore, the voltages plotted in figure 4.10b are determined by

$$
\begin{aligned}
V_{\text{out,P}} &= \frac{V_{\text{out,P+}} - V_{\text{out,P-}}}{2}, \\
V_{\text{out,AP}} &= \frac{-V_{\text{out,AP+}} + V_{\text{out,AP-}}}{2}.
\end{aligned}
\tag{4.2}
$$

A large difference in the TR-measurement (figure 4.10b) between a P and AP configuration is observed. First of all, the sign of the coherent contribution to the signal at pump-probe overlap (section 3.1.7) is opposite for $V_{\text{out,P}}$ compared to $V_{\text{out,AP}}$, which indicates that the coherent contribution originates mainly in the CoNi reference layer, i.e. the layer with the largest magnetization. For a time delay up to 0.25 ps the signal is dominated by this coherent contribution. For larger time delays ($\Delta t > 0.25$), the two curves differ a lot from each other and the minimum signal is measured for two very different time delays (at approximately 0.3 to 0.6 ps). However, from the measurement it is unclear whether this difference results from the Co/Gd bilayer's demagnetization signal or a different signal, such as the coherent pump-probe overlap contribution. No unambiguous conclusions can be drawn.

(a)   (b)
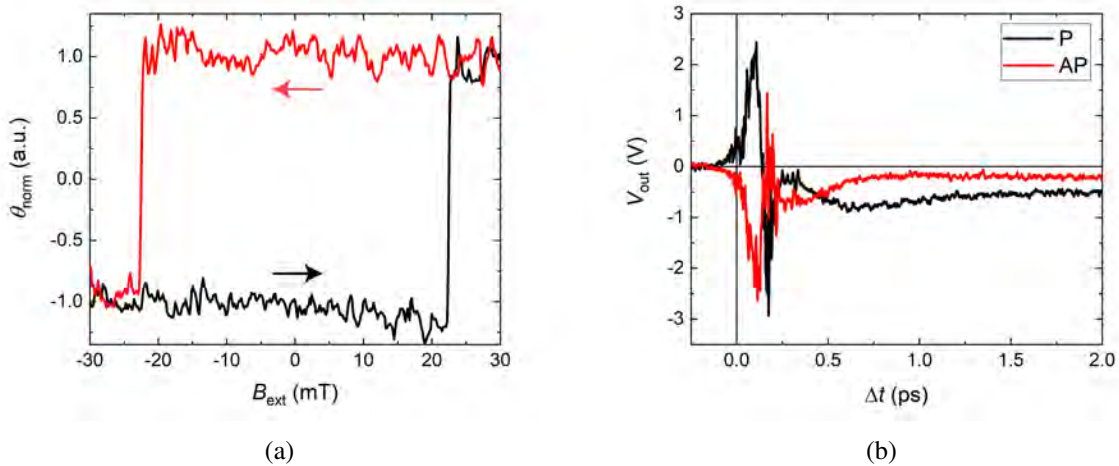
Figure 4.10: (a) Hysteresis of the free layer in a CoNi(4.6)/Cu(5)/Pt(0.5)/Co(1)/Gd(3) multilayer sample. A QWP has been used to isolate the free layer's contribution to the (normalized) Kerr signal. (b) Second lock-in output signal for a TR-MOKE measurement on the CoNi/Cu/Pt/Co/Gd sample in both P and AP configuration with a QWP at the same angle as in (a). The signal's offset at negative delay due to remanent heat has been subtracted.

The focus is shifted to the CoNi reference layer. By setting lock-in 1 to the first harmonic of the PEM frequency (instead of the second harmonic), the (TR-)MOKE signal is sensitive to the Kerr ellipticity ε (instead of Kerr rotation θ, see section 3.1.3). Even without a QWP, the complex Kerr rotation Φ of the free layer is such that only the reference layer is found to contribute to the signal measured through ε (figures 4.11a). Consequently, the reference layer's contribution can be isolated without the need for a QWP in the probe line. Since the only difference between the ε and θ measurements are the internal settings of the PEM and lock-in amplifier, the pump and probe path lengths are expected to be unaffected by the change from ε to θ signal (or vice versa).

(a) Kerr ellipticity (CoNi)   (b) Kerr rotation (full sample)

(c) Kerr ellipticity (CoNi)   (d) Kerr rotation (full sample)
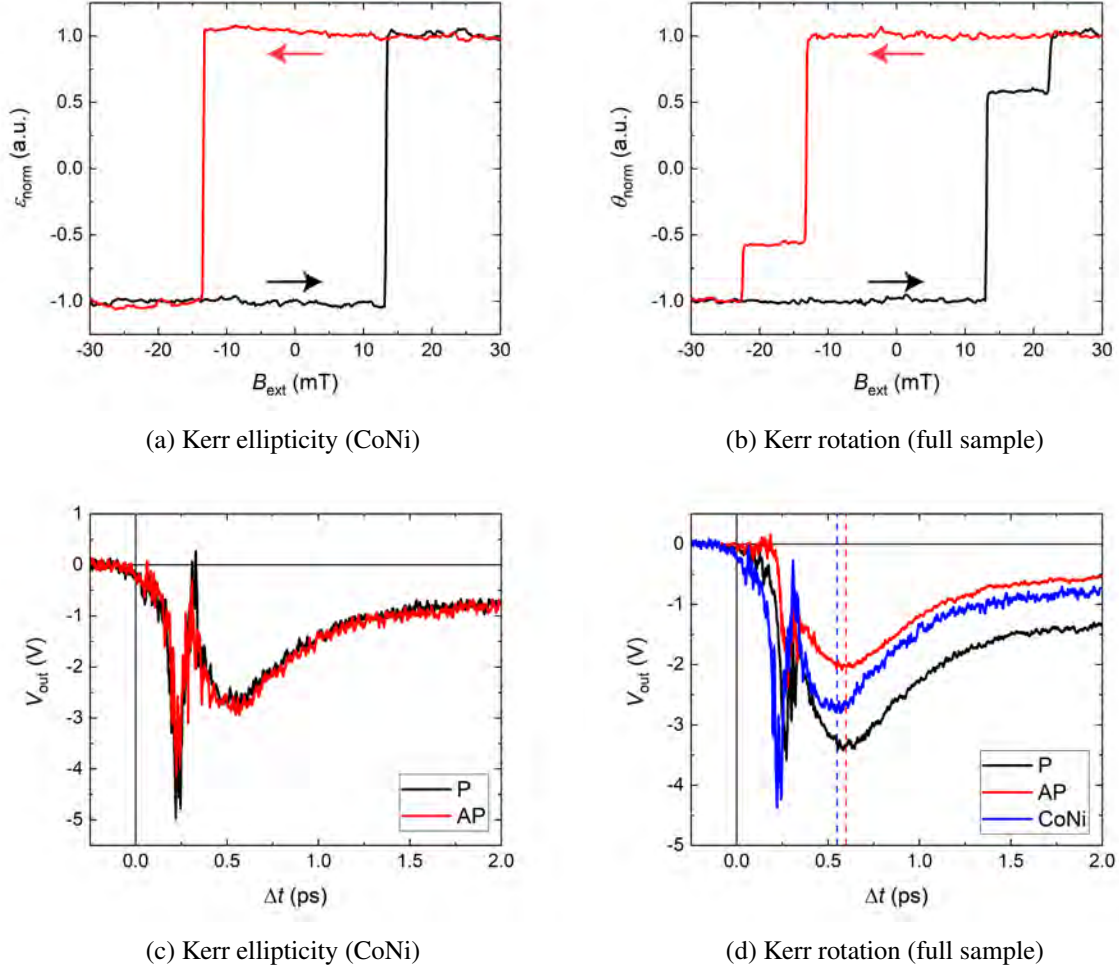
Figure 4.11: (a) & (b) Normalized Kerr signal for the CoNi/Cu/Pt/Co/Gd multilayer sample for a hysteresis as measured from (a) Kerr ellipticity ε and (b) Kerr rotation θ. Only the CoNi reference layer contributes to the signal in (a). (c) & (d) Second lock-in output signal for a TR-MOKE measurement on the CoNi/Cu/Pt/Co/Gd sample in both P and AP configuration as measured from (c) ε and (d) θ. The offset at negative delay due to remanent heat has been subtracted. Panel (d) also shows the average value of the CoNi reference layer signal in (c). The time delay at which the CoNi reference layer and full sample are at maximum demagnetization is indicated with the blue and red dashed line, respectively.

The TR-MOKE signal is measured for both ε and θ, i.e. the reference layer contribution and contributions from the full multilayer (figure 4.11c and 4.11d), respectively. Within the first two ps, the demagnetization dynamics in the reference layer (figure 4.11c) are found to be (approximately) the same for P and AP configuration. It is concluded that on a short timescale, itinerant electrons generated in the Co/Gd bilayer have little to no effect on the laser induced dynamics in the reference layer. This is attributed to the fact that the CoNi multilayer has a much larger magnetization than the Co/Gd bilayer.

Due to the different PEM and lock-in settings, the amplitude of the ε and θ signal can not easily be compared. However, as previously mentioned, the pump-probe overlap is expected to be the same for both measurements and the measurements can qualitatively be compared. The maximum demagnetization in the reference layer is found to occur at a different time delay than the delay at which the maximum signal occurs in the full sample's dynamics (figure 4.11d). This indicates that the free layer's dynamics are largely influenced by the spin current originating from the reference layer. However, it is not possible to extract more information regarding the spin transport between the layers from the measurements.

4.3.2 Magnetization dynamics on a longer timescale

The goal of the research presented in this thesis is to investigate the non-local spin transport between the reference and free layer. As previously mentioned, the effects of this non-local spin transport is expected to be maximum for a short time delay. However, on the short timescale, the demagnetization measurements provided little insight in the spin transport. When comparing the CoNi reference layer's demagnetization dynamics for a P with an AP configuration (figure 4.11c), hardly any difference in the dynamics is observed for a delay up to 2 ps. Surprisingly, on a longer timescale, the AP signal is different from the P signal (figure 4.12a). In order to investigate whether the observed difference in the TR-MOKE signals results from spin transport between the reference and free layer, a multilayer sample with a Pt spacer is fabricated. A Pt spacer is used, since Pt has a short spin-diffusion length ($\lambda_{Pt} \approx 1.4$ nm) [65, 66]. As a result of this short λ_{Pt}, the electrons traveling between the reference layer and free layer are no longer spin-polarized upon arrival in the other layer. Previous research has shown that the fluence gap between AP→P and P→AP switching disappears when the thickness of the Pt layer that is inserted between the Cu and Co layers is increased from 0.5 to approximately 2.5 nm [28]. By replacing the 5 nm thick Cu spacer for a 5 nm thick Pt spacer any effect of a spin current traveling between the layers is eliminated. The measured AP and P dynamics do not show a large difference (figure 4.12b). The observed difference between the AP and P dynamics for the sample with a Cu spacer is thus attributed to non-local spin transport.

(a) Cu spacer   (b) Pt spacer
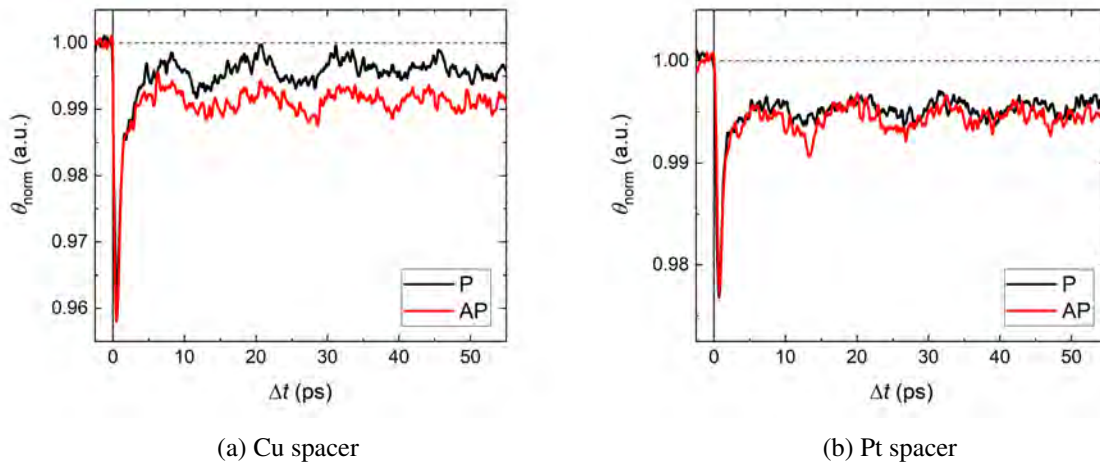
Figure 4.12: Normalized TR-MOKE signal for a (a) CoNi(4.6)/Cu(5)/Pt(0.5)/Co(1)/Gd(3) and (b) CoNi(4.6)/Pt(5)/Co(1)/Gd(3) multilayer sample measurement with QWP such that the reference layer signal is isolated. The oscillation that is observed in both (a) and (b) is attributed to an acoustic strain wave.

One might speculate that the origin of this non-local spin transport is a long lived spin accumulation generated by the Gd magnetization dynamics, similar to the Gd contribution to the spin accumulation that has experimentally been observed in ferrimagnetic alloys (figure 2.4). However, such a contribution is expected to decay within tens of ps. The difference between the P and AP signal, however, is observed

for a delay up to 400 ps and decays at a similar rate as the dissipation of the remanent heat from the multilayer to the substrate. Therefore, the spin transport most likely has a thermal origin. Since the heat in the sample is expected to dissipate through the substrate (which has a much larger thermal conductivity than air), a thermal gradient is expected to form along the z-direction of the sample [67]. The spin-dependent Seebeck effect is thus expected to contribute to the spin transport, although it is questionable whether this gives a significant contribution for more than 100 ps.

Furthermore, a coherent oscillating contribution to the Kerr signal is measured for both the Cu and Pt spacer (figures 4.12a and 4.12b, respectively). The oscillation has a frequency of approximately 0.5 THz. The signal is attributed to a laser-induced longitudinal acoustic strain wave traveling through the entire multilayer sample. Such an acoustic signal has previously been observed in similar samples [68]. Using the multilayers total thicknesses $t_{\text{tot}} \approx 26$ nm, a (longitudinal) sound velocity of approximately $4 \frac{\text{km}}{\text{s}}$ is derived, which is close to literary values for the used metals (3 - 5.8 $\frac{\text{km}}{\text{s}}$ [61]).

In conclusion, the time-resolved (low fluence) demagnetization measurements indicate that in the first two picoseconds itinerant electrons generated in the Co/Gd bilayer have little to no effect on the laser induced dynamics in the reference layer. Comparison of the CoNi demagnetization signal with the full sample's TR-MOKE signal indicates that the Co/Gd bilayer's dynamics are strongly influenced by laser induced spin transport. From an attempt to measure the free Co/Gd bilayer's dynamics directly, no unambiguous conclusions could be drawn. Furthermore, on a longer timescale a difference between the AP and P dynamics of the CoNi reference layer is observed. From comparison to a sample with a Pt spacer is concluded that the observed difference is most likely the result of (thermally induced) spin transport between the two layers.

4.3.3   Spin current assisted switching dynamics

In the final subsection of this chapter, TR-MOKE measurements of the switching dynamics for the Co/Gd bilayer in a CoNi(4.6)/Cu(5)/Pt(0.5)/Co(1)/Gd(3) multilayer sample are discussed. The pump fluence is set such that toggle switching is observed over the entire area covered by the probe pulse. Measurements are performed without the presence of an applied field. The sample is pumped at a fluence in the toggle regime, i.e. each pump pulse switches the free layer's magnetization. Since the TR-MOKE signal is measured by averaging over all probe pulses while the sample is continuously pumped (repetition rate of 100 kHz), the measured signal consists of the average contribution of an equal amount of P→AP and AP→P switches. Without any changes to the setup, the free layer's contribution to the time-resolved signal will thus average zero.

In order to measure the time-resolved switching dynamics, it is necessary to isolate the signal for only the even or odd pulses (appendix C). In this manner, a TR-MOKE signal for switching in one direction (either P→AP or AP→P) can be measured. To illustrate this, two hysteresis loops are shown in figure 4.13. The hysteresis loops are measured at a negative time delay ($\Delta t = -10$ ps). Both signals are normalized to the Kerr signal when the sample is in P configuration. Since only the odd or even pulses are measured, two different hysteresis loops are observed (figures 4.13a and 4.13b, respectively). The initial state of the sample was P. When measuring only the odd pulses at a negative delay (figures 4.13a), the sample is always probed after it has switched back to a P state (for example after the second pulse, just before the third pump pulse arrives). For the even pulses, the sample is probed when it is switched to an AP state, as is observed at zero applied field in figure 4.13b.

Furthermore, figure 4.13 shows why measurement without any applied field is required. At high field values in both hysteresis loops in figure 4.13 a P state is observed. The curved parts of the hysteresis loop show that field values above 50 mT are required in order to restore the free layer's magnetization into its initial direction before the next pump pulse arrives. However, the reference layer's coercivity field has a value of 20 mT. Consequently, when measuring with an applied field, the field always sets the sample in a P configuration and only P→AP switching can be observed.

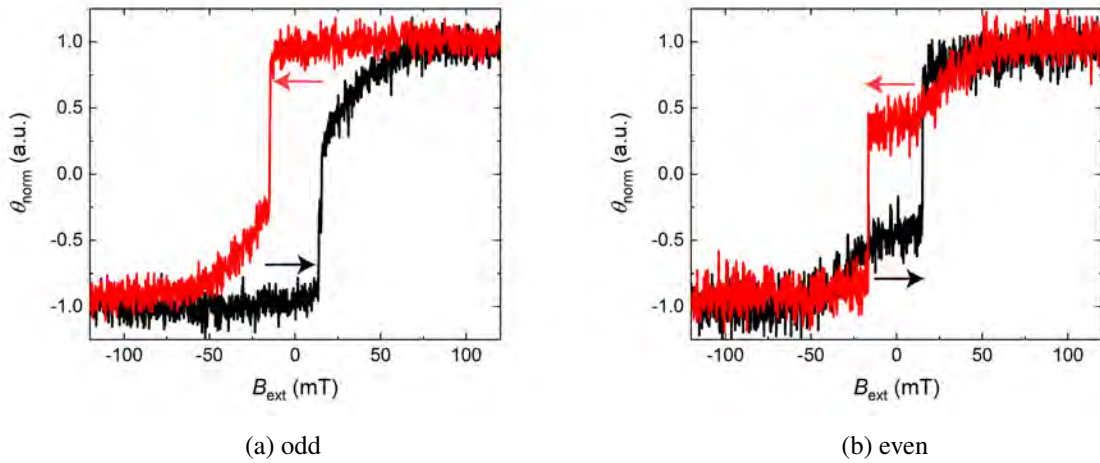(a) odd   (b) even

Figure 4.13: Hysteresis for a CoNi(4.6)/Cu(5)/Pt(0.5)/Co(1)/Gd(3) multilayer in the TR-MOKE setup were only the signal for only the (a) odd or (b) even pulses is measured. Measurements are performed at negative pump-probe delay. At zero field the sample is either in (a) P or (b) AP state. At high field, the sample is saturated in P configuration before the next pump pulse arrives. The steps in the hysteresis loops correspond to the switch of the CoNi reference layer.

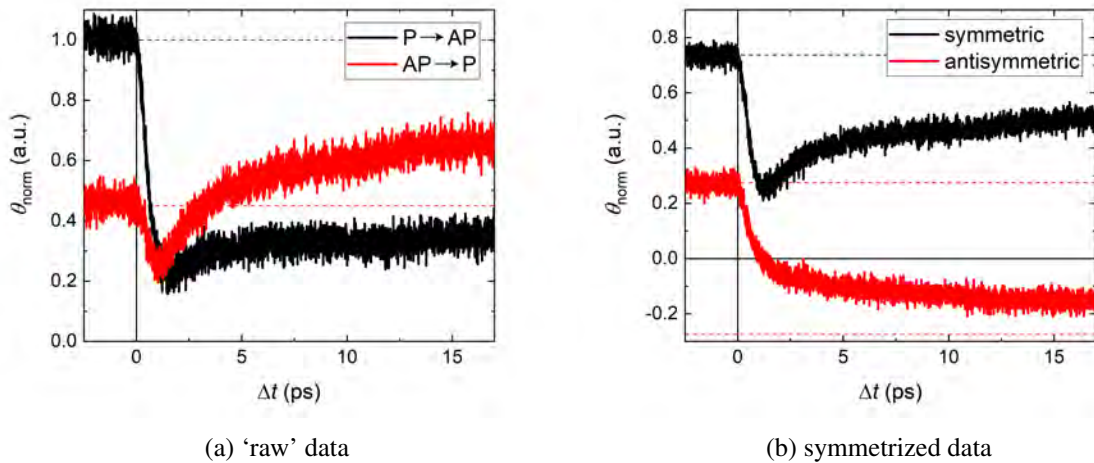(a) 'raw' data   (b) symmetrized data

Figure 4.14: (a) Normalized TR-MOKE measurement of the AOS dynamics in a CoNi/Cu/Pt/Co/Gd multilayer were only the signal for the even or odd pump pulses is measured. (b) Symmetric and antisymmetric part of the 'raw' TR-MOKE data in (a). The symmetric part shows the average reference layer contribution, whereas the antisymmetric part is dominated by the free layer.

First, a TR-MOKE measurement without a QWP is performed (figure 4.14). Again the MOKE signal is normalized to the P state. The signals consist of two distinct contributions, i.e. the demagnetization of the reference layer and the switch of the free layer. By isolating the symmetric and antisymmetric part of the signals, an average contribution by these two layers (reference and free, respectively) can be distinguished (figure 4.14b). The magnetization dynamics of the FM reference layer clearly resemble the previously observed dynamics for laser induced demagnetization in a TM (figure 2.1). The average free layer dynamics closely resemble Co/Gd switching dynamics as previously measured within the group (figure 4.15a) [69]. However, due to the symmetrization, any information regarding the difference between P→AP and AP→P switching (in other words, regarding the spin transport between the reference and free layer) has been lost.

(a) Co/Gd

(b) with QWP
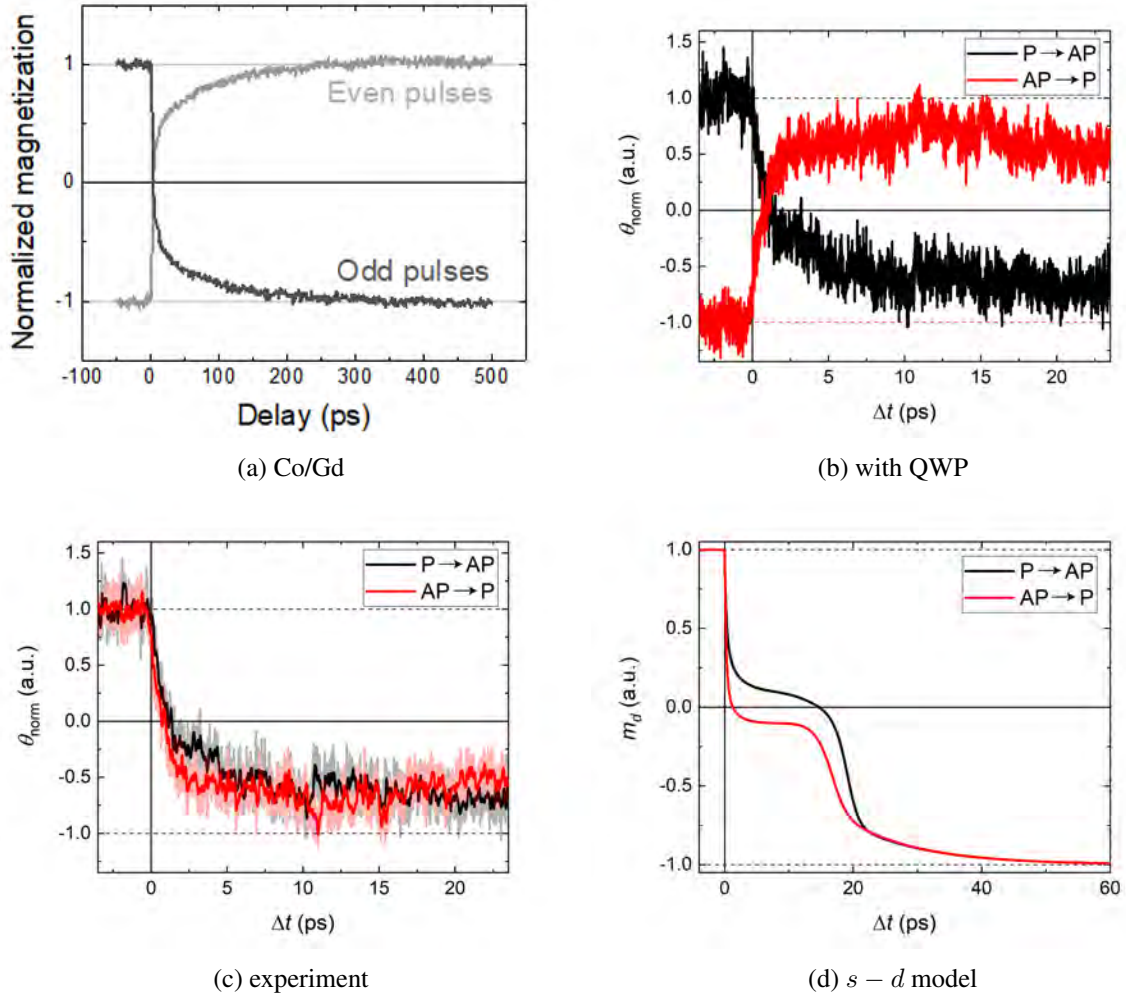
(c) experiment

(d) $s-d$ model

Figure 4.15: (a) Normalized TR-MOKE measurement of the AOS dynamics in a Co/Gd bilayer. From [69]. (b) Normalized TR-MOKE measurement of the AOS dynamics in a CoNi/Cu/Pt/Co/Gd multilayer as measured with a QWP. Again only the signal from the even or odd pump pulses is measured. The angle of the QWP is such that only the free layer's contribution to the Kerr signal is measured. (c) Rolling mean of the TR-MOKE measurement of the AOS dynamics in (b). Both the P→AP and AP→P curves have been normalized to the signal at a negative time delay. The window size that is used to calculate the rolling mean equals 0.1 ps. (d) Multilayer $s-d$ simulation of the Co magnetization dynamics for both P→AP and AP→P switching in the modelled FM/Cu/Co/Gd multilayer.

By inserting a QWP in the path of the probe beam, the free layer's contribution to the Kerr signal is isolated (figure 4.15b). The measured switching dynamics closely resemble the TR-MOKE measurements on a Co/Gd bilayer (figure 4.15a). The measurements are relatively noisy. In order to illustrate the difference between the AP→P and P→AP signal, the rolling mean of both signals is calculated (figure 4.15c). Some clear differences between the AP→P and P→AP measurement can be distinguished. In agreement with the previously discussed demagnetization measurements, already within the first ps the AP→P and P→AP dynamics of the free layer are different. Similar to the FM/NM/FM experiment (figure 2.2), a faster demagnetization of the free layer is found for AP→P switching. Consequently the magnetization crosses zero at a shorter time delay for AP→P than for P→AP switching.

In section 4.2.2 the $s-d$ model was compared to the experimental observation of the fluence gap ΔF as function of Co layer thickness. Here, the free layers switching dynamics in the toggle regime are modelled in the multilayer $s-d$ model and compared to the TR-MOKE measurement. The laser in the

TR-MOKE setup has a wavelength of 700 nm and is mostly sensitive to the Co magnetization (section 3.1.4). The experimental data are thus compared to the Co m_d dynamics (figure 4.15d). Similar to the experimental signal, within the first ps a clear difference between the AP→P and P→AP dynamics is observed. Again, the AP→P demagnetization rate is found to be larger than the P→AP rate. Furthermore, both the measurements and $s - d$ model indicate not only a difference in dynamics in the first ps, but a clear distinction between the AP→P and P→AP curve for several ps (up to approximately 8 ps for the experimental signal).

In conclusion, in this subsection the free layer's switching dynamics as measured through depth- and time-resolved MOKE are discussed. The measured dynamics agree well with expectations based on previous experiments as well as the $s - d$ model. In the next and final chapter of this thesis, all research findings are summarized and some recommendations for future research are given.

5   Conclusions and outlook

Recent research has shown that by combining non-local spin transport with all-optical switching, data can deterministically be written in magnetic domains. This deterministic AOS writing mechanism is very promising for application in a new generation of magnetic memory devices. AOS based devices show high potential for integration with future photonic integrated circuits. In terms of writing speed and energy efficiency an AOS based device has the potential to outperform devices with an electrical writing mechanisms, since no signal conversion from photonic to electric or vice versa is required. In order optimize spin current assisted AOS in spintronic devices, a good understanding of the nature and behavior of the laser induced phenomena is required. However, the microscopic origin of both laser induced spin currents and all-optical switching is still under debate. In this thesis, the influence of non-local spin transport and itinerant electrons on electrons on AOS is investigated. In this final chapter the most important research findings are summarized. Furthermore, some recommendations for future research are given.

5.1   Applicability of the multilayer $s-d$ model

The applicability of the multilayer $s-d$ model on AOS in synthetic ferrimagnetic (Co/Gd) bilayers has been investigated. Laser induced switching on a ps timescale as a result of the $s-d$ exchange interaction is reproduced. However, AOS is only observed in a fluence regime where the phonon temperature is raised above the Curie temperature. At these high fluences, in a real sample a multidomain state is expected to form. By adding a direct angular momentum exchange channel between adjacent monolayers, the threshold fluence can be decreased. The experimental observation of switching over a large range of TM layer thicknesses [46], however, is not reproduced.

The accuracy of the $s-d$ model can potentially be improved. The implementation of direct angular momentum exchange by adopting the exchange scattering term from the M3TM might not be fully correct. It is possible that a correct derivation of this term would enable the model to reproduce the previously mentioned experimental observation of AOS for a large range of TM layer thicknesses. Furthermore, recent research [62] suggests that intermixing at the TM/RE interface reduces the switching threshold fluence. Thus far, the effects of intermixing have not been taken into account in the multilayer $s-d$ model.

Even though the $s-d$ exchange interaction alone is unable to fully explain AOS in synthetic ferrimagnetic bilayers, the multilayer $s-d$ model provides a useful tool for simulating laser induced phenomena in multilayer structures that are attributed to (non-local) spin transport. The multilayer $s-d$ model reproduces the experimentally observed difference in threshold fluence between P→AP and AP→P switching.

5.2   Static measurement of the AOS threshold fluence

From static switching experiments on synthetic ferrimagnetic bilayers (Co/Gd) as well as multilayer samples for spin current assisted AOS ([Co/Ni]$_4$/Co/Cu/Pt/Co/Gd) the threshold fluence as a function of Co thickness has been determined. Although the measured Co thickness range is small, for both samples the threshold fluence is found to increase with Co thickness.

The measurements on the Co/Gd bilayer indicate that switching becomes increasingly difficult with Co layer thickness. The same effect is observed in the multilayer $s-d$ model (for large layer thicknesses). Itinerant electrons can thus potentially explain the experimental observations. However, as intermixing is expected to reduces the AOS threshold fluence, an equal amount of intermixing at every Co thickness provides an alternative explanation for the experimental result.

For the [Co/Ni]$_4$/Co/Cu/Pt/Co/Gd multilayer, the expected spin current assisted AOS is observed over the entire measured Co thickness range. The fluence gap between P→AP and AP→P is found to be increasing with Co thickness. The increase in fluence gap can be partly explained by the increase in threshold fluence for switching the Co/Gd bilayer with increasing Co layer thickness. The fluence gaps are normalized in order to compensate for this effect. Although within the experimental uncertainty, the normalized fluence gap seems to be slightly increasing with Co layer thickness. A decreasing trend was initially expected.

The threshold fluences as function of Co layer thickness are extracted from the multilayer $s - d$ model. The simulations reproduce the increasing fluence gap with Co thickness as well as an increasing normalized fluence gap. The normalized fluence gap in the multilayer $s - d$ model is found to be in the same order of magnitude as the experimentally observed normalized gap. It is concluded that the $s - d$ model is able to explain an increasing (normalized) fluence gap, however the model does not take the effects of a reduced absorption in the reference layer as result of the increased Co thickness in the free layer into account.

As the performed experiments only span a small Co thickness range and the observed increase of the normalized gap lies within the experimental uncertainty, further research is suggested. In order to verify whether the normalized fluence gap increases with layer thickness static experiments over a larger thickness range are suggested. In order to ensure PMA over a larger thickness range, a [Co/Ni] multilayer could be used instead fo the Co in the free layer, similar to the FM/Gd bilayer in reference [46].

5.3   Influence of non-local spin transport on ultrafast demagnetization

Through TR-MOKE measurements the ultrafast dynamics of [Co/Ni]$_4$/Co/Cu/Pt/Co/Gd multilayer samples have been investigated. Both (low fluence) demagnetization as well as toggle switching dynamics have been measured.

From the low fluence measurements it is concluded that the [Co/Ni]$_4$/Co reference layer's ultrafast magnetization dynamics are barely influenced by itinerant electrons originating from the free Co/Gd layer. The reference layer's dynamics are qualitatively compared to the TR-MOKE signal with contributions from both the free and reference layer. It is concluded that the free layer's demagnetization even at low fluence is influenced significantly by the spin transported from the reference layer. Measurements of the free layer's ultrafast dynamics unfortunately yield no unambiguous results.

On a longer timescale ($\Delta t > 2$ ps), a clear difference between the reference layer's TR-MOKE signal in P and AP configuration is observed. The measurements are compared with TR-MOKE demagnetization measurements on a sample where the Cu spacer has been replaced by a Pt spacer layer. The Pt spacer dissipates the angular momentum that is transported between the reference and the free layer by itinerant electrons. For the sample with a Pt spacer, barely any difference in P and AP signal is observed. Therefore, the observed difference in TR-MOKE signal between P and AP configuration for the sample with a Cu spacer is attributed to angular momentum transport between the reference and the free layer. Although the exact origin of this spin current is unknown, it is most likely thermal in nature. Both the Gd magnetization dynamics as well as the spin-dependent Seebeck effect are expected to contribute to the spin current, however it is questionable whether these effects give rise to a significant contribution for more than 100 ps.

In order to gain more insight in the nature of this spin currents, more measurements are suggested. Similar to previous research [44], a time-resolved measurement of the spin accumulation generated by a Co/Gd bilayer in a NM/Co/Gd sample could provide more insight in, among others, the Gd and spin-dependent Seebeck effect contributions to the spin current.

5.4   Influence of non-local spin transport on AOS dynamics

The magnetization dynamics of both AP→P and P→AP AOS in a [Co/Ni]$_4$/Co/Cu/Pt/Co/Gd multilayer sample have been measured with the TR-MOKE setup. A clear difference between the AP→P and P→AP signal is observed. The Co/Gd free layer exhibits a faster demagnetization rate for AP→P switching and a smaller (more negative) Co magnetization is observed for a pump-probe delay up to approximately 8 ps for AP→P compared to P→AP switching. Similar dynamics are observed for the multilayer $s-d$ model.

Just a single TR-MOKE experiment on the switching dynamics has been performed. In order to gain more (quantitative) insight in the AP→P and P→AP switching dynamics, it is suggested to perform the time-resolved measurements for varying threshold fluence gap sizes, e.g. by varying the Co layer thickness in the free layer or the Ni layer thickness in the reference layer [28].

5.5   Future research

Some very preliminary static switching experiments have been performed on a reversed sample stack, i.e. where the order of the reference and free layer has been reversed. In the reversed Co/Gd/Ta/Cu/[Ni/Co]$_4$ stack, the spin current traveling from the reference to the free layer arrives in the Gd instead of the Co part of the Co/Gd bilayer. No evidence of a fluence gap between AP→P and P→AP switching has been found. This is attributed to diffusion of the angular momentum carried by the itinerant spins in the paramagnetic part of the Gd layer. Measurements have only been performed for one Gd layer thickness. To determine whether the arrival of the spin current in the magnetized part of the Gd influences the laser induced switch of the free layer differently, measurements for varying Gd thickness are suggested. Additionally these measurements could offer more insight on the spin-transfer or spin-diffusion length of the Gd.
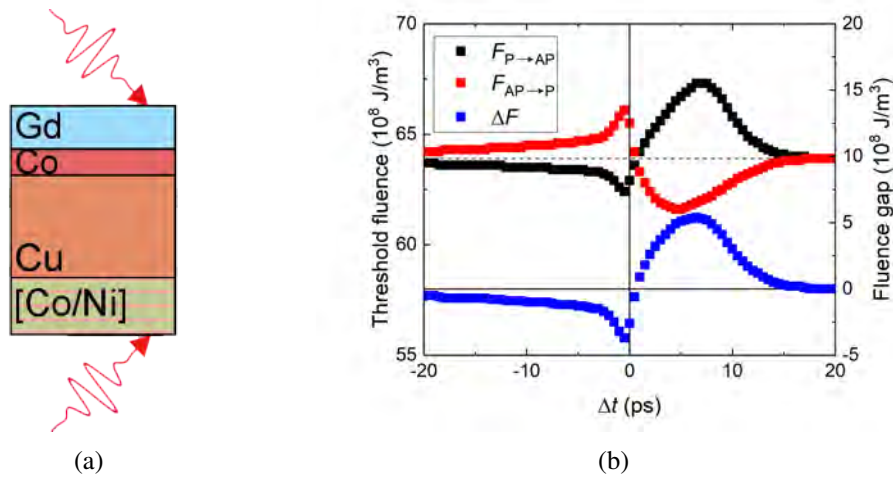
Figure 5.1: (a) Schematic representation of the proposed double pump measurement on a FM/NM/T-M/RE multilayer sample. (b) The threshold fluence and fluence gap as function of the time delay between the free layer and reference layer pump pulses for a FM/NM/Co/Gd sample in the $s-d$ multilayer model. Both the FM reference and Co part of the free layer are modelled as 5 monolayers of Co. The reference layer is pumped at a constant laser fluence of $30 \cdot 10^8 \; \frac{\text{J}}{\text{m}^3}$.

Furthermore, one interesting observation in figure 4.8d is that in the $s-d$ model at very small Co layer thickness ($n_{\text{Co}} = 3$) not AP→P, but P→AP switching is favored. For this particular n_{Co} in fact, AP→P switching is no longer observed in the model. This is, among others, attributed to the fact that

the spin accumulation has a $\frac{\mathrm{d}m}{\mathrm{d}t}$ dependence. The remagnetization of the reference layer generates a sufficient amount of spin accumulation to counteract the switching of the Co layer and to restore the system to its initial state. This indicates that by varying the exact moment at which the spin current arrives in the free layer, the fluence gap can be tuned. This can potentially be achieved by increasing the spacer thickness and exciting the reference and free layer with separate pulses (figure 5.1a). The amount demagnetization of the free or reference layers due to the pump pulse that is used to pump the other layer, should be minimized. Simultaneously, angular momentum transport between the reference and free layer should still occur. Since the spin-diffusion length of Cu is approximately 400 nm [70, 71] and the optical penetration depth in Cu for a laser wavelength of 700 nm approximately 13 nm [72], it is expected that a suitable Cu spacer thickness can be found.

Some preliminary modelling on such a system is performed (figure 5.1b). The system is modelled with two separate electron and two separate phonon temperatures, describing the free layer's and the reference layer's thermal electron and phonon systems. No energy is exchanged between the free layer and the reference layer. The spin accumulation is still equilibrated over the entire multilayer structure. In other words, mobile s spin system transport angular momentum between monolayers, both within the reference and free layer and between the reference and free layer. When the reference layer is pumped before the free layer is pumped, the reference layer already remagnetizes when the free layer is switched. The spin current that is generated during remagnetization has the opposite polarization of the spin current that is generated during demagnetization. Consequently, instead of assisting AP→P switching, this spin current hinders AP→P switching. On the other hand, P→AP switching is assisted by the spin current that is generated during remagnetization. The toy model thus predicts a tunable fluence gap (figure 5.1b), depending on the time delay between the pump pulses.

By performing the suggested experiment, more information on the microscopic origin of laser induced spin transport can be obtained. A different outcome is expected for spin current generation proportional to the time derivative of the magnetization, as assumed in e.g. the $s - d$ model, and different spin accumulation dynamics, as for example is expected from the theory of superdiffusive spin transport. In order to apply and optimize spin current assisted AOS in magnetic memory devices, a good understanding of the microscopic origin of laser induced non-local spin transport is required. The work presented in this thesis indicates that the experimentally observed laser induced phenomena can be explained assuming spin current generation proportional to the time derivative of the magnetization.

Bibliography

[1] R. Bläsing, A. A. Khan, P. C. Filippou, C. Garg, F. Hameed, J. Castrillon, and S. S. Parkin, "Magnetic racetrack memory: From physics to the cusp of applications within a decade," *Proceedings of the IEEE*, 2020.

[2] S. Parkin and S.-H. Yang, "Memory on the racetrack," *Nature nanotechnology*, vol. 10, no. 3, pp. 195–198, 2015.

[3] R. E. Fontana Jr and G. M. Decad, "Moore's law realities for recording systems and memory storage components: Hdd, tape, nand, and optical," *AIP Advances*, vol. 8, no. 5, p. 056506, 2018.

[4] C. M. Compagnoni, A. Goda, A. S. Spinelli, P. Feeley, A. L. Lacaita, and A. Visconti, "Reviewing the evolution of the nand flash technology," *Proceedings of the IEEE*, vol. 105, no. 9, pp. 1609–1633, 2017.

[5] D. Mamaluy and X. Gao, "The fundamental downscaling limit of field effect transistors," *Applied Physics Letters*, vol. 106, no. 19, p. 193503, 2015.

[6] A. D. Kent and D. C. Worledge, "A new spin on magnetic memories," *Nature nanotechnology*, vol. 10, no. 3, pp. 187–191, 2015.

[7] S. S. Parkin, M. Hayashi, and L. Thomas, "Magnetic domain-wall racetrack memory," *Science*, vol. 320, no. 5873, pp. 190–194, 2008.

[8] M. L. Lalieu, R. Lavrijsen, and B. Koopmans, "Integrating all-optical switching with spintronics," *Nature communications*, vol. 10, no. 1, pp. 1–6, 2019.

[9] L. Wang, H. Cheng, P. Li, Y. Liu, Y. Hees, R. Lavrijsen, X. Lin, K. Cao, B. Koopmans, and W. Zhao, "Picosecond switching of optomagnetic tunnel junctions," *arXiv*, Nov. 2020. https://arxiv.org/abs/2011.03612.

[10] J. M. D. Coey, *Magnetism and Magnetic Materials*. Cambridge University Press, 2010.

[11] Z. Diao, Z. Li, S. Wang, Y. Ding, A. Panchula, E. Chen, L.-C. Wang, and Y. Huai, "Spin-transfer torque switching in magnetic tunnel junctions and spin-transfer torque random access memory," *Journal of Physics: Condensed Matter*, vol. 19, no. 16, p. 165209, 2007.

[12] W. Zhu, H. Li, Y. Chen, and X. Wang, "Current switching in mgo-based magnetic tunneling junctions," *IEEE transactions on magnetics*, vol. 47, no. 1, pp. 156–160, 2010.

[13] A. Manchon, J. Železný, I. M. Miron, T. Jungwirth, J. Sinova, A. Thiaville, K. Garello, and P. Gambardella, "Current-induced spin-orbit torques in ferromagnetic and antiferromagnetic systems," *Reviews of Modern Physics*, vol. 91, no. 3, p. 035004, 2019.

[14] D. C. Ralph and M. D. Stiles, "Spin transfer torques," *Journal of Magnetism and Magnetic Materials*, vol. 320, no. 7, pp. 1190–1216, 2008.

[15] M. Cubukcu, O. Boulle, N. Mikuszeit, C. Hamelin, T. Brächer, N. Lamard, M.-C. Cyrille, L. Buda-Prejbeanu, K. Garello, I. M. Miron, *et al.*, "Ultra-fast perpendicular spin–orbit torque mram," *IEEE Transactions on Magnetics*, vol. 54, no. 4, pp. 1–4, 2018.

[16] E. Beaurepaire, J.-C. Merle, A. Daunois, and J.-Y. Bigot, "Ultrafast spin dynamics in ferromagnetic nickel," *Physical review letters*, vol. 76, no. 22, p. 4250, 1996.

[17] C. Stanciu, F. Hansteen, A. Kimel, A. Kirilyuk, A. Tsukamoto, A. Itoh, and T. Rasing, "All-optical magnetic recording with circularly polarized light," *Physical review letters*, vol. 99, no. 4, p. 047601, 2007.

[18] A. Khorsand, M. Savoini, A. Kirilyuk, A. Kimel, A. Tsukamoto, A. Itoh, and T. Rasing, "Role of magnetic circular dichroism in all-optical magnetic recording," *Physical review letters*, vol. 108, no. 12, p. 127205, 2012.

[19] M. Lalieu, M. Peeters, S. Haenen, R. Lavrijsen, and B. Koopmans, "Deterministic all-optical switching of synthetic ferrimagnets using single femtosecond laser pulses," *Physical review B*, vol. 96, no. 22, p. 220411, 2017.

[20] I. Radu, K. Vahaplar, C. Stamm, T. Kachel, N. Pontius, H. Dürr, T. Ostler, J. Barker, R. Evans, R. Chantrell, *et al.*, "Transient ferromagnetic-like state mediating ultrafast reversal of antiferromagnetically coupled spins," *Nature*, vol. 472, no. 7342, pp. 205–208, 2011.

[21] T. Ostler, J. Barker, R. Evans, R. Chantrell, U. Atxitia, O. Chubykalo-Fesenko, S. El Moussaoui, L. Le Guyader, E. Mengotti, L. Heyderman, *et al.*, "Ultrafast heating as a sufficient stimulus for magnetization reversal in a ferrimagnet," *Nature communications*, vol. 3, no. 1, pp. 1–6, 2012.

[22] A. V. Kimel and M. Li, "Writing magnetic memory with ultrashort light pulses," *Nature Reviews Materials*, vol. 4, no. 3, pp. 189–200, 2019.

[23] T. H. Pham, J. Vogel, J. Sampaio, M. Vaňatka, J.-C. Rojas-Sánchez, M. Bonfim, D. Chaves, F. Choueikani, P. Ohresser, E. Otero, *et al.*, "Very large domain wall velocities in pt/co/gdox and pt/co/gd trilayers with dzyaloshinskii-moriya interaction," *EPL (Europhysics Letters)*, vol. 113, no. 6, p. 67001, 2016.

[24] F. A. Kish, D. Welch, R. Nagarajan, J. L. Pleumeekers, V. Lal, M. Ziari, A. Nilsson, M. Kato, S. Murthy, P. Evans, *et al.*, "Current status of large-scale inp photonic integrated circuits," *IEEE Journal of Selected Topics in Quantum Electronics*, vol. 17, no. 6, pp. 1470–1489, 2011.

[25] G. Malinowski, F. Dalla Longa, J. Rietjens, P. Paluskar, R. Huijink, H. Swagten, and B. Koopmans, "Control of speed and efficiency of ultrafast demagnetization by direct transfer of spin angular momentum," *Nature Physics*, vol. 4, no. 11, pp. 855–858, 2008.

[26] G.-M. Choi, B.-C. Min, K.-J. Lee, and D. G. Cahill, "Spin current generated by thermally driven ultrafast demagnetization," *Nature communications*, vol. 5, no. 1, pp. 1–8, 2014.

[27] S. Iihama, Y. Xu, M. Deb, G. Malinowski, M. Hehn, J. Gorchon, E. E. Fullerton, and S. Mangin, "Single-shot multi-level all-optical magnetization switching mediated by spin transport," *Advanced Materials*, vol. 30, no. 51, p. 1804004, 2018.

[28] Y. L. van Hees, P. van de Meugheuvel, B. Koopmans, and R. Lavrijsen, "Deterministic all-optical magnetization writing facilitated by non-local transfer of spin angular momentum," *Nature Communications*, vol. 11, 2020.

[29] Q. Remy, J. Igarashi, S. Iihama, G. Malinowski, M. Hehn, J. Gorchon, J. Hohlfeld, S. Fukami, H. Ohno, and S. Mangin, "Energy efficient control of ultrafast spin current to induce single femtosecond pulse switching of a ferromagnet," *Advanced Science*, vol. 7, no. 23, p. 2001996, 2020.

[30] B. Koopmans, G. Malinowski, F. Dalla Longa, D. Steiauf, M. Fähnle, T. Roth, M. Cinchetti, and M. Aeschlimann, "Explaining the paradoxical diversity of ultrafast laser-induced demagnetization," *Nature materials*, vol. 9, no. 3, pp. 259–265, 2010.

[31] Ł. Cywiński and L. Sham, "Ultrafast demagnetization in the s p- d model: A theoretical study," *Physical Review B*, vol. 76, no. 4, p. 045205, 2007.

[32] E. G. Tveten, A. Brataas, and Y. Tserkovnyak, "Electron-magnon scattering in magnetic heterostructures far out of equilibrium," *Physical Review B*, vol. 92, no. 18, p. 180412, 2015.

[33] B. Koopmans, J. Ruigrok, F. Dalla Longa, and W. De Jonge, "Unifying ultrafast magnetization dynamics," *Physical review letters*, vol. 95, no. 26, p. 267207, 2005.

[34] F. Dalla-Longa, *Laser-induced magnetization dynamics: an ultrafast journey among spins and light pulses*. PhD thesis, Eindhoven University of Technology, 2008.

[35] N. Kazantseva, U. Nowak, R. W. Chantrell, J. Hohlfeld, and A. Rebei, "Slow recovery of the magnetisation after a sub-picosecond heat pulse," *EPL (Europhysics Letters)*, vol. 81, no. 2, p. 27004, 2007.

[36] A. Manchon, Q. Li, L. Xu, and S. Zhang, "Theory of laser-induced demagnetization at high temperatures," *Phys. Rev. B*, vol. 85, p. 064408, Feb 2012.

[37] M. Battiato, K. Carva, and P. M. Oppeneer, "Superdiffusive spin transport as a mechanism of ultrafast demagnetization," *Physical review letters*, vol. 105, no. 2, p. 027203, 2010.

[38] M. Battiato, K. Carva, and P. M. Oppeneer, "Theory of laser-induced ultrafast superdiffusive spin transport in layered heterostructures," *Physical Review B*, vol. 86, no. 2, p. 024404, 2012.

[39] A. Slachter, F. L. Bakker, J.-P. Adam, and B. J. van Wees, "Thermally driven spin injection from a ferromagnet into a non-magnetic metal," *Nature Physics*, vol. 6, no. 11, pp. 879–882, 2010.

[40] A. J. Schellekens and B. Koopmans, "Microscopic model for ultrafast magnetization dynamics of multisublattice magnets," *Physical Review B*, vol. 87, no. 2, p. 020407, 2013.

[41] N. Bergeard, V. López-Flores, V. Halte, M. Hehn, C. Stamm, N. Pontius, E. Beaurepaire, and C. Boeglin, "Ultrafast angular momentum transfer in multisublattice ferrimagnets," *Nature communications*, vol. 5, no. 1, pp. 1–7, 2014.

[42] M. Lalieu, *Femtomagnetism meets spintronics and magnonics*. PhD thesis, Department of Applied Physics, Mar. 2019. Proefschrift.

[43] C. Graves, A. Reid, T. Wang, B. Wu, S. De Jong, K. Vahaplar, I. Radu, D. Bernstein, M. Messerschmidt, L. Müller, *et al.*, "Nanoscale spin reversal by non-local angular momentum transfer following ultrafast laser excitation in ferrimagnetic gdfeco," *Nature materials*, vol. 12, no. 4, pp. 293–298, 2013.

[44] G.-M. Choi and B.-C. Min, "Laser-driven spin generation in the conduction bands of ferrimagnetic metals," *Physical Review B*, vol. 97, no. 1, p. 014410, 2018.

[45] S. Anisimov, B. Kapeliovich, T. Perelman, *et al.*, "Electron emission from metal surfaces exposed to ultrashort laser pulses," *Zh. Eksp. Teor. Fiz*, vol. 66, no. 2, pp. 375–377, 1974.

[46] M. Beens, M. L. Lalieu, A. J. Deenen, R. A. Duine, and B. Koopmans, "Comparing all-optical switching in synthetic-ferrimagnetic multilayers and alloys," *Physical Review B*, vol. 100, no. 22, p. 220409, 2019.

[47] V. Gridnev, "Ultrafast heating-induced magnetization switching in ferrimagnets," *Journal of Physics: Condensed Matter*, vol. 28, no. 47, p. 476007, 2016.

[48] M. Beens, R. A. Duine, and B. Koopmans, "$s-d$ model for local and nonlocal spin dynamics in laser-excited magnetic heterostructures," *Phys. Rev. B*, vol. 102, p. 054442, Aug 2020.

[49] K. H. Bennemann, *Non-linear optics in metals*. No. 98, Oxford University Press, 1998.

[50] A. J. Schellekens, *Manipulating spins: novel methods for controlling magnetization dynamics on the ultimate timescale*. PhD thesis, Eindhoven University of Technology, 2014.

[51] A. Khorsand, M. Savoini, A. Kirilyuk, A. Kimel, A. Tsukamoto, A. Itoh, and T. Rasing, "Element-specific probing of ultrafast spin dynamics in multisublattice magnets with visible light," *Physical review letters*, vol. 110, no. 10, p. 107205, 2013.

[52] A. Schellekens, N. De Vries, J. Lucassen, and B. Koopmans, "Exploring laser-induced interlayer spin transfer by an all-optical method," *Physical Review B*, vol. 90, no. 10, p. 104429, 2014.

[53] J. Hamrle, J. Ferré, M. Nỳvlt, and Š. Višňovskỳ, "In-depth resolution of the magneto-optical kerr effect in ferromagnetic multilayers," *Physical Review B*, vol. 66, no. 22, p. 224423, 2002.

[54] Z. Vardeny and J. Tauc, "Picosecond coherence coupling in the pump and probe technique," *Optics Communications*, vol. 39, no. 6, pp. 396–400, 1981.

[55] H. Eichler, D. Langhans, and F. Massmann, "Coherence peaks in picosecond sampling experiments," *Optics communications*, vol. 50, no. 2, pp. 117–122, 1984.

[56] B. Koopmans, M. Van Kampen, and W. De Jonge, "Experimental access to femtosecond spin dynamics," *Journal of Physics: Condensed Matter*, vol. 15, no. 5, p. S723, 2003.

[57] F. Dalla Longa, J. Kohlhepp, W. Jonge, de, and B. Koopmans, "Influence of photon angular momentum on ultrafast demagnetization in nickel," *Physical Review B*, vol. 75, no. 22, pp. 224431–1/4, 2007.

[58] C.-W. Luo, Y. Wang, F. Chen, H. Shih, and T. Kobayashi, "Eliminate coherence spike in reflection-type pump-probe measurements," *Optics express*, vol. 17, no. 14, pp. 11321–11327, 2009.

[59] N. Zheludev, S. Popov, A. Malinowski, Y. P. Svirko, W. Liang, and C. Lin, "Coherent and incoherent specular inverse faraday effect in yba2cu3o7−δ," *Solid state communications*, vol. 90, no. 5, pp. 287–289, 1994.

[60] P. J. Kelly and R. D. Arnell, "Magnetron sputtering: a review of recent developments and applications," *Vacuum*, vol. 56, no. 3, pp. 159–172, 2000.

[61] W. Martienssen and H. Warlimont, *Springer handbook of condensed matter and materials data*. Springer Science & Business Media, 2005.

[62] M. Beens, M. L. Lalieu, R. A. Duine, and B. Koopmans, "The role of intermixing in all-optical switching of synthetic-ferrimagnetic multilayers," *AIP Advances*, vol. 9, no. 12, p. 125133, 2019.

[63] C. C. Katsidis and D. I. Siapkas, "General transfer-matrix method for optical multilayer systems with coherent, partially coherent, and incoherent interference," *Applied optics*, vol. 41, no. 19, pp. 3978–3987, 2002.

[64] S. J. Byrnes, "Multilayer optical calculations," *arXiv*, Dec. 2020. https://arxiv.org/abs/1603.02720.

[65] M. Isasa, E. Villamor, L. E. Hueso, M. Gradhand, and F. Casanova, "Temperature dependence of spin diffusion length and spin hall angle in au and pt," *Physical Review B*, vol. 91, no. 2, p. 024402, 2015.

[66] L. Liu, R. A. Buhrman, and D. C. Ralph, "Review and analysis of measurements of the spin hall effect in platinum," *arXiv*, Mar. 2012. https://arxiv.org/abs/1111.3702.

[67] C. O. Avci, K. Garello, M. Gabureac, A. Ghosh, A. Fuhrer, S. F. Alvarado, and P. Gambardella, "Interplay of spin-orbit torque and thermoelectric effects in ferromagnet/normal-metal bilayers," *Phys. Rev. B*, vol. 90, p. 224427, Dec 2014.

[68] M. Lalieu, R. Lavrijsen, R. Duine, and B. Koopmans, "Investigating optically excited terahertz standing spin waves using noncollinear magnetic bilayers," *Physical Review B*, vol. 99, no. 18, p. 184439, 2019.

[69] M. Peeters, "Field dependence of time-resolve all-optical toggle switching in co/gd bilayers," *MMM conference*.

[70] K. McKenna and G. Morgan, "Quantum simulations of spin-relaxation and transport in copper," *The European Physical Journal B*, vol. 59, no. 4, pp. 451–456, 2007.

[71] I.-H. Shin, B.-C. Min, B.-K. Ju, and G.-M. Choi, "Ultrafast spin current generated by electron–magnon scattering in bulk of ferromagnets," *Japanese Journal of Applied Physics*, vol. 57, no. 9, p. 090307, 2018.

[72] *Refractive Index Database*, (accessed November, 2020), https://www.filmetrics.com/refractive-index-database.

[73] R. Meservey and P. Tedrow, "Surface relaxation times of conduction-electron spins in superconductors and normal metals," *Physical Review Letters*, vol. 41, no. 12, p. 805, 1978.

A   Substrate optimization

The substrate on which a sample is sputtered, is of influence on the amount of light that is absorbed in and/or reflected of the sample. Furthermore heat dissipation from the sample to the substrate depends on the substrate choice. Depending on the laser fluence and heat dissipation, problems can arise during TR-MOKE measurements. Here, the choice of substrate for the measurements is elaborated on. Four different substrates are considered, i.e. a B doped Si substrate, a oxidized Si substrate with a 100 nm thick SiO_2 outer layer, a degenerately doped Si:B substrate and a degenerately doped oxidized Si:B substrate with a 100 nm thick SiO_2 outer layer.

A.1   Light absorption in the sample

The absorption by the magnetic multilayer sample on the Si:B and Si/SiO_2(100) substrates is calculated with a transfer matrix method (TMM) [63, 64] using the (complex) refractive index values (both from measurement within the group and literature [72]). For the CoNi and SiB, the refractive index of the layer's main component is used, being Ni and Si, respectively.
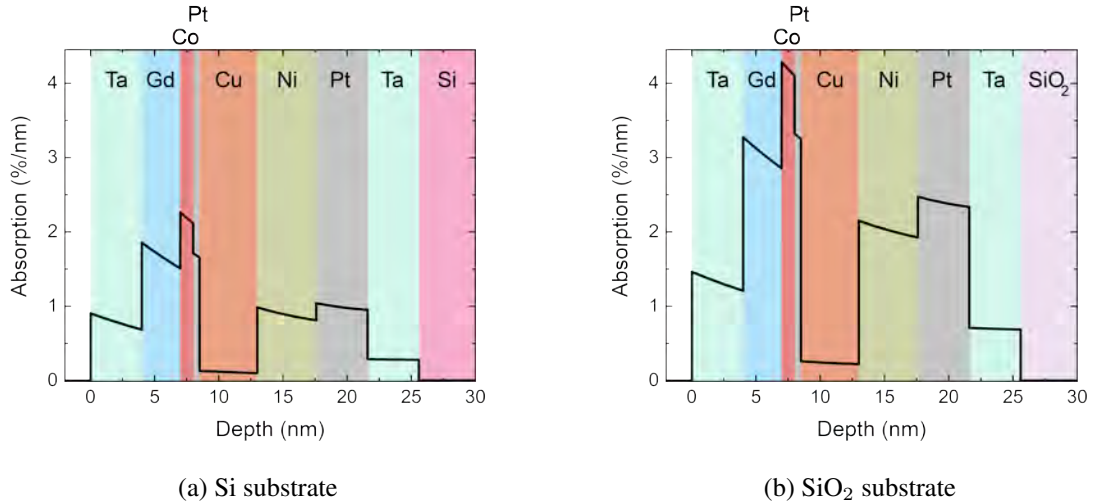

(a) Si substrate   (b) SiO_2 substrate

Figure A.1: TTM calculation of the absorption in the magnetic multilayer stack with $t_{Co} = 1$ nm and $t_{Ni} = 4.6$ nm on (a) a Si/SiO2(100) and (b) a Si substrate respectively.

The calculated absorption is plotted as a function of (penetration) depth in figure A.1. For a wavelength of 700 nm, the 100 nm of SiO_2 approximately doubles the absorption with respect to the Si:B substrate (figure A.1), which is attributed to the reflection of the laser light of the 100 nm thick SiO_2 layer. Even when assuming a 10 nm native oxide (SiO_2) layer on the Si:B substrates, the amount of absorption is found to be roughly half (0.53 times) the amount of absorption with 100 nm SiO_2. The amount of demagnetization at constant incident pump fluence is thus expected to be higher with a Si/SiO_2(100) substrate. Due to the mirror-like 100 nm thick SiO_2 layer, the signal-to-noise ratio for the MOKE measurements is also expected to be better. All measurements in sections 4.2, 4.3.1 and 4.3.2 are performed on Si/SiO_2(100) or deg doped Si:B/SiO_2(100) substrates.

A.2   The effects of heat diffusion

In order to measure the switching dynamics in the TR-MOKE setup, the sample needs to be pumped continuously (repetition rate 100 - 500 kHz). The relatively high fluence needed to switch the Co/Gd bilayer the low heat conductivity of the insulating SiO_2 results in to a lot of accumulated heat in the

(a) single pulses   (b) exposed & switched   (c) exposed & saturated   (d) damaged
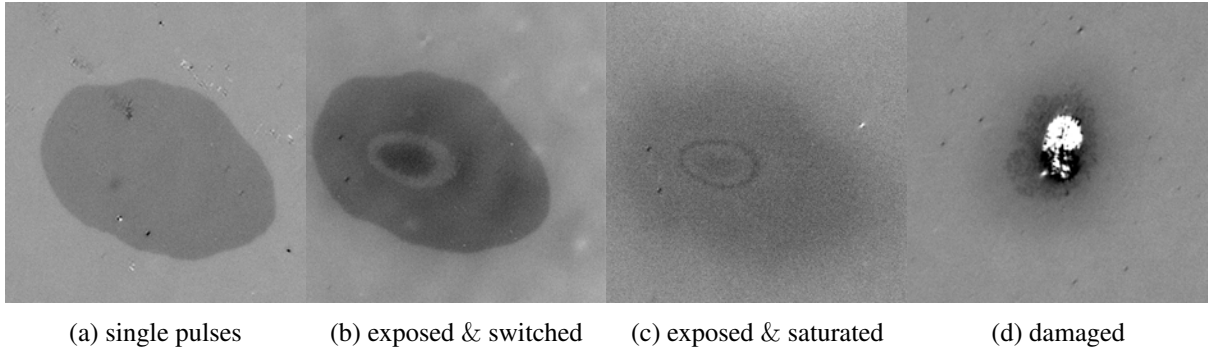
Figure A.2: (a) Kerr microscope image of a switched domain in a Co/Gd bilayer on an degenerately doped Si:B/SiO$_2$(100) substrate after exposure to eleven single pump pulses. (b) Switched domain after some time of exposure to the pump (100 kHz). The altered magnetic properties result in a multidomain state in the center of the pump. (c) The ring and multidomain state remain after the sample has been saturated. This shows that the pump induced change is permanent. (d) A different Co/Gd bilayer clearly shows damage after exposure to the pump.
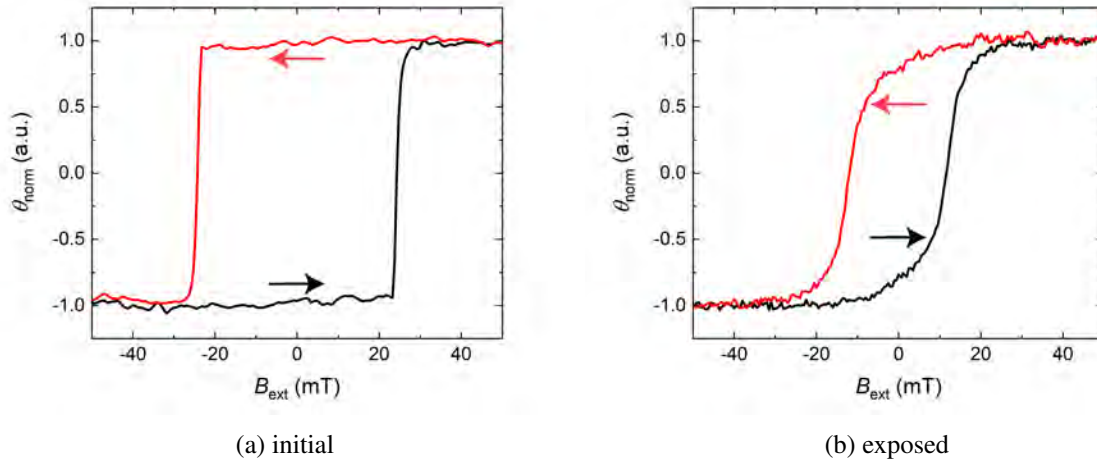

(a) initial   (b) exposed

Figure A.3: Hysteresis loop for a Co/Gd bilayer on degenerately doped Si:B/SiO$_2$(100) substrate as measured with MOKE (a) before and (b) after the sample has been exposed to the pump (100 kHz). The arrows indicate the direction of the field sweep. The pump induced heating (locally) changes the magnetic properties of the sample, resulting in a slanted loop.

sample. As a result, the magnetic properties of the sample are changed or the sample is damaged. The change in magnetic properties is attributed to thermally driven intermixing.

In the Si:B/SiO$_2$(100) substrates, an increased thermal conductivity is expected as a result of the dopant. Consequently, less thermally driven change to the sample is expected. However, after exposure to the pump, the same change in the magnetic properties and even damage is observed. In figure A.2a a Kerr microscope image of a switched domain on a degenerately doped Si:B/SiO$_2$(100)/Ta(4)/Pt(4)/Co(1)/Gd(3)/Ta(4) sample after eleven single pulses (time interval of a few seconds between each pulse) is shown. Figure A.2b shows a switched domain on the same sample, after the spot on the sample has been exposed to the pump (100 kHz). In the middle of the switched area, what looks like a multi-domain state surrounded by an unswitched ring is observed. The ring and multidomain state remain, after the sample has been saturated with an external field (figure A.2c). The magnetic properties of the sample have clearly been modified. This modification is also observed in the hysteresis loop. Before pump exposure, the sample is still saturated at zero field (figure A.3a). After the sample has been exposed to the pump, an unsaturated

(<1.0 or >-1.0) normalised Kerr signal is observed when no field is applied (figure A.3b).

Eventually, degenerately doped Si:B substrates are used for TR-MOKE measurements of the switching dynamics (section 4.3.3). The larger heat conductivity with respect to the Si:B/SiO$_2$(100) substrate results in a smaller amount of accumulated heat in the sample. Less change to the magnetic properties of the sample is observed.

B   Material parameters $s - d$ model

This appendix treats the values for material properties that are used throughout this thesis. The used parameters are listed in tables B.1 and B.2. Most values have been adopted from previous work [33, 46, 48]. Some of the material parameters are discussed below.

Table B.1: Global properties sections [33, 46].

T_{amb} (K)	g_{ep} (Jm^{-3}ps^{-1})	γ_{e} (Jm^{-3}K^{-2})	C_{p} (Jm^{-3}K^{-1})	τ_{D} (ps)	σ (fs)
295	$4.05 \cdot 10^6$	2000	$4 \cdot 10^6$	20	50

Table B.2: Material dependent properties [10, 33, 46, 48].

material	S	μ_{at} (μ_{B})	T_{C} (K)	ρ_{sd} (eV)	τ_{sd} (ps)	τ_{s} (ps)	τ_{eq} (fs)
Co	$\frac{1}{2}$	1.72	1388	1.0	0.3	0.2	0.01
Gd	$\frac{7}{2}$	7.55	292	1.0	10.0	0.02	0.01

Following the example by reference [46], the intersublattice Weiss molecular field constants set to $\gamma_{\mathrm{Co,Gd}} = -0.388\gamma_{\mathrm{Co,Co}}$ and $\gamma_{\mathrm{Gd,Co}} = \gamma_{\mathrm{Co,Gd}} \frac{\mu_{\mathrm{at,Co}}}{\mu_{\mathrm{at,Gd}}}$.

As mentioned in section 2.3.1, the timescale τ_{sd} is closely related to the demagnetization rate. Consequently, the value is set based on demagnetization rate R in the M3TM [30, 46], τ_{sd} for Co is set to 0.3 ps, whereas the Gd value is set to 10 ps.

The Co value for spin-orbit relaxation time τ_s is set to the literary value of 0.2 ps [71]. The spin-orbit relaxation time τ_s is expected to decrease significantly with the atomic number of a material [73]. As the atomic number of Gd is much larger than the atomic number of Co, the Gd τ_s is set to 20 fs, i.e. an order of magnitude smaller than the Co τ_s.

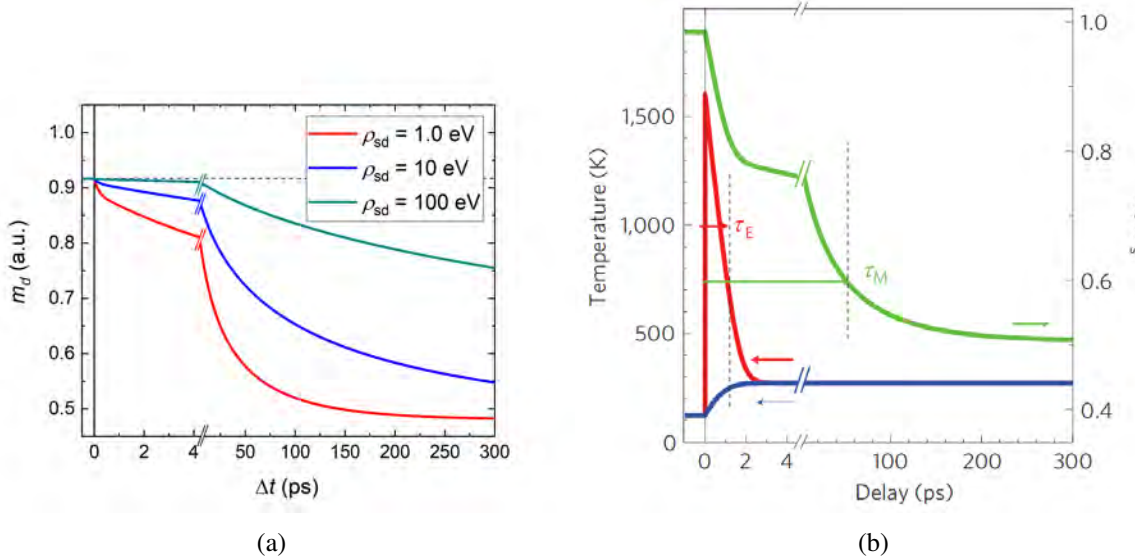(a)   (b)

Figure B.1: (a) m_d dynamics for Gd after laser pulse excitation as described in the (macro spin) $s - d$ model, with an ambient temperature of 120 K, $P_0 = 6 \cdot 10^8 \frac{\mathrm{J}}{m^3}$ and $\tau_{\mathrm{D}} = \infty$. (b) Simulated laser-induced demagnetization of Gd. From [30].

The ρ_{sd} depends (mostly) on the density of states around the fermi level [48]. For Co the value of 1.0 eV used by reference [48] is adopted. In figure B.1 the modelled dynamics for a Gd macro spin for three different values of ρ_{sd} are shown. Since the Curie temperature for Gd is below room temperature,

the plotted curves are for an ambient temperature of 120 K. For ρ_{sd} in the order of 1 eV (figure B.1a), the expected two step Gd demagnetization behavior is found (figure B.1b) [30]. Therefore, for Gd ρ_{sd} is set to 1.0 eV as well, which agrees well with the assumption that the DOS of the s system is homogeneous throughout the structure (which is used to describe the equilibration of the different monolayer's s systems, section 2.3.2).

C   Measuring only even or odd pulses

In section 4.3.3 the spin current assisted switching dynamics are measured by isolating the signal from the even or odd laser pulses. In this appendix, the manner in which the signal is isolated is explained.
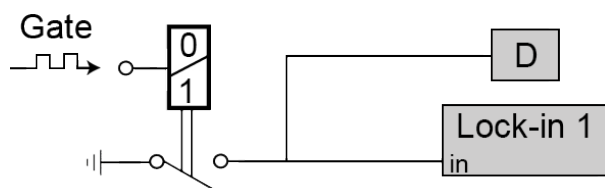

Figure C.1: Schematic representation of the device used to isolate the signal for only the even or odd laser pulses.

A binary counter is connected to the output gate of the Spirit-NOPA laser (figure C.1). The gate output consists of a block wave with a frequency equal to the 500 kHz repetition rate of the Spirit-NOPA. Consequently, the binary counter toggles between a '1' and '0' state every time the laser emits a pulse. The binary counter in its turn toggles a switch. When the counter is set to (for example) 0, the switch is open and the output signal of the photodetector is transmitted to lock-in 1. When the counter reads 1, the switch is closed and the output of the photodetector is grounded. Consequently, no signal is measured in lock-in 1. In this way, every other probe pulse is measured.

A manual switch is located on the side of the device. With this switch, the operation of the device can be reversed, i.e. now the photodetector's signal is transmitted when the counter reads 1, instead of 0. In this manner, instead of measuring (for example) only the even pulses, the odd pulses are measured. The manual switch is used to verify that the device operates properly. During the work presented in this thesis, the manual switch is kept in a single direction. The reason for this is that a slight change in the transmitted signal's amplitude and phase is observed when the manual switch is flipped. In order to be able to qualitatively compare the measurements, the manual switch is not used during measurements. Instead, the initial state of the sample is changed with an applied field.

The frequency of the gate output is always 500 kHz, regardless of the value at which the pulse picker is set. In order for correctly isolate the pulse signal for an even or odd number of pump pulses, the pulse picker should therefore always be set to an odd value (e.g. 1 or 5, for measurement at a pulse rate of 500 or 100 kHz, respectively). Furthermore, it is important that the number of pump pulse that have excited the sample and the binary counter state remain correlated. Therefore, the chopper and the binary counter can not be used simultaneously.